Phil. Trans. R. Soc. Lond. A **322**, 213–241 (1987) [213]
Printed in Great Britain

STRATIFIED ROTATING FLOW OVER AND AROUND ISOLATED THREE-DIMENSIONAL TOPOGRAPHY

BY D. L. BOYER[1], P. A. DAVIES[2], W. R. HOLLAND[3], F. BIOLLEY[1] AND H. HONJI[4]

[1] *Department of Mechanical Engineering, University of Wyoming, Laramie, Wyoming* 82071, *U.S.A.*
[2] *Department of Civil Engineering, The University of Dundee, Dundee DD*1 4*HN, U.K.*
[3] *National Center for Atmospheric Research, P.O. Box* 3000, *Boulder, Colorado* 80307, *U.S.A.*
[4] *Research Institute for Applied Mechanics, Kyushu University, Fukuoka* 812, *Japan*

(*Communicated by P. H. Roberts, F.R.S. – Received* 17 *January* 1986)

[Plates 1–16]

CONTENTS

Laboratory and numerical experiments have been conducted on the flow of a linearly stratified rotating fluid past isolated obstacles of revolution (conical and cosine-squared profiles). Laboratory experiments are considered for a range of Rossby, Ekman and Burger numbers, the pertinent dynamical parameters of the system. In these experiments, inertial, Coriolis, pressure, viscous and buoyancy forces all play a significant role. Emphasis is given to examining the nature of the time development of the flow fields as well as its long-time behaviour, including eddy shedding. It is shown, for example, that increased stratification tends to diminish the steering effect

of the obstacle, other parameters being fixed, at elevation levels above the topography. At levels below the top of the obstacle, increased stratification tends to force the fluid around rather than over the body and this, in turn, tends to develop vortex shedding at smaller Reynolds numbers than would occur in corresponding lower stratification cases. Data for the cone reveal that the Strouhal number for the eddy-shedding régime is relatively insensitive to the values of Ro, Ek and S for the range of parameters investigated.

Stratification tends to induce lee waves in the topography wake, and the nature of this lee-wave pattern is modified by the presence of rotation. For example, it is demonstrated that for vertically upward rotation, the lee waves on the right, facing downstream, have a larger amplitude than their counterparts at the same location on the left.

The steering effects, as predicted by a three-level quasigeostrophic numerical model, are shown to be in good agreement with the laboratory results for a narrow range of parameter space. The numerical model is used to examine the effects of rotation, friction and stratification in modifying the flow. The quasigeostrophic numerical simulations do not produce eddy shedding, and it is concluded that a full, primitive equation numerical model would be needed to explore this phenomenon.

1. Introduction

For many years, there has been a recognition that the large-scale effects of extensive mountain complexes upon incident wind fields can be simulated in several important respects by theoretical and physical models in which slow steady uniform flows of stratified and rotating fluids are deformed by the presence of isolated solid obstacles placed in the flow (see, for example, Buzzi & Tibaldi 1977; Baines & Davies 1980; Smith 1980; Davies & Boyer 1984). Particular emphasis in this regard has been placed recently upon the sub-grid scale fluid dynamical processes occurring in the neighbourhood of the Alps (GARP 1978), and the associated Alpex programme of field observations and theoretical investigations (GARP-Alpex 1982*a*, *b*) has generated renewed interest in these problems.

In this paper we report some recent laboratory results that are of relevance to the above processes. Attention has been focused upon flows incident upon relatively smooth-sloped topographies (conical and cosine-squared obstacles of revolution) for which background rotation plays a significant but not dominant dynamical role. In terms of the non-dimensional parameters of the problem, attention has been confined primarily to flows having Burger numbers, $S \approx 1$, and Rossby numbers, $Ro \approx 10^{-1}$, where S and Ro can be regarded as denoting the relative importance of the buoyancy and inertial forces, respectively, to the Coriolis forces. No β-effect has been included in the studies, and topographic elements having maximum heights greater than the Ekman layer thickness have been employed.

Until recently, laboratory studies of topographic effects in rotating stratified fluids have concentrated upon flows in which rotation has been the dominant constraint (Davies 1972; Baines & Davies 1980) and for which the steering effect of the obstacle in the direction of the rotation vector has been of primary interest. In the present studies, and in the recent investigations by two of us (Boyer & Biolley 1986), density stratification exerts a much stronger influence than in other related experiments. In addition, attention is not restricted to steady flows, and both the downstream and interior† regions of the flow are investigated in some detail.

† The fluid contained within an imaginary upright cylinder circumscribing the obstacle is denoted the 'interior region'.

The present study can therefore be regarded as being complementary to, and an extension of, earlier experimental and numerical work on (i) f-plane and β-plane flows over and around solid cylindrical obstacles in rotating homogeneous fluids (Boyer & Davies 1982; Boyer *et al.* 1984), (ii) related studies with stratified, non-rotating (Brighton 1978; Snyder *et al.* 1979; Hunt & Snyder 1980; Castro *et al.* 1983; Snyder *et al.* 1985) and homogeneous non-rotating (Gaster 1969) flows past isolated topography, and (iii) f-plane, stratified flow over two-dimensional ridges (Boyer & Biolley 1986).

The plan for the paper is as follows. In §2, the fundamental dimensionless parameters governing the physical system are defined. In §3, the apparatus and experimental techniques employed, and the nature of the secondary motions observed in the tow-tank facility, are discussed. The results of the laboratory experiments are presented in §4. Numerical models, including comparisons with laboratory experiments, are given in §5, and some concluding remarks are made in §6.

2. Non-dimensional parameters

The flow configuration relative to the right-handed cartesian coordinate system (x, y, z) is illustrated schematically in figure 1. A linearly stratified fluid of mean density, ρ_0, and kinematic viscosity, ν, and having a normalized vertical density difference, $\Delta\rho/\rho_0$, is contained within a long horizontal channel of rectangular cross section of width, L, and depth H, that rotates uniformly about a vertical axis (z) with angular velocity $\omega(0, 0, \omega)$. Relative to a rotating observer, the fluid is in uniform motion, with steady velocity $(U, 0, 0)$ past a body of revolution symmetric about the z-axis and of maximum height, h_0, and base diameter, D. In the experiments, as discussed below, the relative flow is generated by towing the topographic feature through the fluid, which is otherwise at rest relative to a rotating observer. It is a straightforward matter to show that these systems are dynamically equivalent.

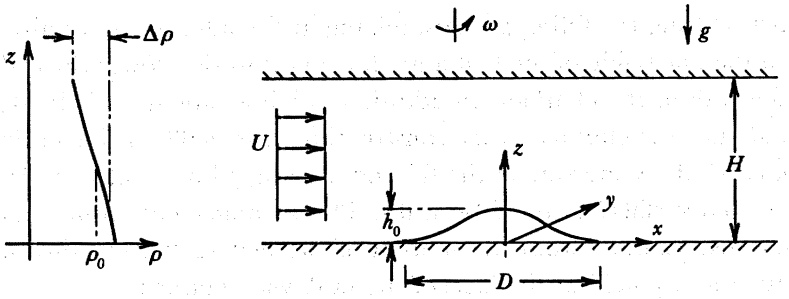

FIGURE 1. Physical system.

A suitable set of independent, non-dimensional parameters defining the flow is thus:

(i) $Ro = U/2\omega D$, the Rossby number;

(ii) $Ek = \nu/2\omega H^2$, the Ekman number;

(iii) $S = g(\Delta\rho)\,H/4\omega^2\rho_0 D^2 = N^2H^2/4\omega^2D^2$, the Burger number;

(iv) h_0/D, h_0/H, D/L, the geometrical parameters; and

(v) the obstacle shape.

Here, N is the Brunt–Väisälä frequency defined by $N = (g\Delta\rho/\rho_0 H)^{\frac{1}{2}}$, and g is the acceleration due to gravity. Note that other familiar non-dimensional parameters such as the Reynolds

number, $Re = UD/\nu = (Ro/E)\,(D^2/H^2)$, and the Froude number, $Fr = U/Nh_0 = (Ro/S^{\frac{1}{2}})\,(H/h_0)$, are not independent of the above. For cases in which the flow is stratified, but not rotating, the Reynolds and Froude numbers are generally used as the determining parameters (Brighton 1978; Hunt & Snyder 1980), whereas when the fluid is homogeneous and non-rotating, the Reynolds number is the sole dynamical parameter (Tritton 1977) determining the character of the flow.

3. Experimental apparatus and techniques

The apparatus used in this study has already been described in detail in previous communications (Kmetz 1982; Boyer & Kmetz 1983; Boyer & Biolley 1986). The experimental facility consists of a Perspex channel–tow tank having dimensions 2.4 m × 0.4 m × 0.3 m mounted horizontally on a rotating turntable, the angular velocity of which can be varied smoothly and continuously. The channel can be filled with a salt-stratified fluid by the familiar Oster double-reservoir technique (Oster 1965; Davies 1972) to produce a stable density profile within the working section. The depth of fluid within this section of the channel is controlled by the vertical adjustment of a horizontal Perspex lid, and an isolated three-dimensional solid obstacle (either a tall cone or a shallow cosine-squared topography), is translated through the fluid by means of a continuous belt to which the base of the obstacle is mounted. A variable speed motor controls the speed of (i) the belt and (ii) an overhead platform that is linked synchronously to the motor drive by a chain and sprocket arrangement. Video and still cameras can be mounted on the platform to record the flow structure in the tank with respect to a frame of reference fixed to the moving obstacle. Lighting for flow visualization at different levels and cross sections is provided from a battery of projectors into which slides with long narrow slits have been inserted; the lighting system is also affixed to the rotating platform.

In the present study, attention was confined to linear density gradients, this state being achieved by careful regulation of the flow rates between the brine and fresh-water reservoirs and the channel. During the filling process, mixing at the inlet was minimized by routing the fluid directly to the underside of the belt and allowing it to rise slowly through a gap between the belt and the wall of the channel. In addition, mixing caused by belt-edge effects during an experimental run was eliminated by constructing false walls to the working section. The walls were bolted to the underside of the lid and a foam-rubber seal was placed between the belt and the bottom surfaces of the false walls. This arrangement ensured that there was no transfer of edge disturbances from the motion of the belt to the working section, and that continuity in the density field at the base of the tank was retained.

The density gradient was established with the channel at rest. The angular velocity of the turntable was then increased in small incremental steps until the required rotation rate was reached. After the fluid had reached solid-body rotation (see, for example, Boyer & Biolley 1986), the stratification was checked by withdrawing small samples in turn from eight reference levels in the working section and measuring the density of the samples with a refractometer. The density gradient was monitored frequently throughout the experimental runs.

The electrolytic precipitation method (Honji *et al.* 1980; Boyer *et al.* 1984) and the suspended particle technique (Boyer & Biolley 1986) were used for visualization of both steady and unsteady flows. Flow streaklines relative to the obstacle were obtained with the former method, and in the latter case streamlines relative to the object and the tank were obtained by recording

(2–5 s) time exposures of the moving particles with the camera mounted on the moving platform and translating with the topography. The exposure time, Δt, could be adjusted so that for different belt velocities, U, the dimensionless exposure time, $\tau_e = (\Delta t)\, U/D$, could be kept constant. The small (0.5 mm diameter) polystyrene spheres used as marker particles had a mean density of 1.04 ± 0.01 g cm^{-3}, and the mean density of the stratified fluid was matched to this value to ensure that small variations in density of the polystyrene could be used to produce an approximately uniform vertical distribution of tracer particles. The particles were illuminated at different levels in the tank with light beams having a width of approximately 5 mm.

Case-study investigations of the flow over and around the obstacles were conducted by using stratification levels, $\Delta\rho/\rho_0 \approx 5.0\%$ and 0.5%, respectively, over a range of Rossby, Ekman and Burger number combinations. For a particular geometry, the same obstacle and fluid depth were used throughout, and variations in the above parameters were produced by changing U and ω only (for a given $\Delta\rho/\rho_0$).

3.1. *Secondary flows*

For cases in which the fluid is unstratified, it is known that secondary flows and instabilities can develop in rotating channel flows (Hart 1971; Lezius & Johnston 1976; Speziale & Thangam 1983), and that such flows can modify significantly the longitudinal velocity profile, particularly when the basic flow is turbulent. However, when the fluid is stably stratified and rotating, and the flow is laminar and forced by the motion of the bottom boundary (as in the present study), secondary flows of a different type are established because the bottom boundary layer transports 'heavy' fluid in both the downstream and rightward directions. By continuity, secondary return flows must develop in the interior region to replace the heavy-fluid deficit and thereby balance the primary mass flux forced by the motion of the bottom boundary. For rotating homogeneous flow, the return flow due to the streamwise Ekman-layer transport is rather uniformly distributed over the entire cross section and thus is relatively weak compared with the belt speed (i.e. $O(E^{\frac{1}{2}})$); see, for example, Boyer & Kmetz (1983).

To study the nature of this secondary return flow (i.e. its magnitude and spatial structure), a series of exploratory experiments was conducted without an obstacle in the flow. Axial velocities were measured for a cross section in the vicinity of the streamwise channel centre by taking time exposures of the motion of tracer particles with a camera fixed with respect to the moving belt. From these photographs the velocity, U, of the belt was subtracted to obtain u', the velocity with respect to the tank.

Figure 2 depicts the spatial distribution of u'/U for both a non-rotating (a) and a rotating (b) experiment. It is noted that for the stratified, non-rotating case, there is a return flow present over the entire cross section but this flow is stronger in the lower levels. Note also that the secondary return flow without rotation is quite uniform across the channel. Figure 2b depicts the return flow for a typical stratified, rotating case. One notes that again the stronger return flows are in the lower portions of the channel, but, under the influence of rotation, there is now a significant cross-channel variation in flow velocity. In particular, the rotating experiments are characterized by sidewall jets, the strength of which (i) decrease with increased $Ro_L = U/2\omega L$, (ii) increase with increased $S_L = g(\Delta\rho)\, H/4\omega^2\rho_0 L^2$, and (iii) increase with increased Ek if, in each case, the other parameters remain fixed. Here, Ro_L and S_L are the channel Rossby and Burger numbers, respectively, each being defined by using the channel width as the characteristic horizontal dimension. In the interior of the channel and in the

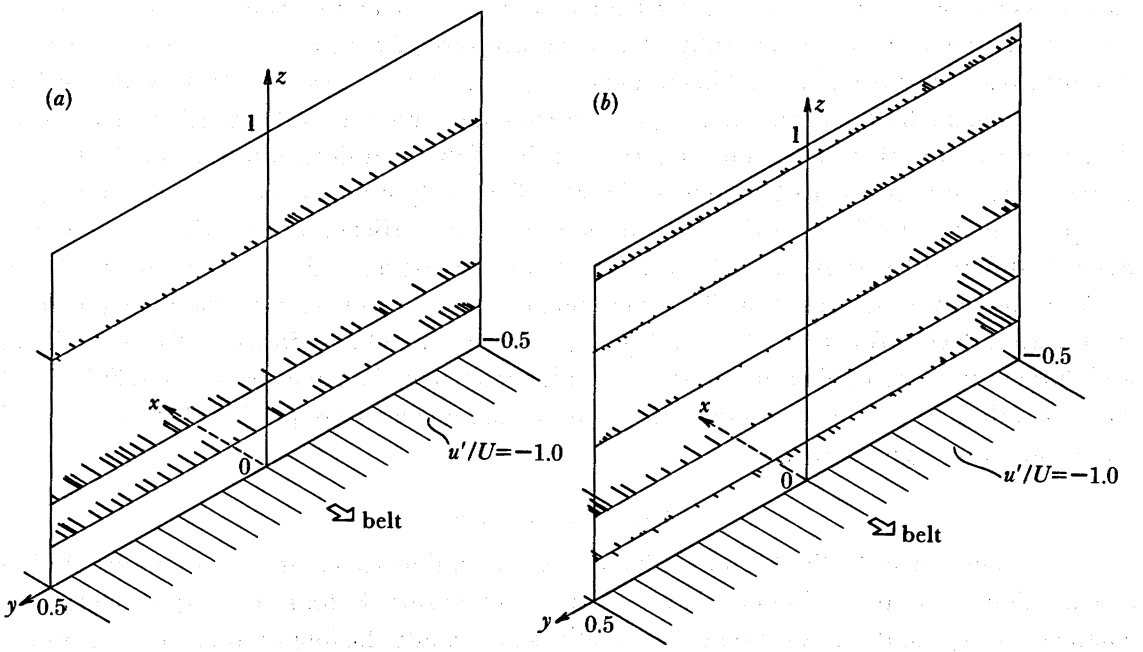

FIGURE 2. Streamwise secondary motions, u'/U, for $H/L = 0.26$ and parameter values shown (see text for definitions) (*a*) stratified, non-rotating, $\Delta\rho/\rho_0 = 7.9 \times 10^{-3}$, $Re_L = 760$, $Ro_L = Ek = \infty$; (*b*) stratified, rotating, $\Delta\rho/\rho_0 = 7.5 \times 10^{-3}$, $Re_L = 720$, $Ro_L = 0.06$, $Ek = 3.0 \times 10^{-4}$.

side-wall jets, the secondary flow decreases with vertical distance from the belt; in the lower levels, the flow is in the same direction as that of the belt, but above $z/H \approx 0.25$, the flow reverses. In all cases, the smallest secondary flows occur near the centre of the channel.

Measurements of the velocities and lateral-length scales of the side-wall jets, as exemplified by that in figure 2*b*, indicate that these motions are in quasigeostrophic balance (i.e. typical Rossby numbers of order 10^{-1}). This being the case, the isobars in the vicinity of the jets must be tilted in such a way as to have high pressure on the right facing in the direction of the jet motion; see the schematic diagram in figure 3. One possibility for tilting the isobars in such a way as to support the observed secondary motion might be the transport of relatively heavy fluid by the Ekman boundary layers on the belt into the corner region in the vicinity of $y = 0.5$, $z = 0.0$ and away from the corner region near $y = -0.5$, $z = 0.0$ (see figure 3) where y, z have been made dimensionless with L, H, respectively. In the corner along $y = 0.5$, $z = 0.0$, the fluid is forced to rise vertically along the solid vertical boundary, but the vertical excursion is limited by the fluid's excess negative buoyancy. A local circulation is thereby established as shown. Along the corner region $y = -0.5$, $z = 0.0$, a circulation of the same sense is induced because of the excess positive buoyancy of the fluid particles that are forced to descend to maintain the Ekman transport out of this corner. As one notes, however, these corner circulations would tend to drive the isopycnals (hence isobars) in the opposite direction to those that must occur to drive the jets in the directions indicated.

It is thus concluded that the principal mechanism at work in driving the jets is the complex response to the streamwise transport of heavy fluid by the belt. This transport sets up a pressure gradient in the $+x$ direction, resulting in a weak cross-channel transport of fluid as indicated in figure 3. In addition, the return flow balancing this transport occurs near the channel walls and forces the isobaric surfaces to have the general shape indicated.

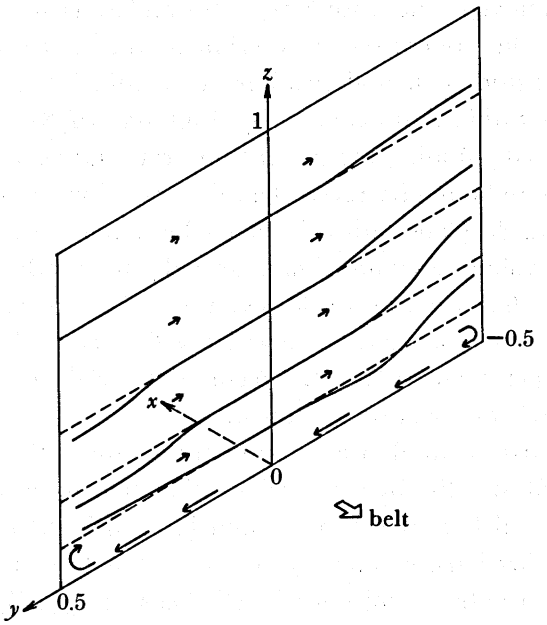

FIGURE 3. Schematic representation of isobars and secondary flows in the channel cross-section for rotating and stratified flow compatible with the observed streamwise motions.

4. LABORATORY EXPERIMENTAL RESULTS

In this section, the principal qualitative features of the various flow configurations are delineated. These are then placed in the context of flow-régime diagrams of inverse Froude number against Reynolds number (for various Ekman numbers), to allow an understanding of where the various flow characteristics can be found in parameter space. Photographs from particular experiments are presented to clarify the discussion and to allow future investigators the opportunity of comparing potential analytical and numerical models with the experimental observations.

4.1. *Non-rotating, linearly stratified flows*

The initial experiments are concerned with non-rotating flows. This allows comparison with their rotating counterparts discussed below. By varying the vertical proportional density difference, $\Delta\rho/\rho_0$, from 0 to *ca.* 5% and the speed of the obstacle in the range $0.5 \leqslant U \leqslant 1.5$ cm s^{-1}, the Froude and Reynolds number ranges investigated were: cone ($0.03 < Fr < 0.82$ and $Fr = \infty$, $370 < Re < 1130$) and cosine-squared ($0.10 < Fr < 1.20$ and $Fr = \infty$, $500 < Re < 1520$), respectively. For all experiments the obstacles were placed in the centre of the channel to minimize the effects of secondary flows.

4.1.1. *Conical obstacle*

The conical obstacle had a base diameter, $D = 7.6$ cm, and a height, $h_0 = 6.6$ cm, with the fluid depth, $H = 8.1$ cm; the cone was thus relatively tall ($h_0/H = 0.81$) and steep ($h_0/D = 0.87$), and in these respects it differed somewhat from the obstacles of similar geometry used in earlier studies by other investigators. For example, Gaster (1969) investigated homogeneous flows past slender cones having maximum values of $h_0/H = 0.7$ and $h_0/D = 36.0$,

and Brighton (1978) employed cones with $h_0/H = 0.4$ and $h_0/D = 0.7$. The range of Reynolds numbers investigated in the present set of experiments (i.e. $370 < Re < 1130$) was approximately the same as those studies cited above. For the stratified flow case, the range of Froude numbers considered was within that explored by Brighton (1978).

As in the Brighton (1978) studies, the present non-rotating experiments are characterized by the presence of a bottom boundary layer, the thickness of which is not negligible compared with the height of the obstacle. Considering the belt to be an infinite plane surface, the boundary layer grows as $\delta \approx (\nu t)^{\frac{1}{2}}$, where we assume similar growth rates for the stratified and unstratified cases. The thickest layers thus occur for the lowest speeds (i.e. 0.5 cm s^{-1}). With the maximum belt traverse being approximately 120 cm, and with $\nu \approx 0.01$ cm^2 s^{-1}, the maximum boundary-layer thickness in the experiments is $\delta_{max} \approx 1.5$ cm. Some of the observations to be discussed were made below this level and will be so indicated.

It is useful to first discuss the qualitative nature of the observed flow for cases in which the free-stream speed is fixed and the background stratification is varied. Figure 4*a–c*, plate 1, depicts experiments for which $U = 1.0$ cm s^{-1} and for which $\Delta\rho/\rho_0 = (0.00, 0.007, 0.064)$, respectively. The normalized tracer injection level is $z^*/h_0 = 0.76$ (in this and subsequent figures, z^* will represent the tracer injection level). Because $\delta_{max}/h_0 \approx 0.17$, the observation level is well above the boundary layers.

The Reynolds number is thus approximately fixed at $Re = 720$, while the Froude numbers, are $(\infty, 0.17, 0.05)$ respectively. The series of photographs under figure 4i show some of the detailed structure of the wake in the vicinity of the cone; we term these 'near-field observations'. The photographs under figure 4ii depict the flow field at large distances from the obstacle; we term these 'far-field observations'.

For an upright obstacle having non-vertical sides, it is to be expected that the downstream flow is three-dimensional, at least in the immediate vicinity of the obstacle and especially for cases in which the fluid is homogeneous or weakly stratified. This is confirmed by the relatively indistinct and confused dye traces in figure 4*a, b*; i.e. vertical motions in the wake cause dye to be elevated and depressed with respect to the illumination level. The relatively clear dye traces in figure 4*c* are indicative of weak vertical motions; i.e. the flow occurs in approximately horizontal planes.

In addition to the suppression of vertical motion by a decrease in *Fr*, the most evident manifestation of smaller Froude numbers is the modification to the far wake form. For the homogeneous case (figure 4*a*ii), the wake develops from eddy pairs that are formed and shed approximately symmetrically from the rear of the obstacle; see also figure 5, plate 2. The far-field wake for this case is not characterized by a vortex street (which is typical for flow past an upright cylinder of uniform cross section in this Reynolds number range) but rather by an array of symmetrical eddy pairs confined within a rather narrow envelope, the form of which we denote as 'varicose'; see figures 4*a*i, *a*ii. The differences between the wake forms of the cone and cylinder in the homogeneous case are ascribed to the large vertical motions induced by the sloping walls of the conical topography. This, in turn, results in coherent slanted vortices being generated at the wall and advected downstream. As will be seen below, both stratification and rotation inhibit this vertical motion and promote motion in approximately horizontal planes. In such cases, the wake produced has the structure of a classical vortex street. This is seen in the comparisons between the homogeneous case (figure 4*a*) and the stratified cases (figure 4*b, c*), the latter exhibiting sinuous wakes near the obstacle and alternating eddy patterns characteristic of vortex streets far downstream.

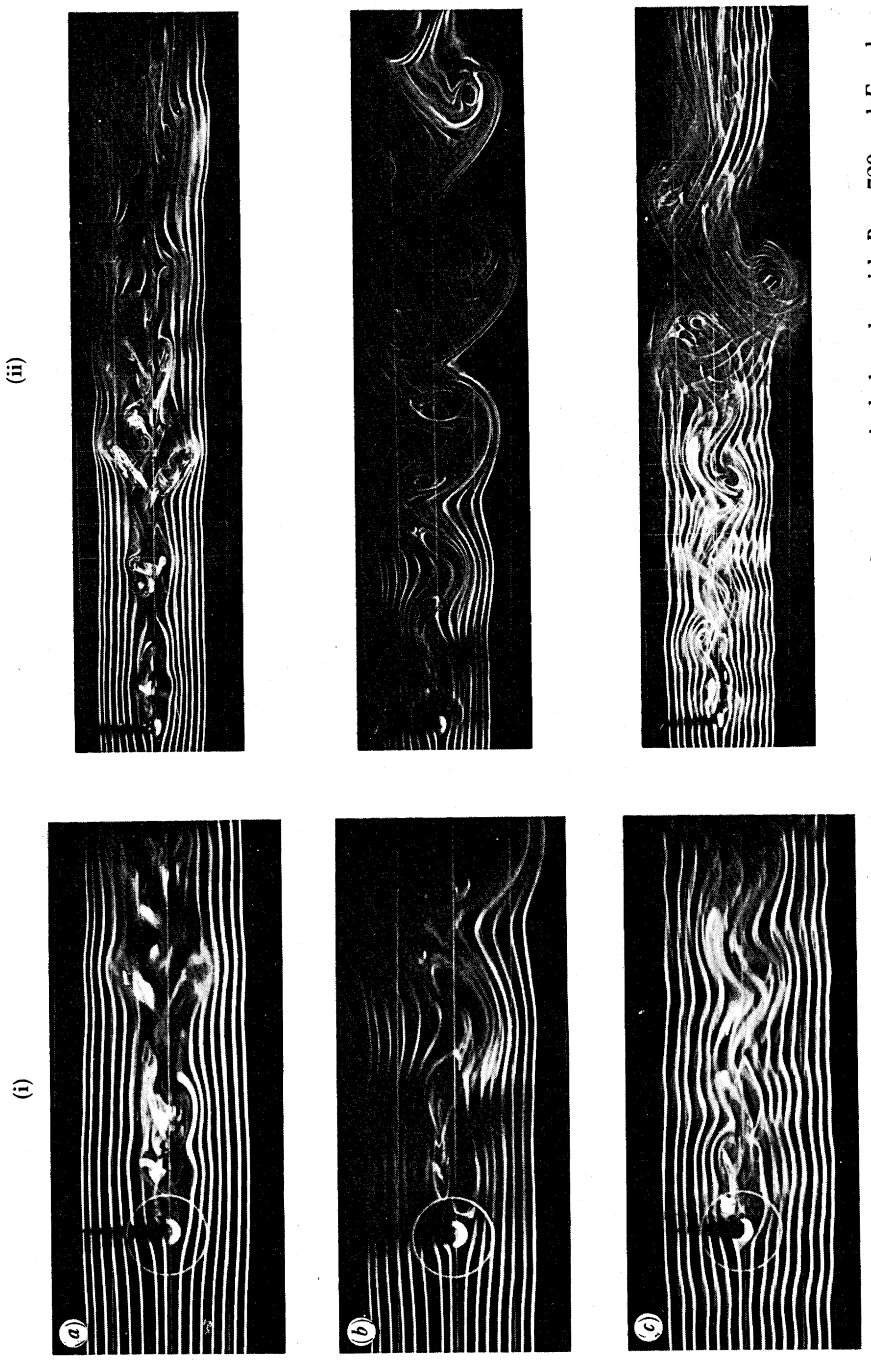

FIGURE 4. (i) Near-field and (ii) far-field streakline patterns for non-rotating flow past conical obstacles with $Re = 720$ and Fr values of (*a*) ∞, (*b*) 0.17 and (*c*) 0.06; $h_0/H = 0.81$, $h_0/D = 0.87$, $D/L = 0.24$ and $z^*/h_0 = 0.76$.

(*Facing p.* 220)

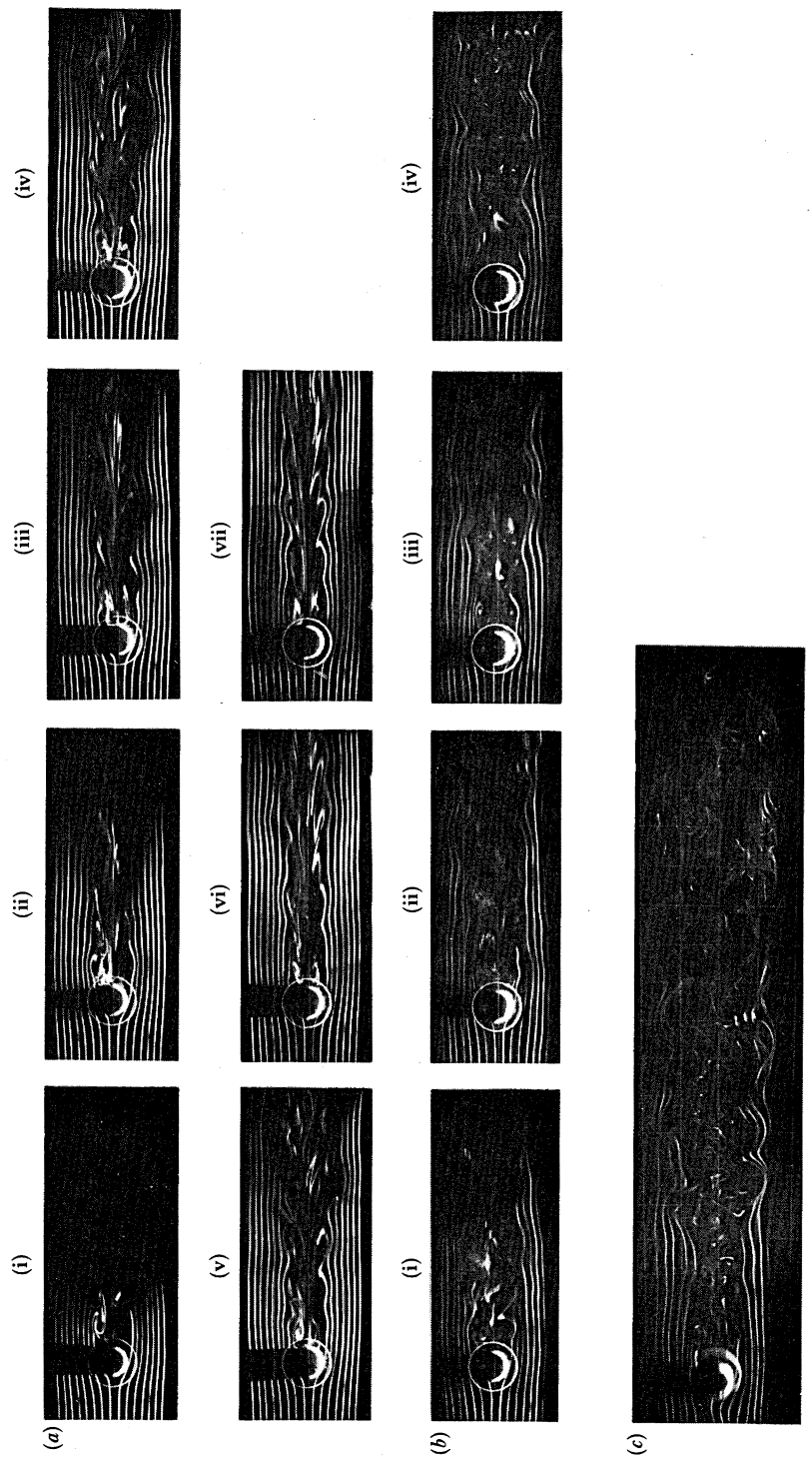

FIGURE 5. (*a*), (*b*) Near-field and (*c*) far-field streakline patterns for homogeneous non-rotating flow past conical obstacles with *Re* values of (*a*) 740 and (*b*), (*c*) 1110; geometrical parameters as in legend of figure 4 and $z^*/h_0 = 0.46$. Note that (*a*) and (*b*) represent time sequences.

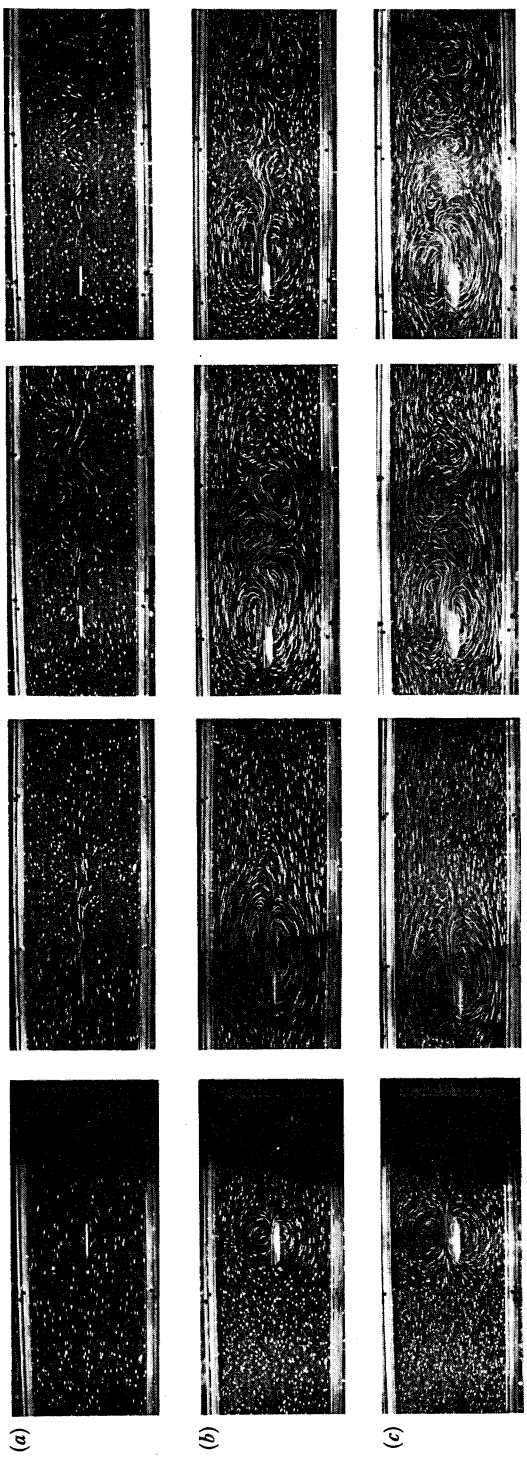

FIGURE 6. Time sequences of particle-streak photographs for non-rotating flow past conical obstacle with $Re = 390$, $Fr = 0.08$ and z^*/h_0 values of (*a*) 0.88, (*b*) 0.46 and (*c*) 0.15; geometrical parameters as in legend of figure 4. The dimensionless exposure time, $\tau_e = (\Delta t)U/D$ is 0.99, while the elapsed dimensionless time, $\tau = tU/D$, is noted on the figure (see text).

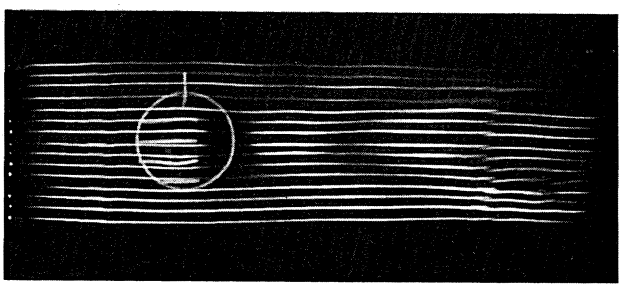

FIGURE 8. Streakline photograph depicting the existence of lee waves for non-rotating flow past a cosine-squared obstacle for $Re = 1500$, $Fr = 0.69$, $h_0/H = 0.25$, $h_0/D = 0.20$, $D/L = 0.32$ and $z^*/h_0 = 1.46$. Note that the white lines painted on the upstream portion of the obstacle are not streaklines.

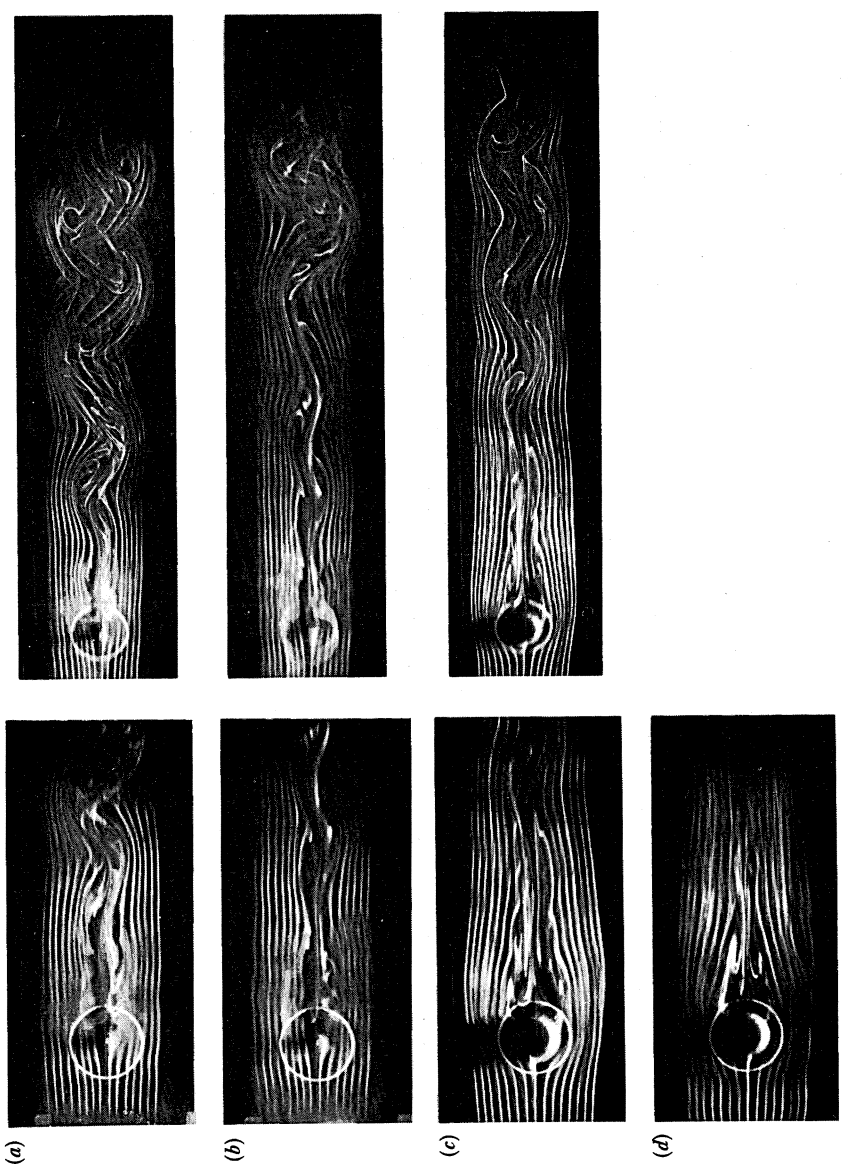

FIGURE 9. (i) Near-field and (ii) far-field streakline patterns for non-rotating flow past cosine-squared obstacle with z^*/h_0 values of (*a*), (*b*) 0.97 and (*c*), (*d*) 0.49, for *Re*, *Fr* values of (*a*) 1000, 0.19, (*b*) 1470, 0.29, (*c*) 1000, 0.18 and (*d*) 1470, 0.27. Geometrical parameters as in the legend of figure 8.

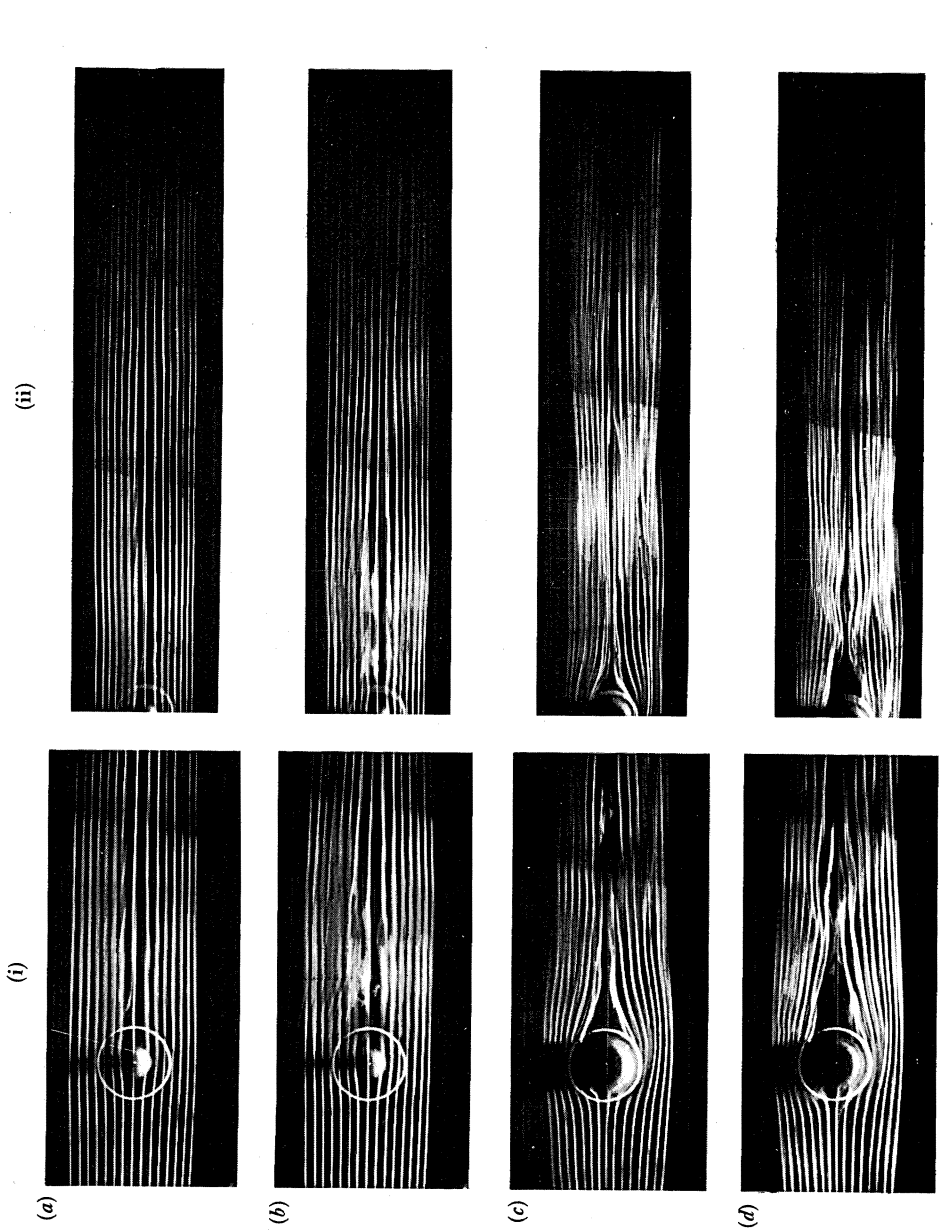

FIGURE 10. Legend as for figure 9 except for *Re*, *Fr* values of (*a*) 960, 0.55, (*b*) 1420, 0.75, (*c*) 960, 0.55 and (*d*) 1440, 0.76.

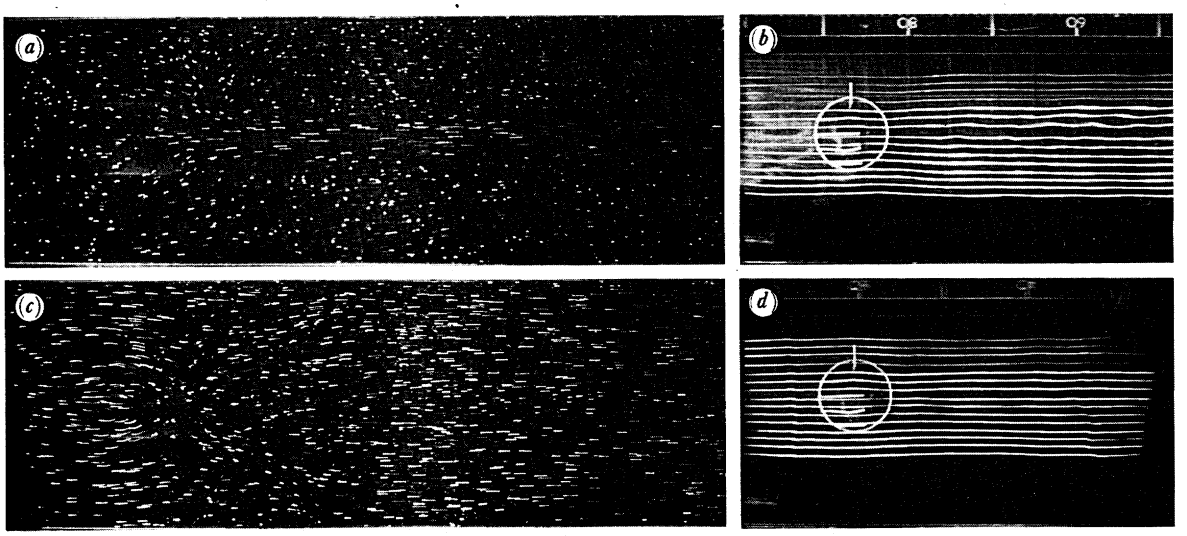

FIGURE 11. Some comparisons between streakline and particle streak photographs of non-rotating flow past cosine-squared obstacle for Re, Fr values of (*a*) 520, 0.25, (*b*) 490, 0.31, (*c*) 1030, 0.51 and (*d*) 1000, 0.59 and for $z^*/h_0 = 1.46$. Geometrical parameters as in the legend of figure 8.

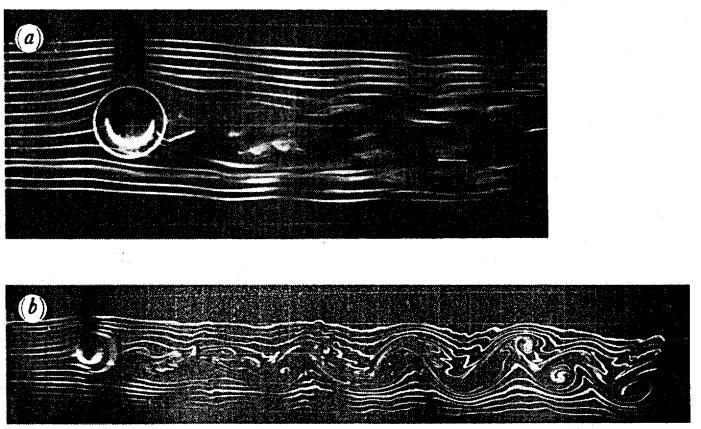

FIGURE 12. (*a*) Near-field and (*b*) far-field streakline patterns for rotating homogeneous flow past conical obstacle; $Ro = 0.20$, $Ek = 1.6 \times 10^{-4}$, $Re = 1100$, $S = 0.0$, $Fr = \infty$ and $z^*/h_0 = 0.46$. Geometrical parameters as in the legend of figure 4.

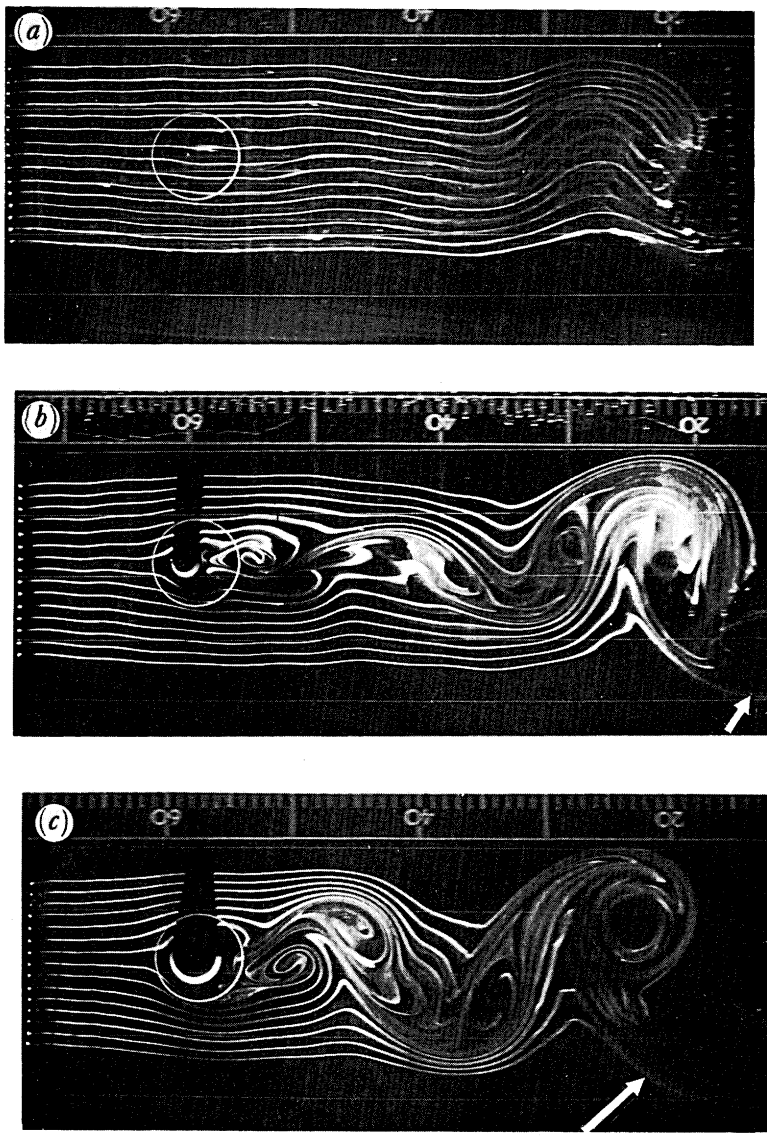

FIGURE 13. Streakline photographs for rotating, stratified flow past conical obstacle with $Ro = 0.13$, $Ek = 3.1 \times 10^{-4}$, $Re = 370$, $S = 3.1$ and $Fr = 0.09$. Geometrical parameters as in the legend of figure 4. Arrows on (*b*) and (*c*) indicate initial cyclonic disturbance.

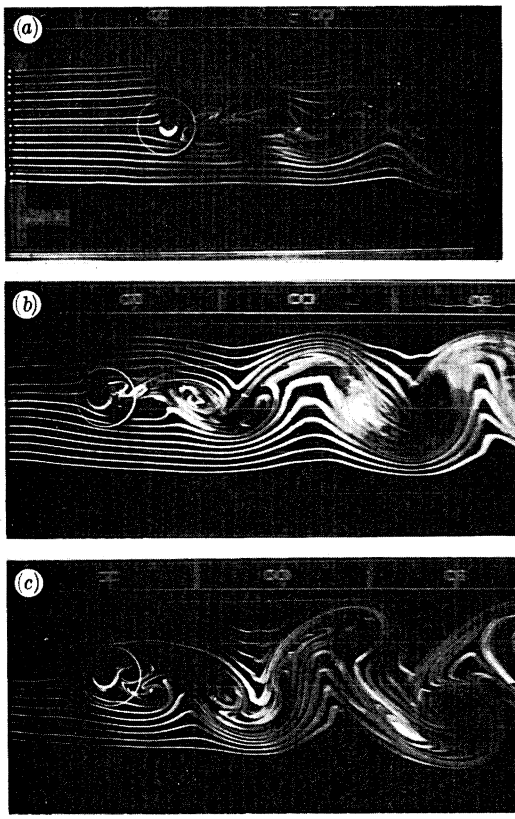

Ro	*Ek*	*S*
∞	∞	∞
0.26	3.1×10^{-4}	3.0
0.13	1.5×10^{-4}	1.1

FIGURE 14. Streakline photographs showing effects of increasing ω upon rotating, stratified flow past conical obstacles for $Re = 740$, $Fr = 0.17$ and $z^*/h_0 = 0.76$. Geometrical parameters as in the legend of figure 4.

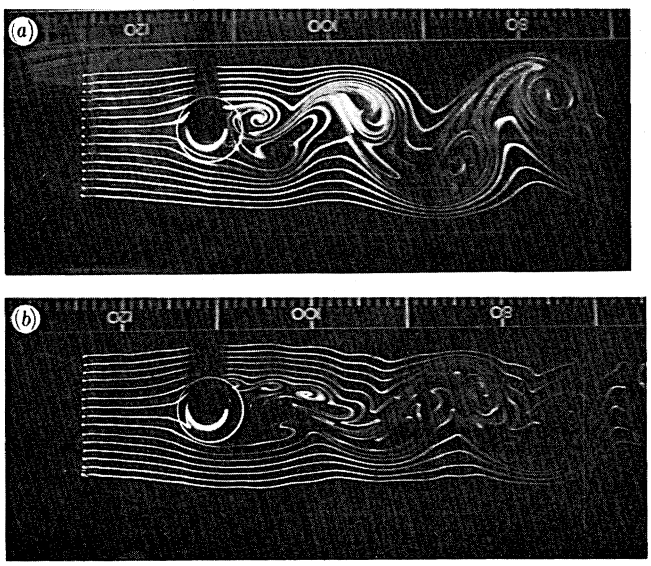

Ro	*Ek*	*S*
0.13	3.1×10^{-4}	3.12
0.06	1.5×10^{-4}	0.85

FIGURE 15. Streakline photographs showing effects of increasing ω upon rotating stratified flow past conical obstacles for $Re = 360$, $Fr = 0.09$ and $z^*/h_0 = 0.46$. Geometrical parameters as in the legend of figure 4.

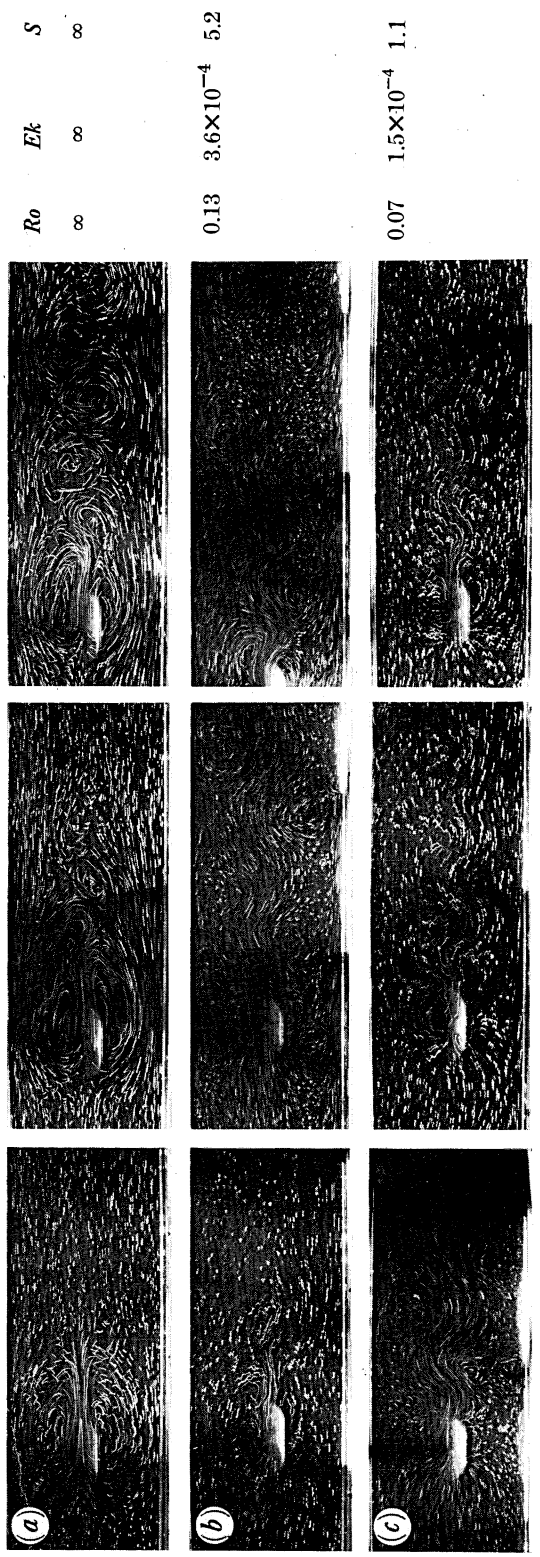

FIGURE 16. Time sequences of particle streak photographs for rotating stratified flow past conical obstacle for $Re = 370$, $Fr = 0.08$ and $z^*/h_0 = 0.15$. Geometrical parameters as in the legend of figure 4.

Figure 17. Time sequences of particle streak photographs for rotating stratified flow past conical obstacle for $Re = 390$, $Fr = 0.08$ and $z^*/h_0 = 0.51$. Geometrical parameters as in the legend of figure 4.

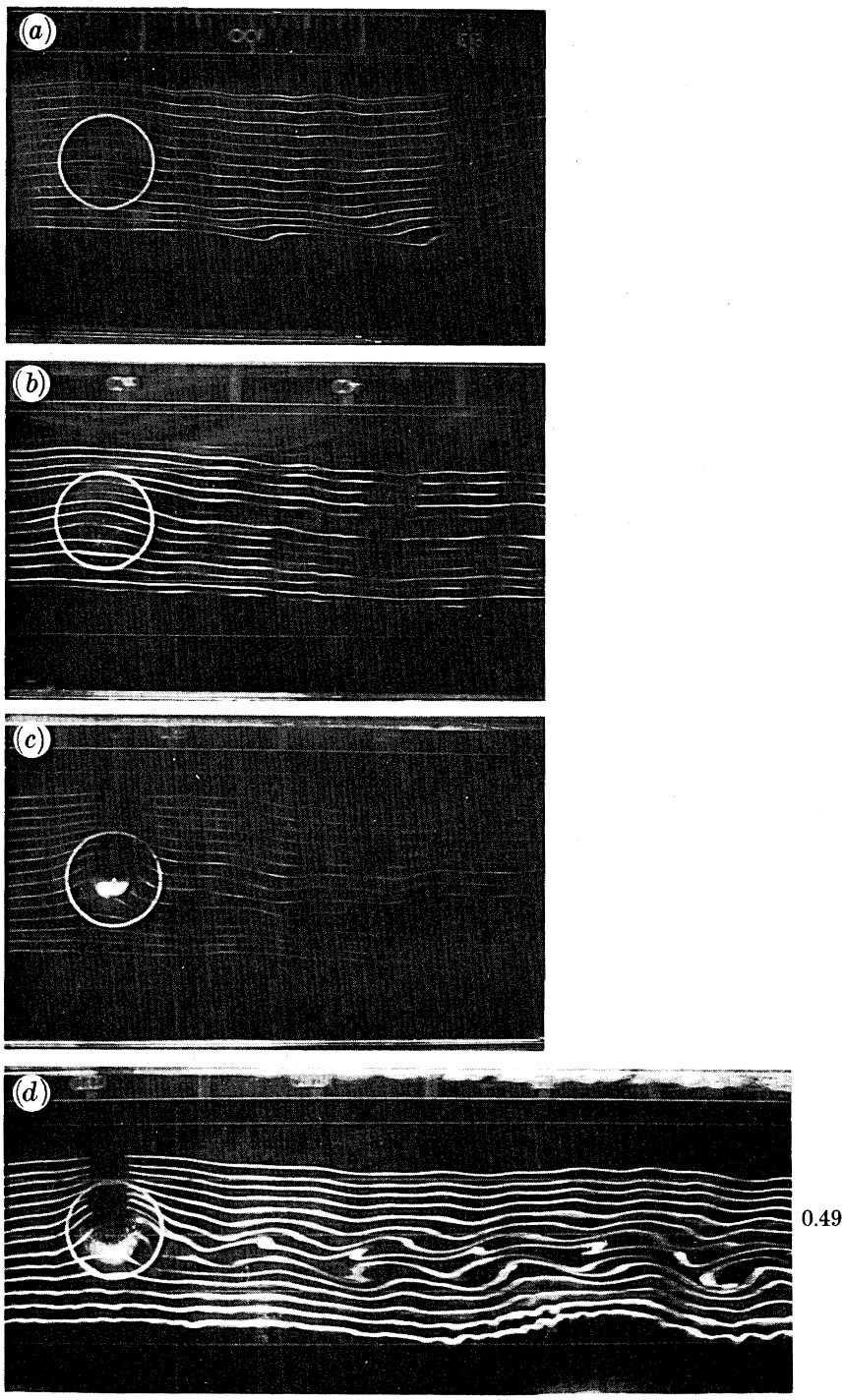

FIGURE 19. Streakline photographs for rotating stratified flow past cosine-squared topography with $Ro = 0.10$, $Ek = 1.6 \times 10^{-4}$, $Re = 950$, $S = 0.47$ and $Fr = 0.57$. Geometrical parameters as in the legend for figure 8.

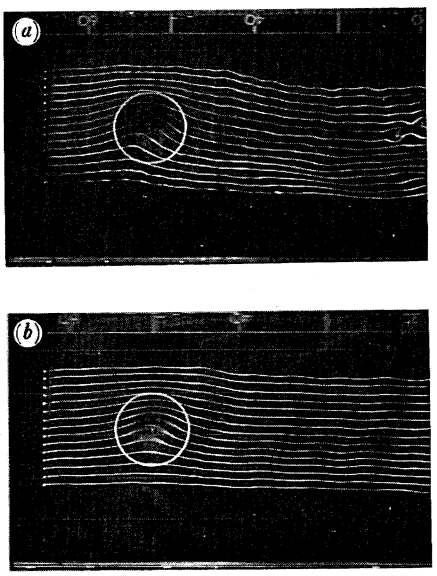

Ro	*Re*	*Fr*
0.05	450	0.39
0.10	900	0.82

FIGURE 20. Streakline photographs showing effects of increasing U upon rotating stratified flow past cosine-squared topography for $Ek = 1.7 \times 10^{-4}$, $S = 0.24$ and $z^*/h_0 = 1.46$. Geometrical parameters as in the legend for figure 8.

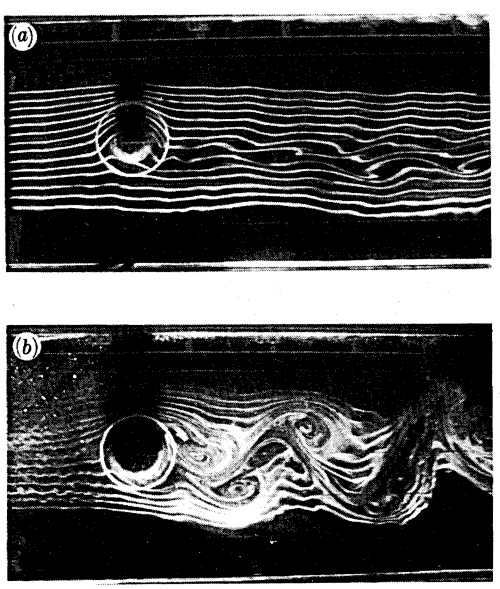

S	*(Fr)*
0.54	(0.53)
3.8	(0.20)

FIGURE 21. Streakline photographs showing effects of increasing $\Delta\rho/\rho_0$ upon rotating stratified flow past cosine-squared topography for $Ro = 0.10$, $Ek = 1.6 \times 10^{-4}$, $Re = 950$ and $z^*/h_0 = 0.49$. Geometrical parameters as in the legend for figure 8.

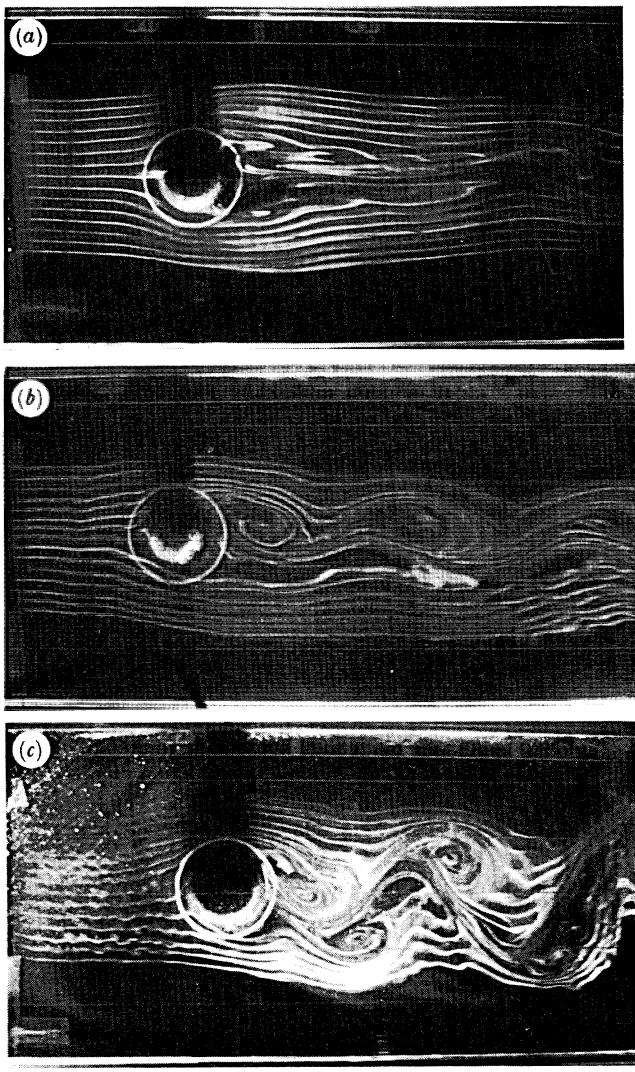

Ro	*Ek*	*S*
∞	∞	∞
0.20	3.2×10^{-4}	14.6
0.10	1.6×10^{-4}	3.8

FIGURE 22. Streakline photographs showing effects of increasing ω upon rotating stratified flow past cosine-squared topography for $Re = 980$, $Fr = 0.20$ and $z^*/h_0 = 0.49$. Geometrical parameters as in the legend for figure 8.

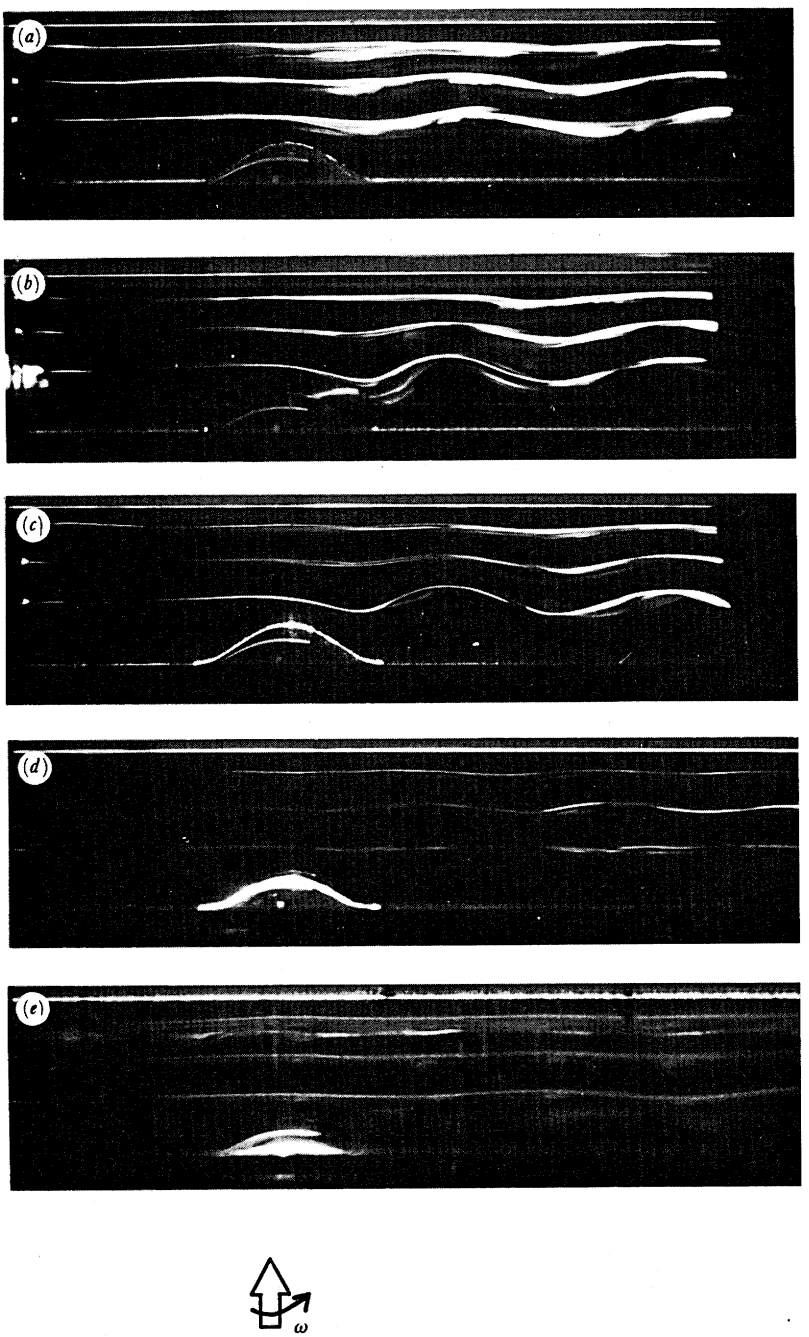

FIGURE 23. Side elevation photographs of lee waves generated by cosine-squared topography for $Ro = 0.30$, $Ek = 3.0 \times 10^{-4}$, $Re = 1510$, $S = 1.7$, $Fr = 0.92$, $z^*/h_0 = 1.46, 2.43, 3.40$ and for $y/(\frac{1}{2}D)$ of (*a*) -0.8, (*b*) -0.4, (*c*) 0.0, (*d*) 0.4 and (*e*) 0.8. Geometrical parameters as in the legend for figure 8.

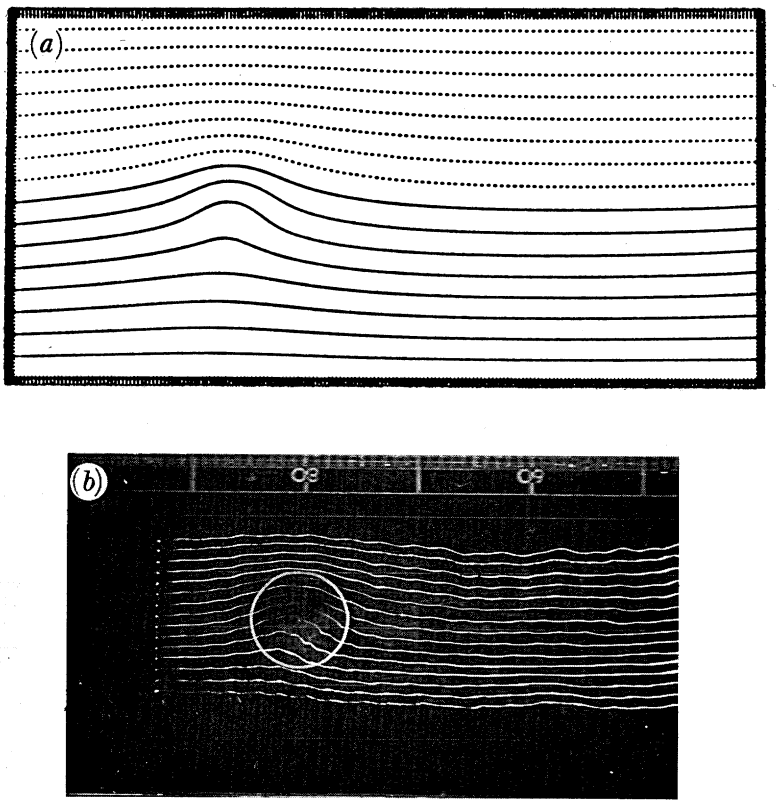

FIGURE 30. A comparison of (*a*) laboratory and (*b*) numerical model streamlines at a height of 3 cm above the bottom, for numerical experiment 1 parameters (see table 1).

With a view to examining the variation of horizontal flow patterns with elevation, a series of experiments with neutrally buoyant tracer particles was conducted. Figure 6, plate 3, depicts such experiments for a fixed speed ($U = 0.5$ cm s^{-1}) and stratification ($\Delta\rho/\rho_0 \approx 0.7\,\%$), at various observation levels, z^*/h_0, of 6*a*, 0.88; 6*b*, 0.46; and 6*c*, 0.15. The photographs are obtained by taking short time exposures of the moving tracer particles with a camera that is at rest with respect to the channel; i.e. the cone is moving with respect to the camera and is indicated by the broad, blurred, white horizontal streaks in the central section of each of the photographs. The elapsed dimensionless time $\tau = tU/D$ is given in the lower portion of the figure. The dimensionless boundary layer thicknesses at $\tau = 12.3$, 16.3 are approximately $\delta/h_0 = 0.17$, 0.24, respectively, so that the flow patterns of the last two photographs of figure 6*c* are embedded in the upper portions of the boundary layer.

Some deformation of the flow field is in evidence at all observation levels, but is quite weak at the upper level (see figure 6*a*). We note that the flow in the early stages of development at the lowest two levels (figures 6*b*, *c*) is characterized by symmetrical starting eddies that remain attached to the moving obstacle and elongate progressively with time. This elongated pair subsequently separates asymmetrically and a sinuous wake with alternating eddies is formed. Measurements of the characteristic retention times (i.e. the time taken for the first separation to occur), τ_r, for this and other similar experiments at different free stream speeds, U, suggest that $\tau_r \approx D/U$ with a constant of proportionality of *ca.* 10. Note that at the upper level (figure 6*a*) the principal motion is a streamwise current caused by the drag of the cone and that this wake develops a small horizontal oscillatory motion at large times.

A comparison between the flow at the two lowest observation levels in this and other similar experiments reveals a strong coherence in the vertical structure of the wake both with regard to the eddy formation – elongation phase and to the eddy-shedding process. The latter property of the flow is in consonance with the results of Brighton (1978), who found that for weakly stratified flow the shedding frequency of the eddies behind a cone was independent of height. This finding contrasts with the results of Gaster (1969) for homogeneous flows that indicated that the shedding frequency for slender cones was determined by the local cone diameter at each level. Observations from the experiments depicted in figure 6 and others reveal that the axes of the shed vortices are curved downstream and towards the plane $y = 0$, a finding also reported by Brighton (1978); see the schematic representation in figure 7.

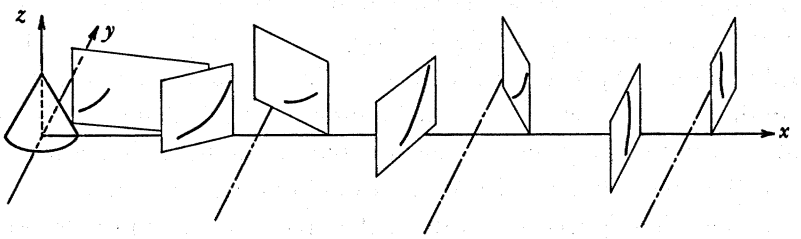

FIGURE 7. Schematic diagram indicating tilting of vortex cores downstream of cone.

4.1.2. *Cosine-squared topography*

The programme of experiments with the smooth, shallow cosine-squared topography followed essentially the same course as the cone studies, but had as an additional objective the investigation of the flow structure at levels in the fluid well above the top of the obstacle. The

principal reason for including these non-rotating studies was to compare the resulting flow structures with those obtained in rotating cases where topographic steering was anticipated. The obstacle took the form $(z/h_0) = \cos^2(\pi r/D)$, with h_0 and D having values of 2.00 cm and 10.08 cm, respectively.

The flow at five reference levels (two below the top of the obstacle and three above it) were recorded. In the upper layers of the fluid, particularly for the small Froude-number cases, the presence of the obstacle produced no noticeable effects upon the horizontal streakline patterns; i.e. the streaklines passed over the region above the obstacle without noticeable deflection. However, for flows at relatively larger Froude numbers, three-dimensional lee waves generated by low-level interactions of the flow with the solid obstacle could be detected in the upper levels. Figure 8, plate 4, is an example of a lee-wave case where the observation level is well above the top of the obstacle (i.e. $z^*/h_0 = 1.46$). The wave is made visible by the vertical excursions of the horizontally injected streaklines above and below the horizontal light beam illuminating the flow. The values of the Froude numbers for which lee waves were generated were compatible with the results of Hunt & Snyder (1980) and others who found that for smooth topographies a critical value of $Fr \approx 0.4$ delineated the approximate boundary between flow régimes in which flow passed predominantly over the obstacle ($Fr > 0.4$) and around it ($Fr < 0.4$) respectively, with lee-wave generation being favoured by the former circumstance.

The horizontal flow patterns at levels below the mountain top for cases in which the flow is predominantly around and over, respectively, are now investigated. Figure 9, plate 5, depicts the (i) near and (ii) far fields of a series of experiments at two different speeds ($U = 1.0$, 1.5 cm s^{-1}), with stratification, $\Delta\rho/\rho_0 \approx 5.7\,\%$ and at observation levels below the crest of the topography; $Fr < 0.4$ for all cases (see legend). We note that the near fields exhibit a sinuous nature whereas the far fields develop into a vortex street. These observations are qualitatively similar to the wake characteristics for the stratified cases of flow past a cone as shown in figure 4*b*, *c*.

Figure 10, plate 6 , also depicts a series of experiments for $U = 1.0$, 1.5 cm s^{-1}, but now with a smaller stratification, $\Delta\rho/\rho_0 \approx 0.7\,\%$, than that in figure 9. The observation levels are the same, but the Froude numbers are now much larger (i.e. $Fr > 0.4$). For these large Fr cases the flow in the lowest level forms a separated region in the lee of the obstacle for both Reynolds numbers. The flow then reverts rapidly to a relatively undisturbed state of smooth streamwise streaklines. The downstream extent of the separation bubble for such a flow increases with increasing Reynolds number in much the same manner as for homogeneous flow past circular cylinders in rotating and non-rotating fluids (Boyer & Davies 1982). Near the level of the top of the topography (figure 10*a*, *b*) the incident streaklines are deflected only slightly by the solid boundary; note that for the lowest Reynolds-number case this deflection is almost imperceptible. The local deformation produced by the interaction produces little downstream effect, and for both cases the laminar wake consists of a series of parallel streaklines.

Whereas streakline photographs for both weakly and strongly stratified flows showed little horizontal deflections for the cosine-squared topography when the observation levels were above the feature, a series of experiments were conducted with neutrally buoyant tracer particles to further investigate this region. Figure 11, plate 7, depicts comparisons between the streakline and particle methods of flow visualization for an observation level of $z^*/h_0 = 1.46$ and for two sets of Re, Fr combinations; i.e. $Re \approx 500$, $Fr \approx 3.0$ (figure 11*a*, *b*) and $Re \approx 1000$, $Fr \approx 0.55$ (figure 11*c*, *d*). One notes from these experiments that the particle streaks give more detail than the streakline patterns. For example, when the Reynolds number is sufficiently low,

a definite streamwise current caused by the drag of the obstacle is in evidence in the particle photograph (figure 11*a*) but not in the corresponding streakline photograph (figure 11*b*).

As the Reynolds and Froude numbers are increased, more flow is forced over the topography for otherwise identical conditions, and the thin streamwise current formed by the drag of the topographic feature disappears (see the particle photograph, figure 11*c*). At these larger *Re*, *Fr* combinations, however, three-dimensional lee-wave patterns begin to appear as evidenced by the streakline photograph of figure 11*d*. Note that with the particles being distributed quite uniformly throughout the fluid, the horizontal particle photographs show no evidence of the lee wave pattern; such effects can be demonstrated with tracer particles by using a vertically oriented streamwise sheet of light, and photographing this vertical section (see figure 23, plate 15, below).

Hunt & Snyder (1980) have shown that for non-rotating stratified flow over a bell-shaped hill and for $Fr > 0.4$, there is a region above the obstacle of thickness $O(h_0/Fr)$ within which the initially horizontal incident streaklines are affected by the presence of the obstacle. By using this relation, figure 11*c*, *d* should not be affected at the $z^*/h_0 = 1.46$ level, and the experiments so indicate.

4.2. *Rotating, linearly stratified flows*

The effects of rotation were studied by choosing reference rotation rates, ω, of 0.25 and 0.5 s^{-1}, varying the normalized vertical-density difference, $\Delta\rho/\rho_0$, from 0.3 to 5.0% (as well as investigating homogeneous flows), and considering free stream speeds, U, of 0.5, 1.0 and 1.5 cm s^{-1}. The ranges of the Rossby, Ekman and Burger numbers investigated were thus: cone ($0.07 < Ro < 0.40$, $1.5 \times 10^{-4} < Ek < 3.0 \times 10^{-4}$ and $0.9 < S < 36.0$) and cosine-squared ($0.05 < Ro < 0.30$, $1.5 \times 10^{-4} < Ek < 3.0 \times 10^{-4}$ and $0.39 < S < 17.5$).

The range of U was limited by practical considerations; namely, requirements that the belt motion be steady ($U \geqslant 0.5$ cm s^{-1}) but sufficiently slow for dye tracer streaks to be clearly visible ($U \leqslant 1.5$ cm s^{-1}). The upper limit on the rotation rate of $\omega \leqslant 0.5$ s^{-1} was established to ensure that centrifugal effects would be negligible (see, for example, Boyer & Biolley 1986).

Studies with stratified non-rotating fluids, as exemplified by those discussed above, have demonstrated that the nature of the starting flow and of the character of the downstream wake are sensitive to the degree of stratification in the fluid. This is principally due to the tendency of stratification to suppress vertical motion. If the fluid is also rapidly rotating ($Ro \ll 1$, $Ek \ll 1$), the constraints of geostrophy further inhibit vertical motions. Boyer & Biolley (1986), for example, have shown that for other parameters fixed, the waves in the lee of stratified flow over a long ridge can be suppressed at sufficiently small Rossby numbers. The combination of rotation and stratification on the flow past isolated topography thus tends to produce more nearly two-dimensional horizontal motions than would be present should these factors be considered separately.

In the non-rotating stratified flows, it was noted that the boundary layer above the belt grows with time according to $(\nu t)^{\frac{1}{2}}$. For the rotating experiments, these horizontal boundary layers grow to steady-state Ekman layers of thickness $\delta_E \approx (\nu/\omega)^{\frac{1}{2}}$ (approximately 1–2 mm for the rotation rates considered) in a time scale, $\tau_E \approx \omega^{-1}$; 'steady state' is reached in the present facility well before the obstacle traverses one-half of the channel (Boyer & Kmetz 1983). This inherent difference in boundary layers must be considered when comparing rotating and non-rotating flow patterns especially those near the end of the obstacle traverse in the non-rotating case.

4.2.1. *Homogeneous rotating flows: conical obstacle*

Previous experimental studies (Boyer 1968; Boyer & Davies 1982; Boyer *et al.* 1984) of high Reynolds number, homogeneous, rotating flows past isolated solid obstacles have been limited to two-dimensional topographies (upright cylinders). In these cases, it has been shown that the presence of rotation affects the transition from separation to vortex shedding in the wake flow and, furthermore, that when shedding occurs, the cores of the cyclonic eddies have larger relative vorticities than their anticyclonic counterparts.

Figure 12, plate 7, depicts (*a*) near-field and (*b*) far-field observations from an experiment in which the dye tracer is introduced at about the mid-height of the cone. We note that the flow upstream of the obstacle veers to the left, and that the streamline separating flow passing to the left of the cone from that passing to the right has its upstream location to the right of the centre line passing through the cone axis. This is reminiscent of observations of the homogeneous rotating flow past shallow topographies, as discussed by Vaziri & Boyer (1971). The separated flow in the near-field wake (figure 12*a*) is quite irregular and does not show the development of a well-defined vortex street. Further downstream, however, the flow does begin to develop into a more organized pattern (i.e. a vortex street) as indicated in figure 12*b*. In this and other homogeneous experiments, there was no clear indication of the cyclone–anticyclone asymmetry noted above for right-circular cylinders of uniform cross section.

4.2.2. *Linearly stratified flows: conical obstacle*

Figure 13, plate 8, depicts a series of experiments for flow past a cone in which the observation level is varied and the free stream speed, $U = 0.5$ cm s^{-1}, rotation rate, $\omega = 0.25$ s^{-1}, and stratification, $\Delta\rho/\rho_0 \approx 0.6\%$, are fixed; the photographs are all taken when the obstacle has completed approximately one-half of the traverse through the channel.

Conservation of potential-vorticity arguments suggest that fluid columns initially above the cone before the impulsive start of the topography should experience cyclonic relative vorticity as they are advected downstream. This effect can be noted in the two lowest observation levels in figure 13. This observation is in qualitative agreement with numerical experiments on a similar physical system discussed by Huppert & Bryan (1976). We note, however, that this initially shed cyclone (indicated by arrows on figure 13*b*, *c*) is relatively weak and that the first strong shed eddy is an anticyclone. This initial downstream advection of a weak cyclonic disturbance followed by a strong anticyclone was also observed for the rotating homogeneous flow past a cone.

The experiments of figure 13*a*–*c* indicate the dramatic decrease in streakline deflection with height, in the wake. For example, the deflections just above the top of the cone (i.e. at $z^*/h_0 = 1.06$ in figure 13*a*) are seen to be very weak whereas strong eddy shedding occurs at lower levels (i.e. $z^*/h_0 = 0.46$ and 0.76 in 13*b* and 13*c*, respectively). An analysis of these and other experiments shows that the shed eddies, especially in the lower layers slope downstream and towards the streamwise plane of symmetry ($y = 0$) as shown schematically in figure 7. Furthermore, as indicated in figure 7, the eddy axes become more vertically oriented far downstream. There is no apparent difference in the core strengths of the cyclones and anticyclones, in contrast with the study cited earlier for homogeneous rotating flow past circular cylinders (Boyer *et al.* 1984).

Figures 14 and 15, plate 9, demonstrate effects of increased rotation upon flows with relatively

small flows with relatively small $\Delta\rho/\rho_0 \approx 0.6\%$. In each figure, the flow velocity (and hence the Reynolds number) remains fixed but Ro, Ek and S all decrease as ω increases; $U = 1.0$ cm^{-1} in figure 14, and $U = 0.5$ cm^{-1} in figure 15. The most apparent manifestation of the increase in ω in figure 14 is the increased lateral extent of the downstream streaklines at a given reference level, in this case $z^*/h_0 = 0.76$. In these experiments, although $S \approx O(1)$, the background rotation is able to exert a strong control over the large-scale structure of the flow by establishing a weak Taylor column (Davies 1972) above the cone. The presence of such a feature, at relatively high values of ω, results in an increase in the effective obstacle diameter and hence in the lateral extent of the vortex street.

For the lower Reynolds number experiments of figure 15 (observation level, $z^*/h_0 = 0.46$), rotation can decrease the 'strength' of the vortex street. For small Reynolds numbers and large rotation rates (i.e. very small Ro) the Taylor column can become quite strong, and separation is inhibited in much the same way as that observed for the circular cylinder experiments of Boyer & Davies (1982). Merkine & Solan (1979) have predicted the tendency for separation to be inhibited from circular cylinders at sufficiently small Rossby numbers.

For the conical obstacle, the consequences of increasing the dominance of stratification over Coriolis, inertial and viscous forces (i.e. increasing S for constant Ro, Re and Ek) take the form of an increased tendency to flow in horizontal planes (as for the non-rotating cases described previously). In the upper layers of the fluid near the peak of the obstacle, the stronger stratification ensures that less fluid flows over the obstacle and, in consequence, the lateral extent of the downstream disturbance is wider than for cases of weaker stratification.

The time dependence of the motions are best observed by using particle-streak techniques. Figure 16, plate 10, and figure 17, plate 11, represent experiments conducted at fixed free stream speeds, $U = 0.5$ cm s^{-1}, and stratification levels, $\Delta\rho/\rho_0 \approx 0.8\%$. The observation level in figure 16 is deep in the fluid (i.e. $z^*/h_0 = 0.15$) whereas that in figure 17 is at approximately mid-height of the cone (i.e. $z^*/h_0 = 0.51$). The rotation rates, ω, in (a), (b) and (c) of each figure are 0.0, 0.25 and 0.50 s^{-1}, respectively. Thus the Rossby, Ekman and Burger numbers decrease, as indicated. The dimensionless observation time $\tau = Ut/D$ for each photograph is given in the figures.

Note first that the starting-eddy retention time, τ_r, is significantly shortened when the fluid is rotating; this can be seen by comparing the initial photographs in each experimental run. In the non-rotating cases (figures 16a and 17a), the initial eddies are shed somewhere between the first two photographs; the retention time, $\tau_r \approx 10D/U$, as stated earlier. In the rotating cases, the initial eddy has been shed before the first photograph. From experiments with photographs taken at earlier stages in the obstacle's motion, it may be concluded that the retention time scale for the rapidly rotating cases considered is given by the background rotation period; i.e. $\tau_r \approx 2\pi/\omega$. The data indicate a constant of proportionality of about unity.

We also note that for the $\omega = 0.25$ s^{-1} experiments (figures 16b and 17b), a well-defined vortex street is developed for this set of parameters ($Ro = 0.13$, $Ek = 3.6 \times 10^{-4}$, 3.0×10^{-4}, $S = 5.2$, 3.6). At the larger rotation rate of $\omega = 0.50$ rad s^{-1} (figures 16c and 17c, with $Ro = 0.07$, $Ek = 1.5 \times 10^{-4}$, $S = 1.1$) the increased effect of rotation has suppressed the vortex shedding and the flow is effectively attached to the obstacle. These observations are similar to the effects of increased rotation for right circular cylinders as found by Boyer (1968) and Boyer & Davies (1982).

The Strouhal number, $St = nD/U$, for eddy shedding from the cone, was measured by using

dye-streak and particle-track data; here, n is the shedding frequency from one side of the cone. The procedure adopted was to examine a sequence of photographs for which the time interval $[(\tau)_j - (\tau)_{j-1}]$ between successive ($j-1$ and j) frames was known, and to calculate the distance, l, a given vortex moved in the streamwise direction during this interval. The mean separation distance, X, between successive vortices on the same side of the street was measured and the frequency, n, could then be obtained from

$$n = l/[(\tau)_j - (\tau)_{j-1}]\, X. \tag{4.1}$$

For each sequence of photographs, a mean value of St was obtained by using the data from all shed eddies of the experiment.

Figure 18 is a plot of the Strouhal number as a function of the Burger number for the cone for all values of Ro, Ek and Re investigated; in the figure, note that the different symbol shapes depict different Rossby numbers, the symbol shading delineates the Reynolds number, and the presence or absence of a tilde denotes the Ekman number. Whereas St may be a mildly decreasing function of S, it appears to be essentially independent of Ro, Ek and Re.

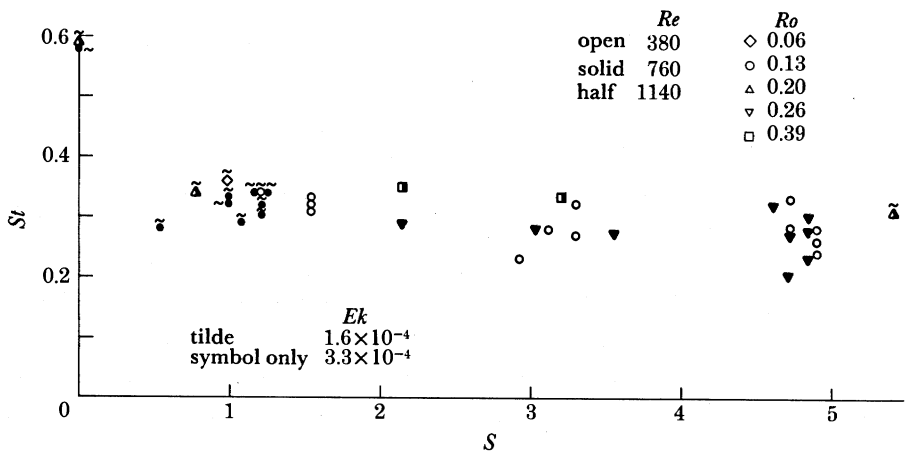

FIGURE 18. Plot of Strouhal number against Burger number for cone and for various Ro, Ek and Re. Geometrical parameters as in the legend of figure 4.

It is of interest to note that the Strouhal numbers obtained above are consistently less than those obtained by Brighton (1978) for his non-rotating studies with conical obstacles. In the Brighton investigation, values of St ranging from 0.35 to 0.47 were measured for the 'symmetric instability' and vortex-shedding régimes respectively, over a range of Fr and Re comparable with the present study.

4.2.3. *Linearly stratified flows: cosine-squared obstacle*

The initial objective in this series of experiments was to examine the vertical attenuation of the steering effect with height for fixed geometry and Ro, Ek and S. Davies (1972), by using spherical obstacles, has shown that such flows are attenuated with height, z^*/h_0, until a cut-off value is reached above which incident horizontal streaklines are essentially unaffected by the bottom topography.

The experiments depicted in figure 19, plate 12, are for a fixed free stream speed

$U = 1.0$ cm s^{-1}, and for a relatively small proportional density stratification, $\Delta\rho/\rho_0 \approx 0.6\%$. The observation levels z^*/h_0 are (2.43, 1.46, 1.00 and 0.49) for figures 19*a–d*, respectively. At the lowest level (figure 19*d*), the incident flow is forced around the obstacle with a pattern similar to that found by Vaziri & Boyer (1971) for homogeneous flow past shallow topography. Above the topography, the flow is seen to be deflected at all levels by the Coriolis forces associated with the background rotation, in the same general manner as for the conical obstacle in figure 13. The deflections of such slow, steady flows at low Rossby numbers are well predicted by quasigeostrophic theory, as will be shown in §5.

The effect of varying free stream speed (0.5 and 1.0 cm s^{-1}) for fixed rotation, $\omega = 0.25$ s^{-1} and proportional stratification, $\Delta\rho/\rho_0 \approx 0.5\%$, is demonstrated in figure 20, plate 13. Here the observation level is $z^*/h_0 = 1.46$, and greater deflections for the lower Rossby number case are noted.

It is of interest to investigate the characteristic motion changes for fixed rotation and free stream speed and varying stratification. Figure 21, plate 13, depicts two experiments for $U = 1.0$ cm s^{-1}, $\omega = 0.50$ rad s^{-1} and $\Delta\rho/\rho_0 \approx 0.7\%$ (figure 21*a*) and 5.0% (figure 21*b*), respectively; the observation level is at about half the mountain height, $z^*/h_0 = 0.49$. Note that for the relatively weak stratification case, $S = 0.54$ (figure 21*a*) the flow goes 'over and around' the body with the general anticyclonic curvature above the obstacle characteristic of rotating flows. With the high stratification flow, $S = 3.8$, however, the obstacle blocks the flow to a much greater degree, forces more of the fluid around the topography and hence effectively presents a much larger obstruction to the free stream motion than in the lower stratification case. At a fixed free stream speed then, the wake pattern develops a strong vortex street in the lower levels as $\Delta\rho/\rho_0$ is increased.

Similar effects can be noted for cases in which the stratification and free stream speed are fixed and the rotation is increased. Figure 22, plate 14, depicts a series of experiments in which again the observation level is $z^*/h_0 = 0.49$, $U = 1.0$ cm s^{-1} and $\Delta\rho/\rho_0 \approx 5.0\%$. The rotation rate, ω, has the values of (0.0, 0.25, 0.50 s^{-1}) in figure 22*a–c*, respectively. As the rotation is increased, other factors being fixed, the Taylor–Proudman column effect becomes increasingly important and the obstacle presents a successively larger obstruction to the free stream flow. The flow thus goes from one in which much of the fluid goes over the feature (figure 22*a*) to one in which most goes around (figure 22*c*). With more flow going around, the effective Reynolds number again is larger and a vortex streak is seen to develop.

The experiments described in §4.1.2 indicate that the presence of an isolated cosine-squared topography in a stratified flow caused three-dimensional lee waves to be generated in the fluid. Such lee waves also appear when the stratified fluid is rotating. The spatial characteristics, however, are modified considerably by the rotational constraint. Figure 23, plate 15, represents a series of experiments in which a vertically oriented sheet of light is used to indicate the lee-wave structure along various planes perpendicular to the y-axis. Dye tracers are introduced at the vertical locations $z^*/h_0 = (1.46, 2.43, 3.40)$. The positions of the dye-tracer sources are at the far left of each photograph; these locations are clearly seen (the white dots) in the upper photograph, for example. The dark areas along some of the streaklines are due to horizontal excursions of the dye tracer away from the light sheet. The principal effect of rotation is to develop an asymmetry in the lee-wave amplitude across the wake. In particular, the largest amplitudes are observed on the right side of the obstacle looking downstream; compare, for example, the photographs for $y/(\frac{1}{2}D) = -0.4$ and $+0.4$. The asymmetric nature of the lee waves

can be understood in terms of horizontal flow patterns such as shown in figure 20. Rotation tends to deflect the incident flow to the right when crossing over the topography. Because the value of $Fr = 0.92$ in figure 23 is significantly higher than the 'critical' value of $Fr = 0.4$ for the non-rotating case, the incident flow is not only deflected rightwards because of Coriolis force effects, but is also diverted over, rather than around, the obstacle. Strong lee waves are thereby generated in the downstream region on the right into which most of the descending fluid has been directed.

4.3. *Flow-régime diagrams*

The matter of developing flow-régime diagrams for the present physical system is complicated by the large number of dimensionless parameters, and by the fact that the flows are highly three-dimensional in nature. For both the conical and cosine-squared obstacles three characteristic flow patterns are defined.

The first is a flow in which the wake motion is steady and for which eddies will typically be attached to the downstream portion of the obstacle. This régime is designated steady, and is exemplified by figure 10 for the cosine-squared topography (for the range of parameters investigated, no steady motions were observed for the cone). The second characteristic flow is designated as varicose, above. In such a flow, the wake is unsteady but no vortex street within one or two diameters downstream of the topography is in evidence. Examples of such flows for the cone and cosine-squared topographies are given respectively in figures 5 and 9i. Flows that are varicose near the topography but develop into vortex streets far downstream are designated as varicose; see, for example, figure 9ii. Finally, flows for which vortices shed

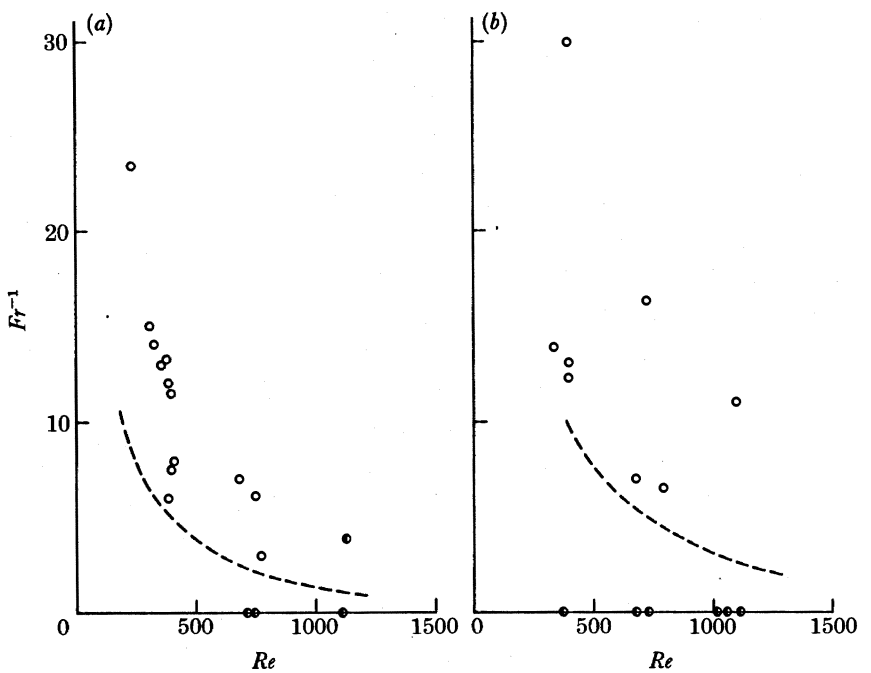

FIGURE 24. Flow régime diagram of Fr^{-1} against Re for conical obstacle for Ek values of (*a*) 3.0×10^{-4} and (*b*) 1.5×10^{-4}. Symbols: ◐, varicose; and ○, vortex street (see text). Geometrical parameters as in the legend for figure 4.

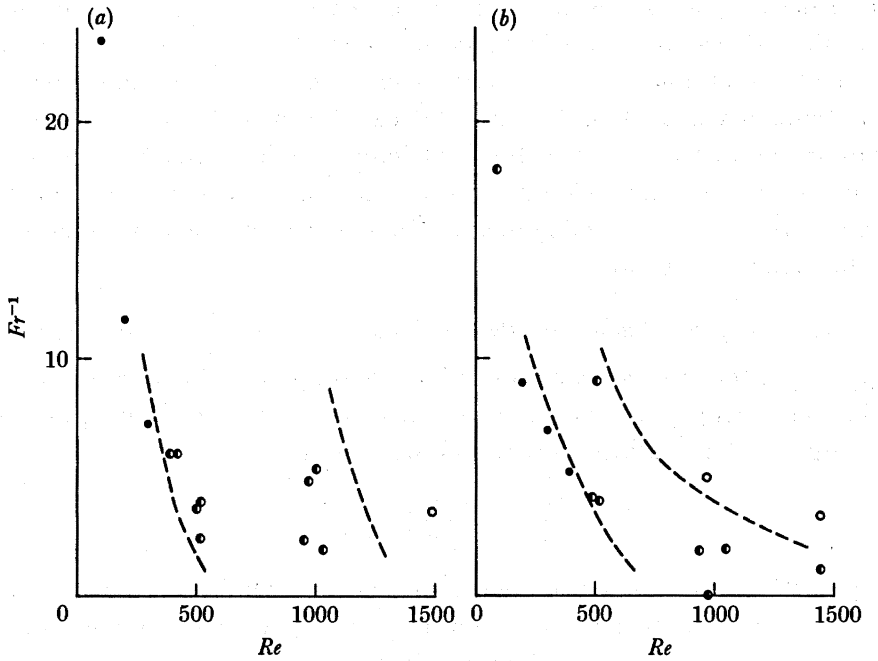

FIGURE 25. Flow régime diagram of Fr^{-1} against Re for cosine-squared topography for Ek values of (*a*) 3.0×10^{-4} and (*b*) 1.5×10^{-4}. Symbols: ●, steady; ◐, varicose; and ○, vortex street (see text). Geometrical parameters as in the legend for figure 8.

alternately immediately downstream of the obstacle are termed as a vortex-street régime. Figures 13 and 21*b* are examples for the cone and cosine-squared topographies, respectively.

In determining the flow régimes for the cone, photographs at a fixed observation level $z^*/h_0 = 0.46$ (at about mid-height) were used. Figure 24*a*, *b* shows the Fr^{-1} against Re flow-régime diagrams so-obtained for $Ek \approx 3.0 \times 10^{-1}$ and $Ek \approx 1.5 \times 10^{-4}$, respectively. As one notes, all of the observations indicated are designated as either varicose or vortex street. As discussed above, increased rotation (smaller Ek) at low Reynolds numbers ($Re < 500$) had a tendency to stabilize the wake and shift the flow from vortex street to varicose.

The observations for obtaining the cosine-squared Fr^{-1} against Re flow-régime diagrams were made at $z^*/h_0 = 0.5$, a level above the Ekman boundary layers. The resulting diagrams for $Ek \approx 3.0 \times 10^{-4}$ and $Ek \approx 1.5 \times 10^{-4}$, respectively, are shown in figure 25*a*, *b*. As should be expected, for fixed Fr^{-1} and Ek, increased Reynolds numbers result in moving from steady to varicose to vortex shedding. Similarly, for fixed Re and Ek and increasing Fr^{-1} (increased stratification), the flow will tend to become more unstable; i.e. a varicose motion develops into a vortex street at increased stratification levels, other parameters being fixed. The data on the effect of rotation (variable Ek) at fixed Fr^{-1} and Re are too limited to draw firm conclusions.

5. NUMERICAL MODELLING

Some aspects of stratified, rotating flow over topography can be modelled with quasigeostrophic (hereafter QG) physics (Pedlosky 1979; Holland 1978). In particular, for small Rossby number and small amplitude topographic relief, the behaviour of the flow is governed by the

QG potential vorticity equation. In this case, the local vorticity tendency is given by several contributions: the advection of vorticity, vortex-tube stretching due to variable depth, Ekman-layer pumping on the lower boundary (assume that the lower boundary is rigid and that the upper boundary is free), and frictional decay. Boyer *et al.* (1984) used such a model to examine rotating flow past discs and cylindrical depressions in a homogeneous fluid including a β-effect simulated by a variable-depth cross section. They showed a close correspondence between selected laboratory flows and numerical simulations, and used the numerical solutions to delve into the dynamical balances.

5.1. *The quasigeostrophic potential-vorticity equation with friction, stratification and topography*

Consider a comparison between laboratory flows and numerical experiments over isolated topography in a channel geometry for the stratified case without β (that is, on the f-plane). The vorticity equation for stratified flow can be written as

$$\frac{\mathrm{D}\zeta}{\mathrm{D}t} = 2\omega\frac{\partial w}{\partial z} + \nu\nabla^2\zeta, \tag{5.1}$$

where $\zeta = \nabla^2\psi$, is the vorticity of the nondivergent geostrophic flow, ψ is the QG streamfunction with horizontal velocity components $u = -\partial\psi/\partial y$, $v = \partial\psi/\partial x$, and w is the upward vertical velocity in the interior. As before, ω is the rate of rotation and ν is the viscosity. A coordinate system has been chosen with x positive to the right in the channel (downstream), and y cross channel. The vertical coordinate z goes from $-H_{\mathrm{B}}(x,y)$ at the bottom, to zero at the top of the fluid. The vorticity equation is supplemented by a buoyancy tendency equation in the interior of the fluid given by

$$\mathrm{D}h/\mathrm{D}t = w, \tag{5.2}$$

where h is the perturbation (upward) of constant density surfaces from their level, undisturbed configuration. The equation set is closed by the thermal wind relation that relates lateral gradients of the density perturbations to vertical shear of the horizontal velocity (derived from geostrophic and hydrostatic relations); i.e.

$$\psi_z = \frac{g}{2\omega}\frac{\mathrm{d}\bar{\rho}}{\mathrm{d}z}h. \tag{5.3}$$

Here g is gravity and $\mathrm{d}\bar{\rho}/\mathrm{d}z$ is the horizontally averaged mean static stability of the fluid.

The boundary conditions on w at the bottom introduce the effects due to bottom topography and Ekman-layer pumping (Pedlosky 1979). At the bottom

$$w(x,y,-H_{\mathrm{B}}) = J(\psi,H_{\mathrm{B}}) + \frac{1}{2}\left(\frac{\nu}{\omega}\right)^{\frac{1}{2}}\nabla^2\psi. \tag{5.4}$$

At the free surface, $w(x,y,0) = 0$.

In addition to the top and bottom boundary conditions, there are inflow, outflow and side-wall conditions on velocity and vorticity. At both the upstream and downstream ends, a uniform flow ($u = U$ = constant) is specified. At the upstream end, the vorticity is set to zero, whereas at the downstream end the gradient of potential vorticity (defined below) is set to zero. This last condition is a simple extrapolation technique that allows transients generated at the bump to advect out of the domain. Little reflection of energy back into the region of interest is found, and this condition is judged to be sufficiently effective for the present problem in which advection is the only process by which energy is carried from one part of the fluid to another.

Equations (5.1)–(5.4), together with the boundary conditions, define an initial-value problem that describes the flow over the obstacle in terms of evolving streamfunction and vorticity fields.

5.2. *Numerical techniques*

The QG numerical model formulation with N arbitrary layers is a straightforward extension of the two-layer case described by Holland (1978). Here the form of the equations in which the vertical discretization has already been done are presented. The horizontal discretization and the form of the finite difference equations will not be discussed (the interested reader is referred to Chow & Holland (1986) who have recently described the physics and an efficient numerical code for solving this time-dependent boundary-value problem).

As discussed above, the governing equations are the vorticity and interface-height perturbation equations, and the thermal-wind relation. In discrete form, these are

$$\frac{\partial}{\partial t}\nabla^2\psi_k = J(\nabla^2\psi_k, \psi_k) + \frac{2\omega}{H_k}(w_{k-\frac{1}{2}} - w_{k+\frac{1}{2}}) + \nu\nabla^4\psi_k, \quad k = 1 \text{ to } N; \tag{5.5}$$

$$\frac{\partial}{\partial t}h_{k+\frac{1}{2}} = J(h_{k+\frac{1}{2}}, \psi_{k+\frac{1}{2}}) + w_{k+\frac{1}{2}}, \quad k = 1 \text{ to } N-1; \tag{5.6}$$

and

$$h_{k+\frac{1}{2}} = \frac{2\omega}{g'_{k+\frac{1}{2}}}(\psi_{k+1} - \psi_k). \tag{5.7}$$

Whole-number subscripts (k) denote the vertical layers (k increasing downward) in which the QG streamfunction is defined (nominally at the centre of each of the layers) whereas fractional subscripts ($k+\frac{1}{2}$) denote the interfaces between layers where the vertical velocity and the interface height perturbations are defined. The variables are the QG streamfunction, ψ_k, the interface-height perturbation, $h_{k+\frac{1}{2}}$, and the mean layer thicknesses, H_k. The basic background vertical stratification is written in terms of the reduced gravity $g' = g\Delta\rho_{k+\frac{1}{2}}/\rho_0$, where $\Delta\rho_{k+\frac{1}{2}}$ is the (positive) density difference between layers $k+1$ and k.

Topographic and bottom friction effects are taken care of by the bottom-boundary condition on w; i.e. $w_{N+\frac{1}{2}} = J(\psi_N, H_B) + (\epsilon_B H_N/2\omega)\nabla^2\psi_N$, where $H_B(x,y)$ is the variable bottom topography (positive upward) and ϵ_B is $(\nu\omega/H_N^2)^{\frac{1}{2}}$. At the surface of the fluid $w_{\frac{1}{2}} = 0$. The advective velocities at the interfaces, needed in (5.6), are calculated from a weighted average of the velocities in the layers; i.e. $\psi_{k+\frac{1}{2}} = \alpha_{k+\frac{1}{2}}\psi_{k+1} + (1-\alpha_{k+\frac{1}{2}})\psi_k$, where $\alpha_{k+\frac{1}{2}} = H_k/(H_k+H_{k+1})$.

These equations can be written in potential vorticity form as

$$\frac{DQ_k}{Dt} = F_k, \quad k = 1, N; \tag{5.8}$$

where

$$Q_k = \nabla^2\psi_k + \frac{2\omega}{H_k}(h_{k+\frac{1}{2}} - h_{k-\frac{1}{2}}); \tag{5.9}$$

and

$$F_k = \nu\nabla^4\psi_k \quad \text{for} \quad k = 1, N-1; \; F_N = \nu\nabla^4\psi_k - \epsilon_B\nabla^2\psi_N. \tag{5.10}$$

For consistency in relation (5.9), $h_{\frac{1}{2}} = 0$ and $h_{N+\frac{1}{2}} = H_B$. Potential vorticity is conserved following fluid particles, except for frictional effects.

Note that the layer streamfunction field can be written in terms of vertical modes. In fact, the numerical solutions are found by solving the equivalent modal equations (each mode is

simply a two-dimensional field) as discussed by Holland (1978). For the present case of uniform stratification and equal layer depths, the model shapes are simply related to the streamfunction by

$$\phi_{BT} = \tfrac{1}{3}(\psi_1+\psi_2+\psi_3),$$

$$\phi_{BC1} = a_1(\psi_1-\psi_3),$$

and

$$\phi_{BC2} = a_2(\psi_1-2\psi_2+\psi_3),$$

where $a_1 = 0.4082$ and $a_2 = -0.2357$. Here, ϕ_{BT} is the barotropic mode, and ϕ_{BC1} and ϕ_{BC2} are the first and second baroclinic modes. These baroclinic modes have radii of deformation (called Rd_1 and Rd_2) determined by the system parameters as shown in table 1 and, as will be demonstrated, play an important role in the flow response to the obstacle.

5.3. *Numerical experiments*

These equations are solved as an initial-value problem in which a uniformly stratified flow enters a channel of width 31.2 cm, length 62.4 cm and depth 8.1 cm. In the diagrams shown, the flow is from left to right past an isolated cosine-squared obstacle of height 2.06 cm and diameter 10.06 cm situated near the upstream end of the channel. The viscosity is 0.0108 $cm^2\ s^{-1}$. At time $t = 0$, the undisturbed flow ($u = U$ = constant, $v = 0$) begins to feel the influence of the obstacle, disturbances move downstream, and after several minutes the flow comes to a steady state, at least for the experiments run here.

A three-layer model ($H_k = 2.7$ cm, $k = 1$–3) with uniform vertical stratification is considered. A horizontal grid size of 0.312 cm is used so that there are 100 grid points across and 200 points along the channel. A time step of 0.2 s is found to be necessary so that a run of 6 min takes 1800 time steps. The boundary conditions are that $u = -\partial\psi/\partial y$ is constant at both upstream and downstream ends (ψ is a linear function of y), and that $Q = 0$ on the upstream (inflow) boundary and $Q_x = 0$ on the downstream (outflow) boundary. As explained earlier, this latter condition is a very simple extrapolation technique to let 'Q-stuff' be advected out of the region.

Figure 26 shows the spin-up phase (the first 2 min) in terms of the potential vorticity plume generated at the obstacle, and figures 27–29 show several fields after a steady state is reached (6 min); in these experiments the upstream flow speed U is 0.50 cm s^{-1}, the rotation rate ω is 0.5 s^{-1}, and the proportional density stratification, $\Delta\rho/\rho_0$, is 0.0032 (see table 1). This is considered the 'standard' case and U, ω and $\Delta\rho/\rho_0$ are varied to understand the dependence of the vertical and horizontal disturbances upon the non-dimensional numbers governing the flow. For this case, the Rossby number, $Ro = U/2\omega D = 0.05$; the Ekman number, $Ek = \nu/2\omega H^2 = 1.65\times10^{-4}$; and the Froude number $Fr = U/h(g\Delta\rho/H\rho_0)^{\frac{1}{2}} = 0.048$ (see table 1). Finally, figure 30*a*, plate 16, shows the streaklines measured in the laboratory for experiment 1 (table 1) at a depth z^* of 3 cm above the bottom; figure 30*b*, plate 16, shows the numerical model streamlines at this level (interpolated linearly from levels 2 and 3 in the model results).

Figure 27 shows, at three levels, the streamlines of the steady flow (left panels), the disturbance streamfunction obtained by subtracting the linear streamfunction representing the uniform upstream flow (middle panels) and the barotropic and two baroclinic modes that can be defined as a linear combination of the streamfunctions (right panels). Here the barotropic mode shows the disturbance only; the inflow has been subtracted. The modes are especially useful because the inflow is uniform in the vertical; i.e. it is barotropic, and the three modes

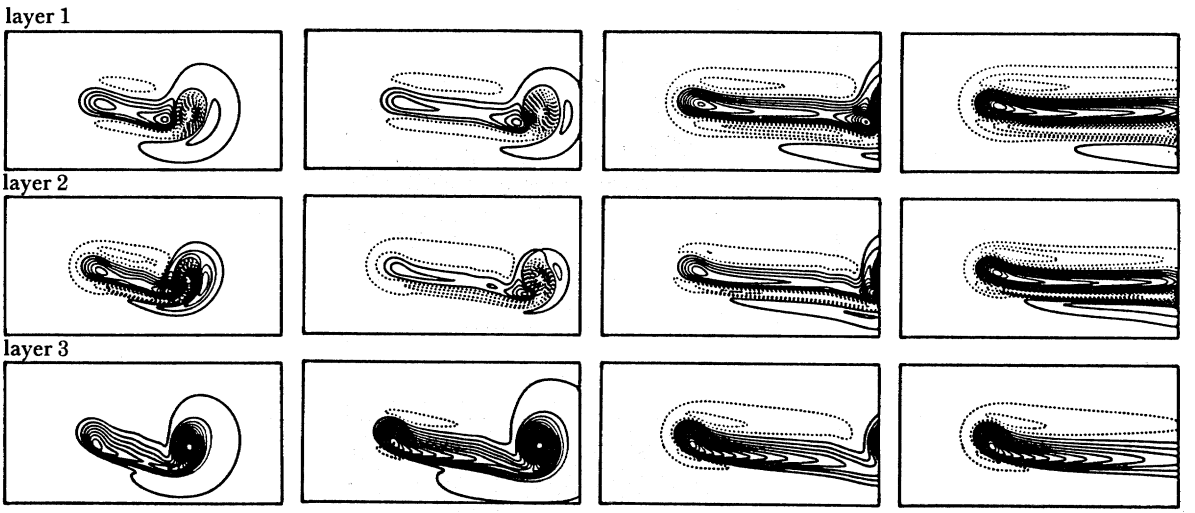

FIGURE 26. The potential vorticity fields, Q, at three levels (top to bottom) and at time intervals of 48, 72, 96 and 120 s, showing the spin-up phase of numerical experiment 1 (see table 1). After 2 min, the flow is near to steady state. The contour intervals vary from level to level and time to time.

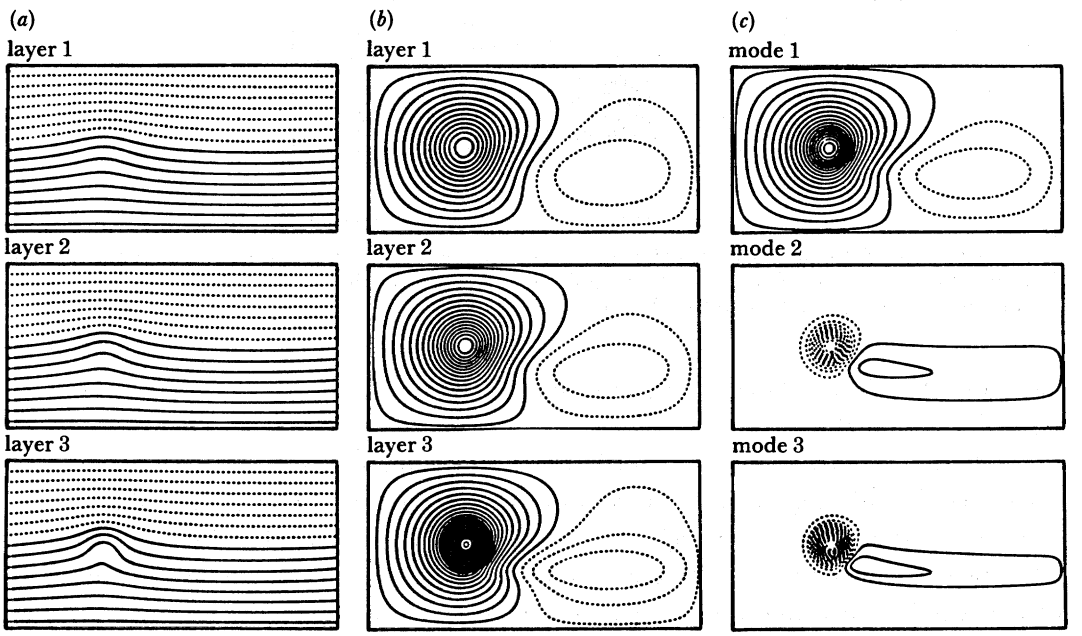

FIGURE 27. The steady-state fields (at $t = 360$ s) of (*a*) the streamfunction ψ, (*b*) the perturbation streamfunction, and (*c*) the perturbation vertical modes for numerical experiment 1 (see table 1). The top panel of the modes shows the barotropic disturbance and the middle and lower panels show the first and second baroclinic modes, respectively. The contour intervals from top to bottom are: left, 1.0, 1.0, 1.0 $\mathrm{cm^2\,s^{-1}}$; middle, 0.1, 0.1, 0.1 $\mathrm{cm^2\,s^{-1}}$; right, 0.1, 0.03, 0.008 $\mathrm{cm^2\,s^{-1}}$.

represent the disturbance caused by the obstacle. Note that the leftward disturbance in the streamlines, largest in the lowest layer and decreasing upward, is caused by a slightly asymmetrical disturbance centred over the obstacle (shown by both the ψ disturbance and modal disturbance fields). Downstream, the streamlines tend to return to their original location in the channel but they overshoot somewhat to give rise to a disturbance that reaches far

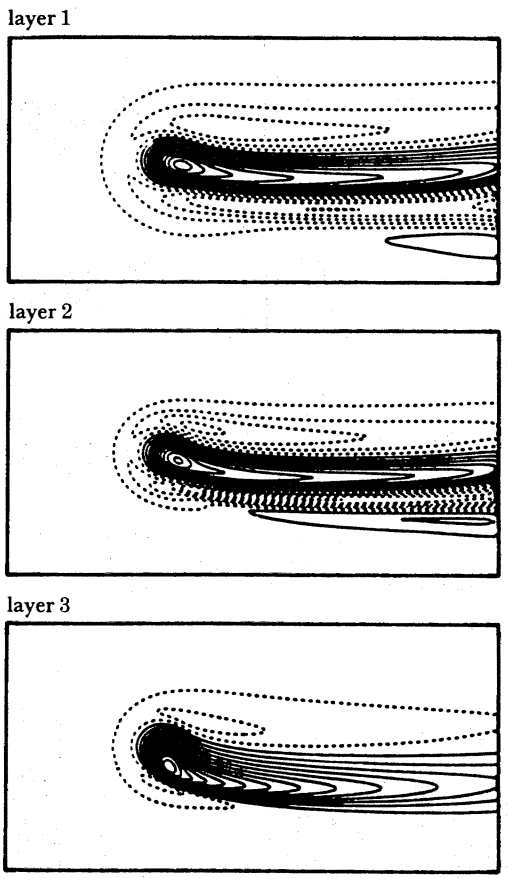

FIGURE 28. The steady state fields (at $t = 360$ s) of potential vorticity Q for numerical experiment 1 (see table 1). Note the plume-like nature of the spread of Q from its source over the obstacle. The contour intervals (top to bottom) are 0.001, 0.002 and 0.04 s^{-1}, respectively.

downstream. As will be shown later, the asymmetry and distant downstream influence are caused by frictional effects.

Figure 28 shows plots of potential vorticity, Q, in the three layers. Potential vorticity tends to be conserved following streamlines (5.8) but is generated in the vicinity of the obstacle by friction and carried downstream. Q_k is quite small, being the small difference between the relative vorticity $\nabla^2\psi_k$ and the stretching term $2\omega(h_{k+\frac{1}{2}}-h_{k-\frac{1}{2}})/H_k$; see (5.9). Note that the advection speed in this experiment dictates that the flow reaches a near steady state in only 2 min (figure 26) and is quite steady after 6 min.

Finally, the vertical velocities, $w_{k+\frac{1}{2}}$, and height perturbations, $h_{k+\frac{1}{2}}$, at the interfaces between the layers are shown in figure 29. Taking account of the contour intervals (see figure legends), the disturbance in w at the lower interface, 2.74 cm above the bottom, is about 35% of the bottom induced vertical velocity, whereas w at the upper interface (5.4 cm above the bottom) is only 10%. The disturbance h shows a similar confinement of the disturbance by the stratification to near the bottom. The first interface above the bottom is uplifted 0.85 cm and the second interface 0.37 cm over an obstacle 2.06 cm high. These results will be quantified, as a function of nondimensional numbers, below. The results are summarized in table 1.

These figures give a complete picture of the steady-state flow found with this choice of

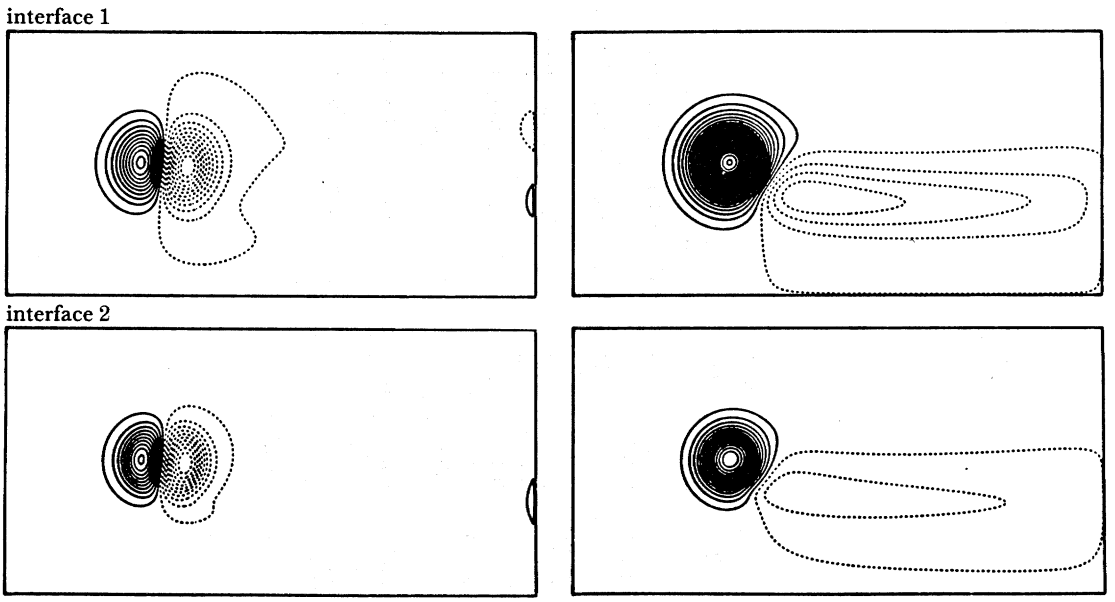

FIGURE 29. The steady-state fields (at $t = 360$ s) of vertical velocity (left) and height perturbation (right) at the two interfaces separating fluid layers for numerical experiment 1 (see table 1). The contour intervals are 0.003 cm s^{-1} (upper interface) and 0.01 cm s^{-1} (lower interface) for w, and 0.01 cm (upper interface) and 0.05 cm (lower interface) for h.

parameters U, $\Delta\rho/\rho_0$ and ω. We can compare these results with other numerical experiments that systematically vary these parameters. Table 1 gives quantitative results for seven distinct experiments. Experiments 2 and 3 change the stratification, experiments 4 and 5 vary the amplitude of the inflow velocity, and experiments 6 and 7 vary the rotation rate. These changes lead to the non-dimensional numbers and results shown in table 1 and in figures 31 and 32. Because a complete set of pictures of the flows is too large to show, table 1 summarizes the results in terms of how large the topographically induced disturbance is, as a function of depth, for different fields, and figures 31 and 32 show the four disturbance fields and height-perturbation fields, respectively, for experiments 2–7. These can be compared with the appropriate figures showing results for experiment 1.

Note that the contour intervals for a given field at a given level are the same in all experiments so they can be directly compared. In addition, as a measure of how large the disturbance is in these seven experiments, the maximum disturbances in ψ_k, ϕ_k, $h_{k+\frac{1}{2}}$ and $w_{k+\frac{1}{2}}$, as measured by the difference between the maximum and minimum values found in these fields, are shown in table 1.

Figure 31 shows the streamfunction deviation fields for the six auxiliary experiments. Note that experiments 2 and 7 show an especially strong asymmetry associated with the flow veering far to the right (looking downstream) after passing the obstacle. In the lowest layer, the negative disturbance, as shown by the number of contour lines, is greater in these cases than in experiment 1. Experiment 5 has about the same disturbance amplitude whereas 3, 4 and 6 all have less deviation of the downstream flow. At the uppermost level (layer 1), however, only experiment 7 is stronger than experiment 1. The strong response just above the obstacle in experiment 2 is damped rapidly with height by the stronger stratification.

The interface-height perturbation fields are shown in figure 32. Note the large amplitude of

TABLE 1

numerical experiment	physical parameters U cm s^{-1}	$\Delta\rho/\rho_0$	ω s^{-1}	$Rd1$ cm	$Rd2$ cm	non-dimensional numbers Ro	$10^{-4}\,Ek$	Fr	ψ_1 cm^2 s^{-1}	ψ_2 cm^2 s^{-1}	ψ_3 cm^2 s^{-1}	deviation amplitudes ϕ_1 cm^2 s^{-1}	ϕ_2 cm^2 s^{-1}	ϕ_3 cm^2 s^{-1}	$h_{1.5}$ cm	$h_{2.5}$ cm	$w_{1.5}$ cm s^{-1}	$w_{2.5}$ cm s^{-1}
1	0.50	0.0032	0.50	1.68	0.97	0.050	1.65	0.048	1.57	1.88	2.72	2.06	0.49	0.13	0.31	0.85	0.064	0.202
									(1.69)	(2.01)	(2.87)	(2.19)	(0.48)	(0.13)†				
2	0.50	0.0128	0.50	3.36	1.94	0.050	1.65	0.024	0.98	1.46	3.26	1.89	0.98	0.33	0.12	0.45	0.066	0.344
									(1.20)	(1.72)	(3.65)	(2.19)	(1.00)	(0.33)†				
3	0.50	0.0008	0.50	0.84	0.48	0.050	1.65	0.096	1.92	2.05	2.37	2.11	0.18	0.04	0.53	1.18	0.035	0.082
									(2.00)	(2.14)	(2.43)	(2.19)	(0.18)	(0.04)†				
4	1.00	0.0032	0.50	1.68	0.97	0.100	1.65	0.096	1.65	1.97	2.83	2.15	0.49	0.13	0.31	0.84	0.135	0.429
									(1.69)	(2.01)	(2.87)	(2.19)	(0.48)	(0.13)†				
5	0.25	0.0032	0.50	1.68	0.97	0.025	1.65	0.024	0.97	1.19	1.80	1.32	0.39	0.11	0.24	0.68	0.020	0.063
									(1.69)	(2.01)	(2.87)	(2.19)	(0.48)	(0.13)†				
6	0.50	0.0032	0.25	3.36	1.94	0.100	3.30	0.048	0.56	0.82	1.78	1.06	0.51	0.17	0.13	0.47	0.038	0.194
									(0.60)	(0.86)	(1.82)	(1.10)	(0.50)	(0.16)†				
7	0.50	0.0032	1.00	0.84	0.48	0.025	0.82	0.048	3.20	3.45	3.99	3.55	0.35	0.08	0.51	1.16	0.056	0.134
									(4.00)	(4.27)	(4.87)	(4.38)	(0.35)	(0.08)†				

† The numbers in parentheses show the results for the analogous frictionless cases in which $Q = 0$.

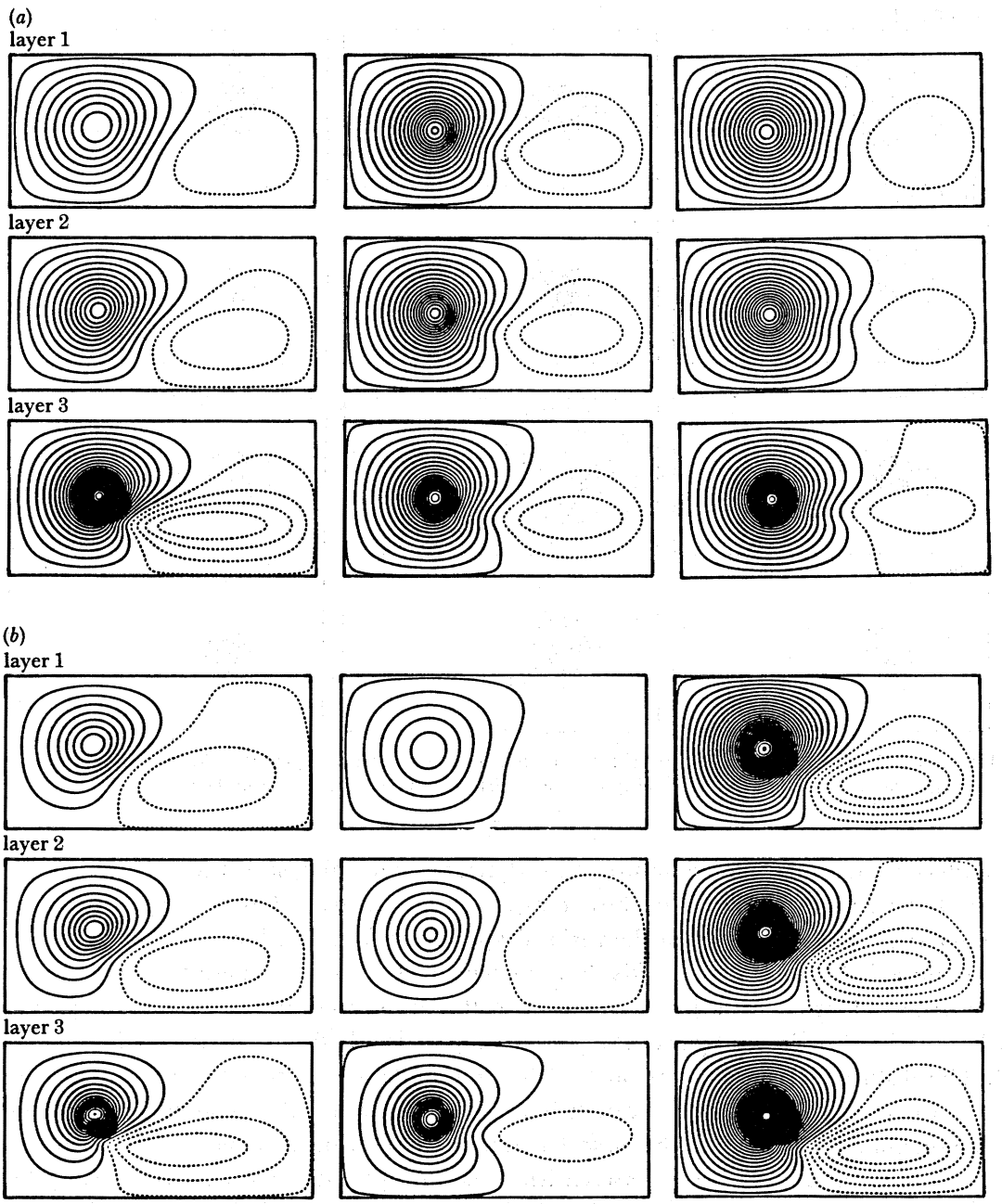

FIGURE 31. The streamfunction perturbation fields for numerical experiments 2–7. Experiments 2–4 are shown (left to right) in (*a*); experiments 5–7 are shown (left to right) in (*b*). The contour interval (the same for all experiments) is 0.1 $cm^2 s^{-1}$ in all diagrams.

response in experiments 3 and 7 and the broad region of uplift in experiments 2 and 6. This baroclinic response is related to the respective baroclinic radii of deformation governing the flow in the several experiments (table 1). Large deformation radii lead to a broad but weak response whereas small *Rd* values lead to a local intense response.

Careful perusal of these results shows very briefly something of the nature of the QG stratified topographic response in these experiments. In fact, the numerical model can be quite useful

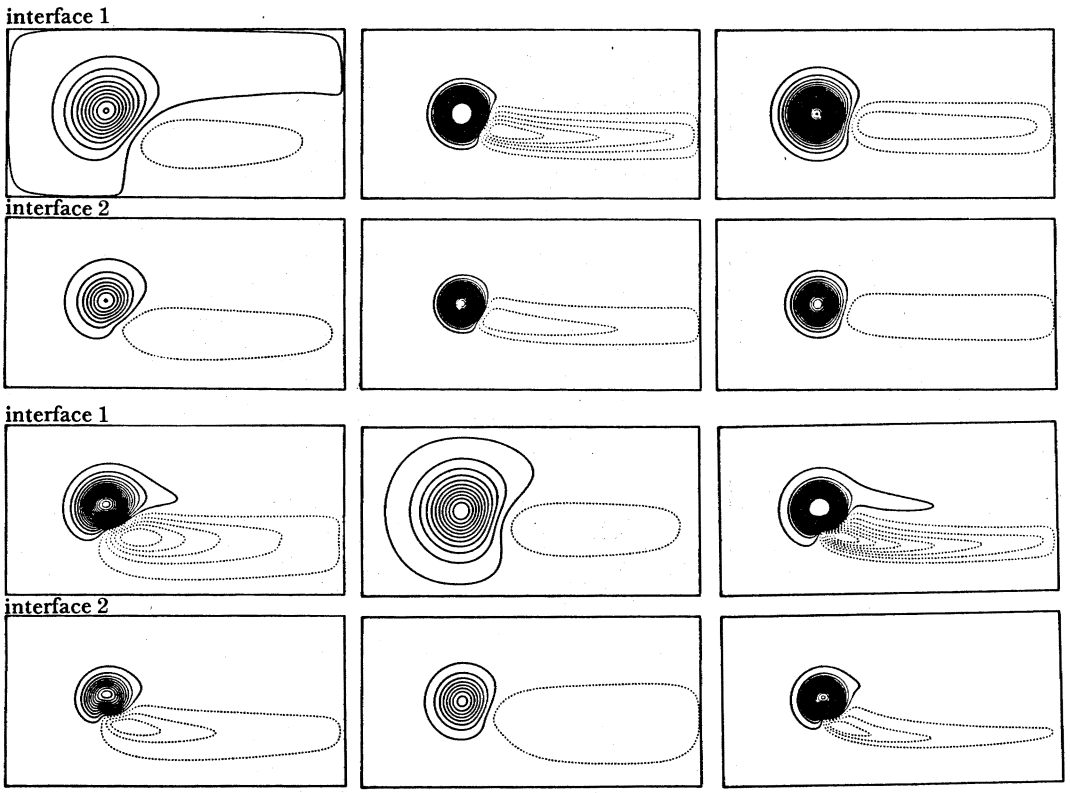

FIGURE 32. The height perturbation fields for numerical experiments 2–7 (left to right, top to bottom). The contour intervals (the same in all experiments) are 0.01 cm (upper interface) and 0.05 cm (lower interface).

in understanding the detailed nature of the dynamics governing stratified rotating laboratory flows. For example, it is easy to show that an important part (but not all) of the response characteristics indicated here for the various experiments is dictated by the respective solutions for a simplified, frictionless, steady flow in which Q is exactly conserved (and thus zero everywhere). This is shown by examining $Q \equiv 0$ solutions; figure 33 shows the fields for one such case with experiment 1 parameters, to be compared with the full frictional solution in figure 27. The disturbance is symmetrical but the amplitude and horizontal–vertical structure is similar to the actual experiment 1 results (see also table 1, where the streamfunction and modal deviation amplitudes for both the basic experiments and for the analogous $Q \equiv 0$ solutions are given). The biggest differences between frictional and potential vorticity conserving flows is found in experiment 5 where the slow basic flow allows time for friction to act, thus reducing the deviation amplitudes. In this case, the disturbance amplitudes are only about 60 % of the frictionless ones, whereas all the other cases are greater than 85 % of their respective frictionless amplitudes.

We shall not delve deeper into the physics of these flows here. It is clear that at least part of the behaviour observed in the laboratory, the large-scale steering of the flow by an obstacle, is captured and rendered understandable by these numerical exercises. It is also clear that another part of the flow behaviour, the eddy-shedding aspect, is not found in these QG numerical simulations. It is our speculation that this eddying behaviour, found to occur for the most part

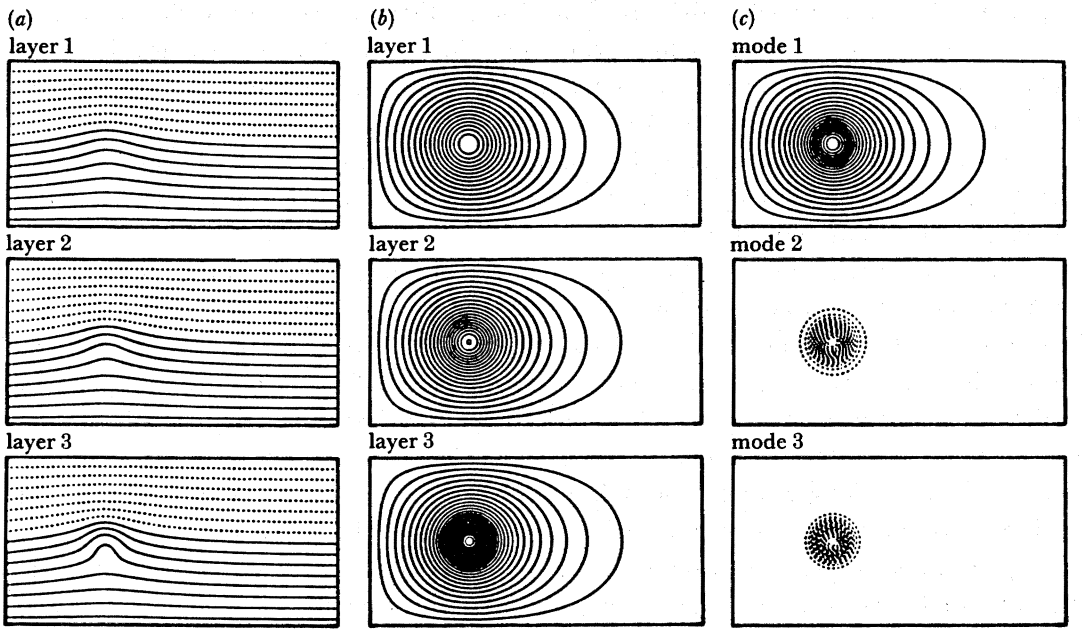

FIGURE 33. The fields of (*a*) the streamfunction ψ, (*b*) the perturbation streamfunction, and (*c*) the perturbation vertical modes for the frictionless case in which $Q = 0$ everywhere in the flow; numerical experiment 1 parameters are used (see table 1). Compare with figure 27 and see table 1 for amplitudes. The contour intervals are the same as in figure 27.

at levels in the fluid below the top of the obstacle, is a vortex-shedding phenomenon associated with frictional boundary layers on the sides of the obstacle, a phenomenon not included in the QG physics. A full, primitive-equation numerical model would be needed to explore this problem.

6. CONCLUDING REMARKS

The present experiments have described both the transient development and steady-state nature of the velocity fields resulting from the slow steady motion of tall, conical and smooth shallow cosine-squared solid obstacles respectively through rotating stratified fluids. For rotating and stratified fluids the motion above the level of the shallow cosine squared topography is characterized by (i) horizontal deflections of incident streamlines and (ii) lee-wave generation downstream. For a given obstacle and fluid geometry, the vertical distance over which the obstacle exerts a steering effect upon the flow depends upon the values of *Ro*, *Ek* and *S*. The degree of streamline distortion (steering) decreases with increasing z^*/h_0 and

(i) reduces with increasing *Ro* for constant *S*, *Ek*;

(ii) reduces with increasing *S* for constant *Ro*, *Ek*.

The principal distinguishing feature of the lee-wave character is the cross-channel asymmetry, with the largest amplitude waves being produced at the right side of the obstacle. The left–right asymmetry in wave amplitude increases with decreasing *S* and *Ro* as more fluid is deflected above the obstacle by the strong Coriolis force. As *S* increases, for constant *Ro* and *Ek*, more fluid flows around rather than over the obstacle, and lee waves cease to be generated. The

downstream flow at levels below the top of the obstacle then takes the form of a Karman vortex street, with an increased tendency for vortices to be shed from the obstacle as S increases.

When eddies are shed downstream, for both the cosine-squared and conical obstacles the lateral extent of the vortex-street wake

(i) increases with increasing $\Delta\rho/\rho_0$ for constant U, for non-rotating and rotating cases, and

(ii) increases with increasing ω for constant U, for weak and strong $\Delta\rho/\rho_0$ provided that the value of Fr is less than about 0.4.

The structure of the eddy field in the wake of the obstacle is determined essentially by the presence or absence of either or both of the two agencies (rotation and stratification) capable of inhibiting vertical motion. The results show that the field is established in three distinct phases. Following the impulsive start of the obstacle's motion from rest, the initial phase of flow development consists of the rapid generation of a symmetrical starting eddy pair in the lee of the obstacle. The eddy pair remains attached to the obstacle and moves with it. As time proceeds, the pair elongates longitudinally until shedding occurs at the rear of the obstacle. The dimensional retention time, τ_r, of the eddy pair by the obstacle is significantly shorter for rotating cases and appears to scale with the rotation period of the system (i.e. $\tau_r\omega/2\pi \approx 1$. When the fluid is not rotating, the retention time is much longer and seems to scale with the advective time; i.e. $\tau = Ut/D \approx 10$.

In the second phase of development (the shedding phase), the mode of shedding depends critically upon whether either rotation and/or density stratification are present. In the absence of both agencies, the eddies are shed in phase with each other from the right and left rear of the obstacle respectively. However, if either ω or $\Delta\rho/\rho_0$ are non-zero, eddies of opposite circulation are shed alternately from the obstacle. Because of potential-vorticity conservation, the initial downstream disturbance is cyclonic followed by the shedding of an anticyclonic vortex and then alternate shedding. For the experiments conducted, there is no evidence of the subsequent dominance of either cyclonic or anticyclonic vortices in the downstream wake.

The final stage of development consists of spindown of the individual eddies that have been shed by the obstacle. The spindown process is most effectively accomplished when the system is rotating, and for low S and shallow smooth topography, some of the eddies are spun down rapidly to leave only a sinuous tail disturbance downstream.

Quasigeostrophic-model results explain some of this behaviour but not all. The roles of stratification and friction in modifying the steady disturbance fields are examined briefly in a narrow range of parameter space. It is clear that more complete physics than QG will be necessary to examine the eddy-shedding process in detail.

The authors acknowledge the financial support of the National Science Foundation's Atmospheric Science Division (through the award of grant ATM 8218488), the Royal Society, NATO Scientific Affairs Division (RG 0005) and The Carnegie Trust for the Universities of Scotland for making the above investigation possible. The participation of W.R.H. was supported by the National Center for Atmospheric Research, which is also funded by the National Science Foundation. Thanks are also extended to Mr Greg Frary and to Mr Gordon Spence for their assistance with the laboratory programme.

References

Baines, P. G. & Davies, P. A. 1980 Laboratory studies of topographic effects in rotating and/or stratified fluids. In *Orographic effects in planetary flows* (ed. R. Hide & P. W. White), GARP Publications series no. 23, pp. 233–299. Geneva: World Meteorological Organization.

Boyer, D. L. 1968 Flow past a right circular cylinder in a rotating frame. *J. bas. Engng* **92**, 430–436.

Boyer, D. L. & Davies, P. A. 1982 Flow past a circular cylinder on a β-plane. *Phil. Trans. R. Soc. Lond.* A **306**, 533–556.

Boyer, D. L. & Kmetz, M. L. 1983 Vortex shedding in rotating flows. *Geophys. astrophys. Fluid Dyn.* **26**, 51–84.

Boyer, D. L., Davies, P. A. & Holland, W. R. 1984 Rotating flow past disks and cylindrical depressions. *J. Fluid Mech.* **141**, 67–95.

Boyer, D. L., Kmetz, M. L., Smathers, L., Chabert d'Hieres, G. & Didelle, H. 1984 Rotating open channel flow past right circular cylinders. *Geophys. astrophys. Fluid Dyn.* **30**, 271–304.

Boyer, D. L. & Biolley, F. 1986 Linearly stratified, rotating flow over long ridges in a channel. *Phil. Trans. R. Soc. Lond.* A **318**, 411–440.

Brighton, P. W. 1978 Strongly stratified flow past three-dimensional obstacles. *Q. Jl R. met. Soc.* **104**, 289–307.

Buzzi, A. & Tibaldi, S. 1977 Inertial and frictional effects on rotating and stratified flow over topography. *Q. Jl R. met. Soc.* **103**, 135–150.

Castro, I. P., Snyder, W. H. & Marsh, G. L. 1983 Stratified flow over three-dimensional ridges. *J. Fluid Mech.* **135**, 261–282.

Chow, J. C. & Holland, W. R. 1986 A multi-layer quasigeostrophic numerical model of ocean circulation. NCAR technical note. (In preparation.)

Davies, P. A. 1972 Experiments on Taylor columns in rotating stratified fluids. *J. Fluid Mech.* **54**, 691–717.

Davies, P. A. & Boyer, D. L. 1984 Quasi-geostrophic flow past isolated obstacles. *Riv. Met. aeronaut.* **44**, 265–275.

GARP 1978 Report of the First Planning Meeting on the GARP Mountain Sub-Programme. Geneva: World Meteorological Organization.

GARP-Alpex 1982*a* Alpex: field phase report, GARP publication no. 6A. Geneva: World Meteorological Organization.

GARP-Alpex 1982*b* Alpex: preliminary scientific results, GARP Publication no. 7. Geneva: World Meteorological Organization.

Gaster, M. 1969 Vortex shedding from slender cones at low Reynolds numbers. *J. Fluid Mech.* **38**, 565–576.

Hart, J. E. 1971 Instability and secondary motion in a rotating channel flow. *J. Fluid Mech.* **45**, 341–352.

Holland, W. R. 1978 The role of mesoscale eddies in the general circulation of the ocean. Numerical experiments using a wind-driven quasigeostrophic model. *J. phys. Oceanogr.* **8**, 363–392.

Honji, H., Taneda, S. & Tatsuno, A. 1980 Some practical details of the electrolytic precipitation method of flow visualization. *Res. Inst. appl. Mech., Kyushu Univ.* **28**, 83–89.

Hunt, J. C. R. & Snyder, W. H. 1980 Experiments on stably and neutrally stratified flow over a model three-dimensional hill. *J. Fluid Mech.* **96**, 671–704.

Huppert, H. E. & Bryan, K. 1976 Topographically generated eddies. *Deep Sea Res.* **23**, 655–679.

Kmetz, M. L. 1982 Vortex shedding in rotating flows. M.Sc. thesis, University of Wyoming, U.S.A.

Lezius, D. K. & Johnston, J. P. 1976 Roll cell instabilities in rotating laminar and turbulent channel flows. *J. Fluid Mech.* **77**, 153–175.

Merkine, L. O. & Solan, A. 1979 The separation of flow past a cylinder in a rotating system. *J. Fluid Mech.* **92**, 381–392.

Oster, G. 1965 Density Gradients. *Scient. Am.* **213**, 70–76.

Pedlosky, J. 1979 *Geophysical fluid dynamics.* (624 pages.) New York: Springer-Verlag.

Smith, R. B. 1980 Linear theory of stratified hydrostatic flow past an isolated mountain. *Tellus* **32**, 348–364.

Snyder, W. H., Britter, R. & Hunt, J. C. R. 1979 A fluid modelling study of the flow structure and plume impingement on a three-dimensional hill in stably stratified flow. In *Proc. 5th Int. Conf. on Wind Engng, Fort Collins* (ed. J. E. Cermak). Oxford: Pergamon Press.

Snyder, W. H., Thompson, R. S., Eskridge, R. E., Lawson, R. E., Castro, I. P., Lee, J. T., Hunt, J. C. P. & Ogawa, Y. 1985 The structure of strongly stratified flow over hills; dividing-streamline concept. *J. Fluid Mech.* **152**, 249–288.

Speziale, C. F. & Thangam, S. 1983 Numerical study of secondary flows and roll-cell instabilities in rotating channel flow. *J. Fluid Mech.* **130**, 377–395.

Tritton, D. J. 1977 *Physical fluid dynamics.* Wokingham: Van Nostrand Reinhold.

Vaziri, A. & Boyer, D. L. 1971 Rotating flow over shallow topographies. *J. Fluid Mech.* **50**, 79–95.

(i) (ii)

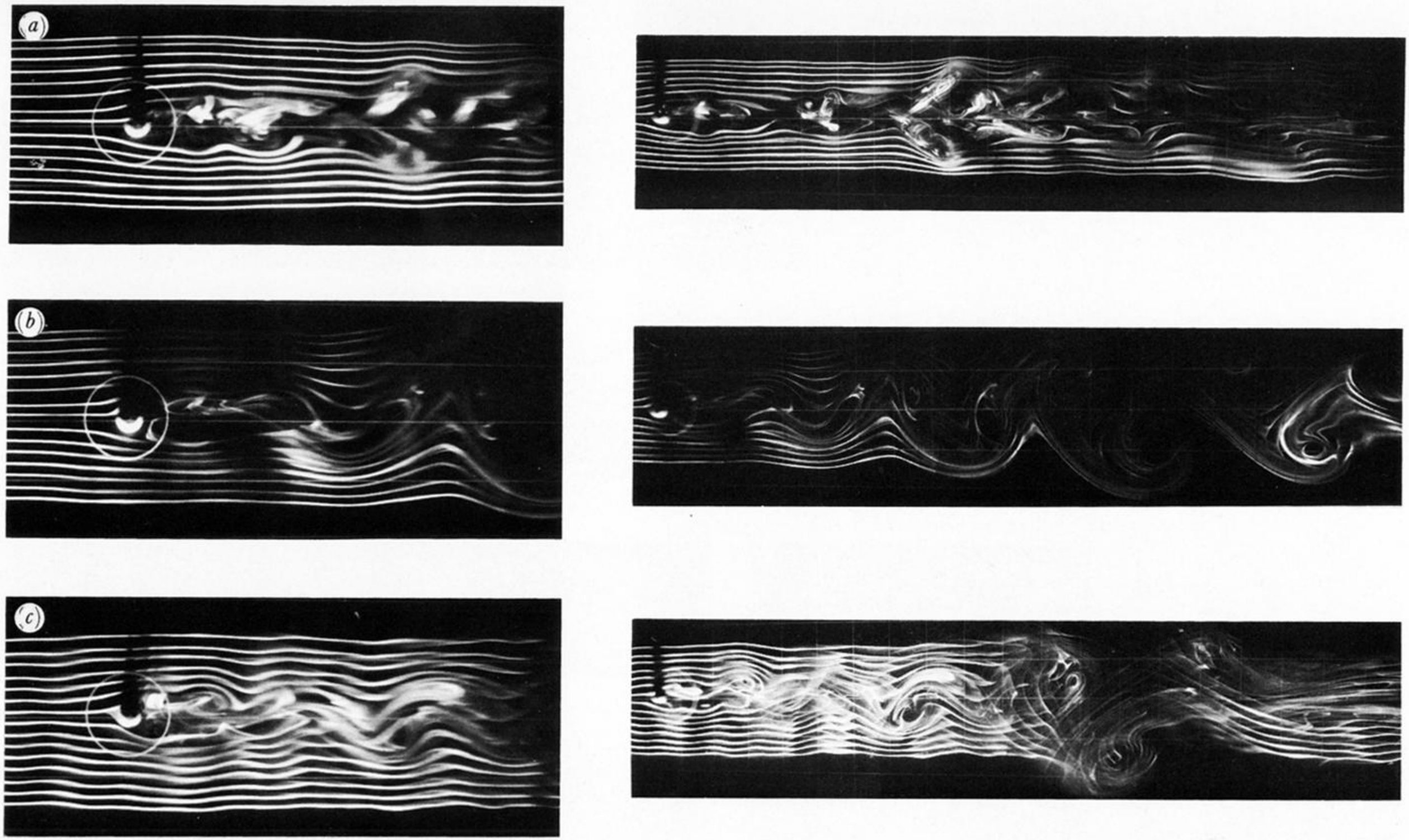

FIGURE 4. (i) Near-field and (ii) far-field streakline patterns for non-rotating flow past conical obstacles with $Re = 720$ and Fr values of (*a*) ∞, (*b*) 0.17 and (*c*) 0.06; $h_0/H = 0.81$, $h_0/D = 0.87$, $D/L = 0.24$ and $z^*/h_0 = 0.76$.

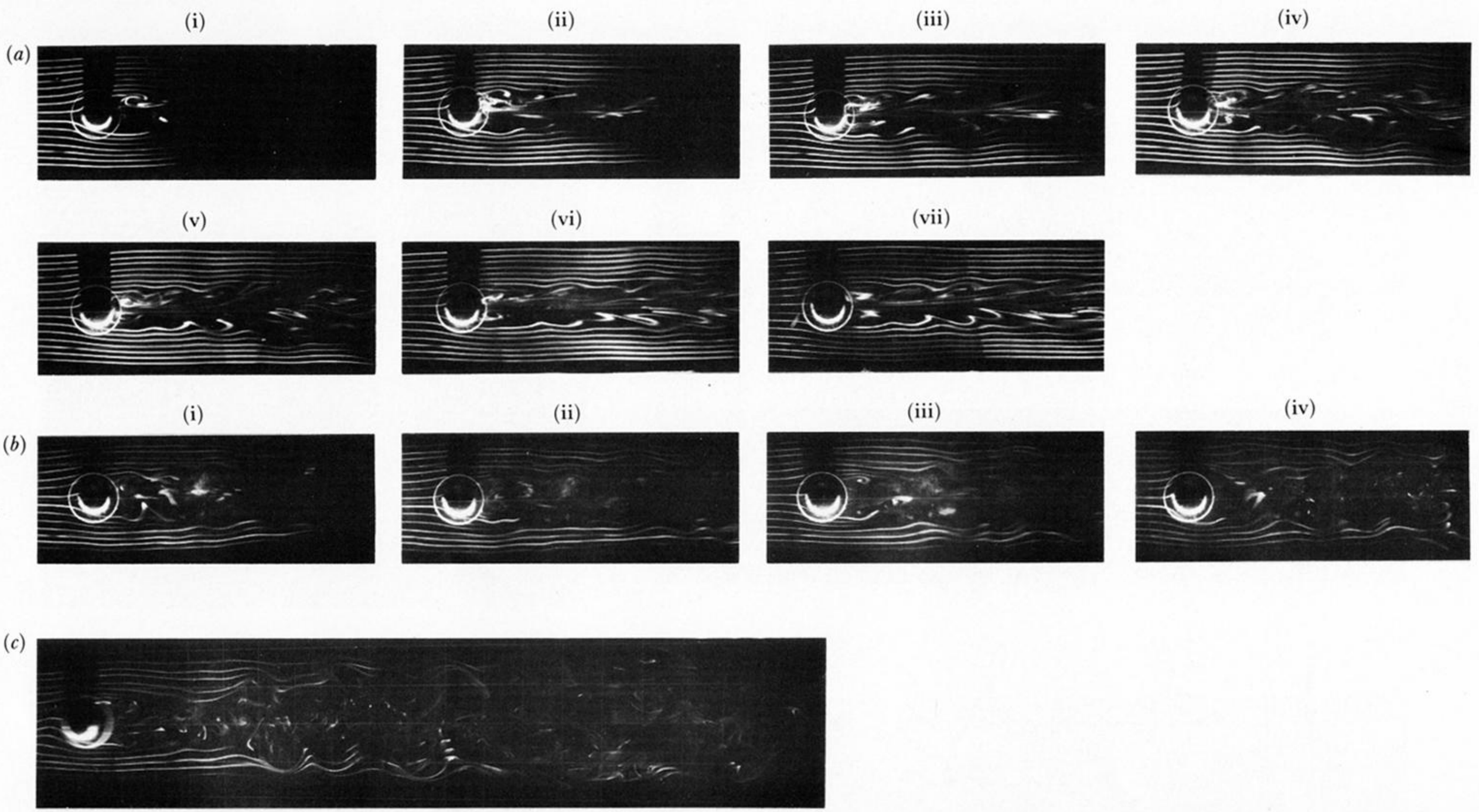

FIGURE 5. (*a*), (*b*) Near-field and (*c*) far-field streakline patterns for homogeneous non-rotating flow past conical obstacles with *Re* values of (*a*) 740 and (*b*), (*c*) 1110; geometrical parameters as in legend of figure 4 and $z^*/h_0 = 0.46$. Note that (*a*) and (*b*) represent time sequences.

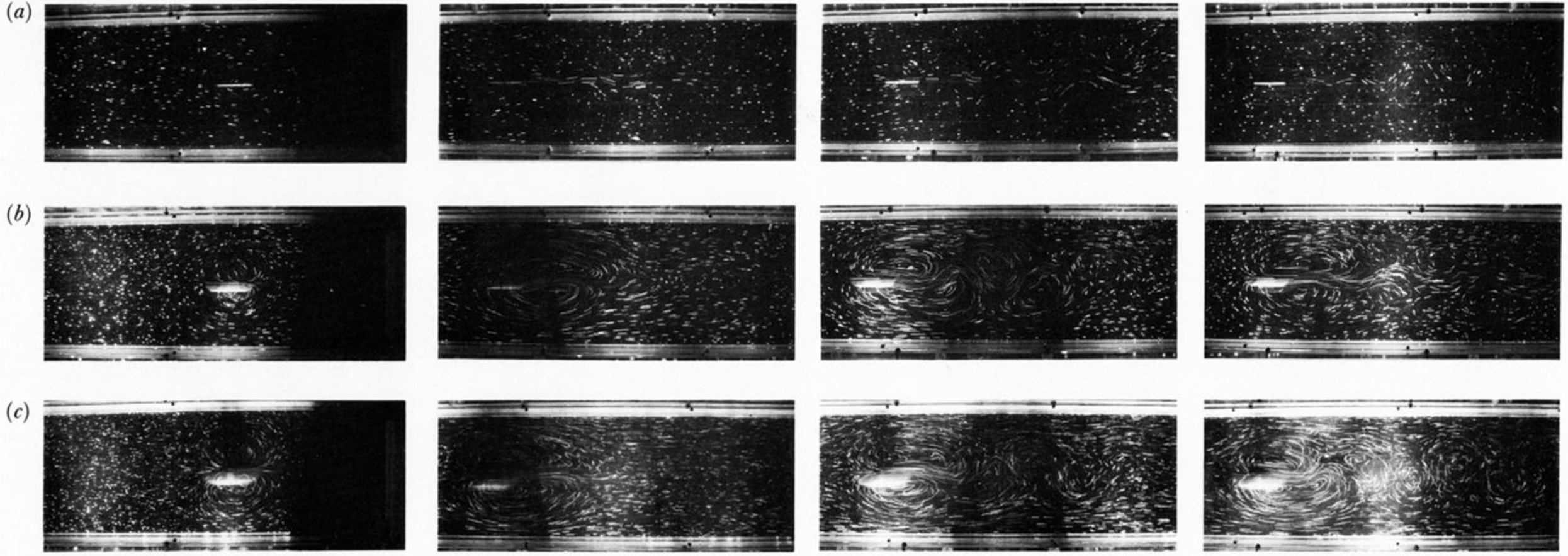

FIGURE 6. Time sequences of particle-streak photographs for non-rotating flow past conical obstacle with $Re = 390$, $Fr = 0.08$ and z^*/h_0 values of (*a*) 0.88, (*b*) 0.46 and (*c*) 0.15; geometrical parameters as in legend of figure 4. The dimensionless exposure time, $\tau_e = (\Delta t)U/D$ is 0.99, while the elapsed dimensionless time, $\tau = tU/D$, is noted on the figure (see text).

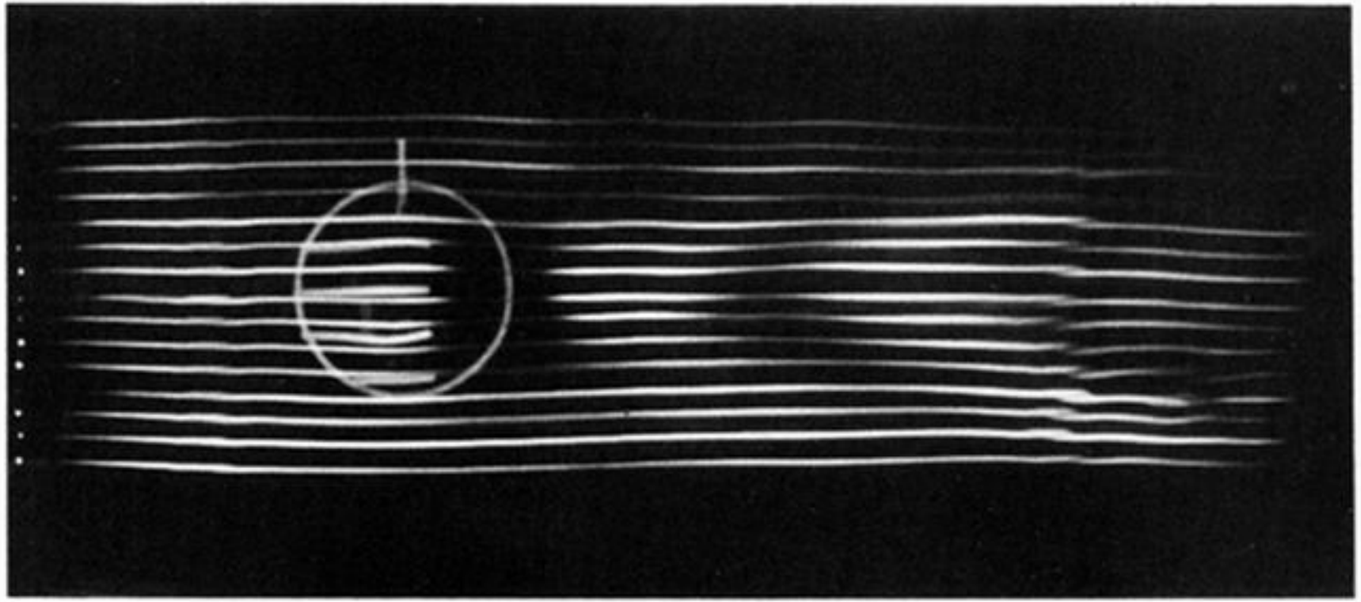

FIGURE 8. Streakline photograph depicting the existence of lee waves for non-rotating flow past a cosine-squared obstacle for $Re = 1500$, $Fr = 0.69$, $h_0/H = 0.25$, $h_0/D = 0.20$, $D/L = 0.32$ and $z^*/h_0 = 1.46$. Note that the white lines painted on the upstream portion of the obstacle are not streaklines.

(i) (ii)

(a)

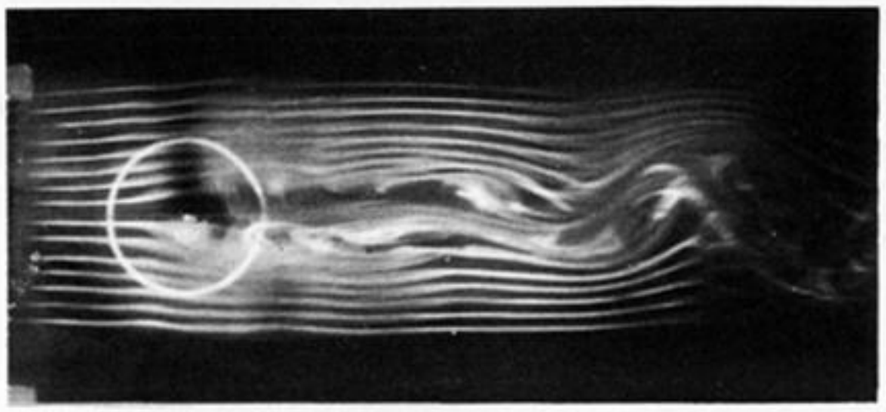

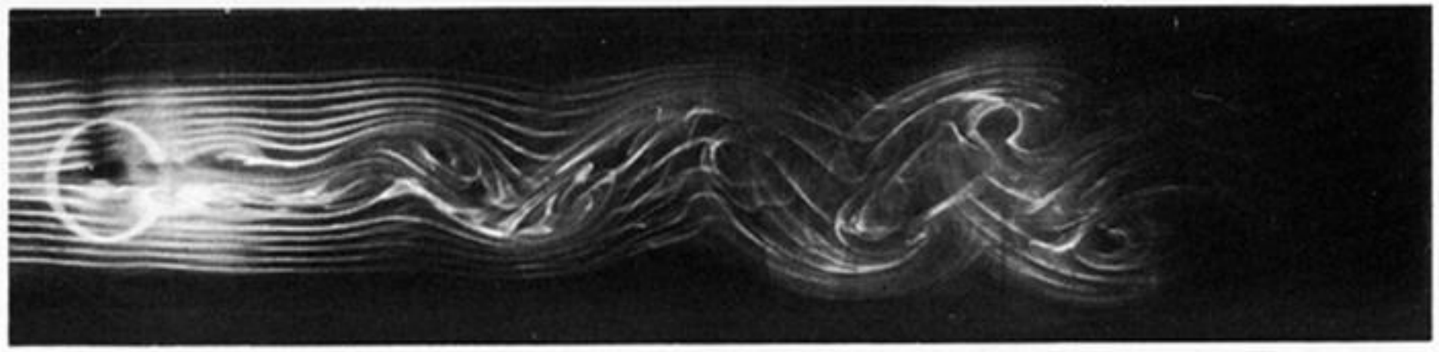

(b)

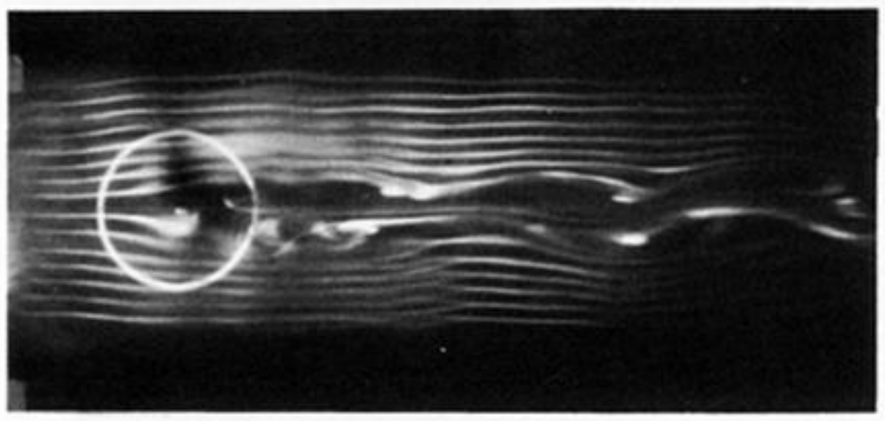

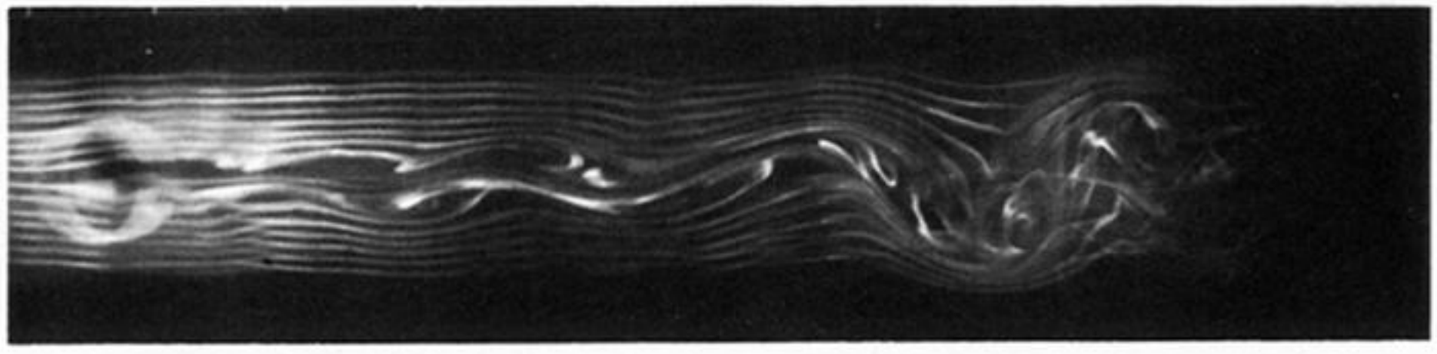

(c)

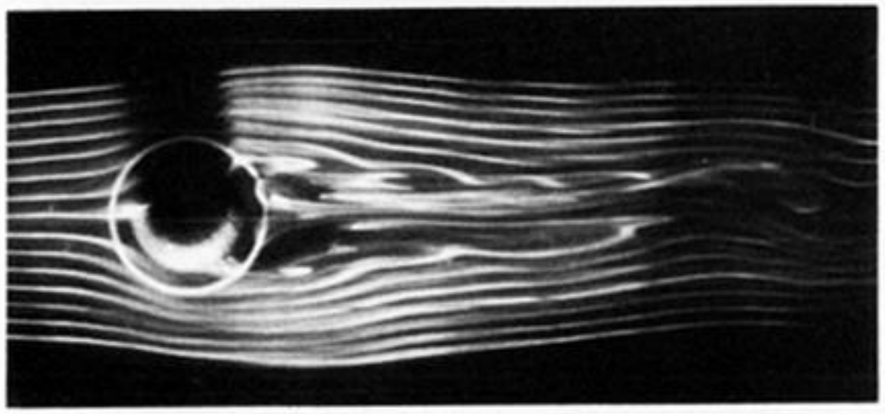

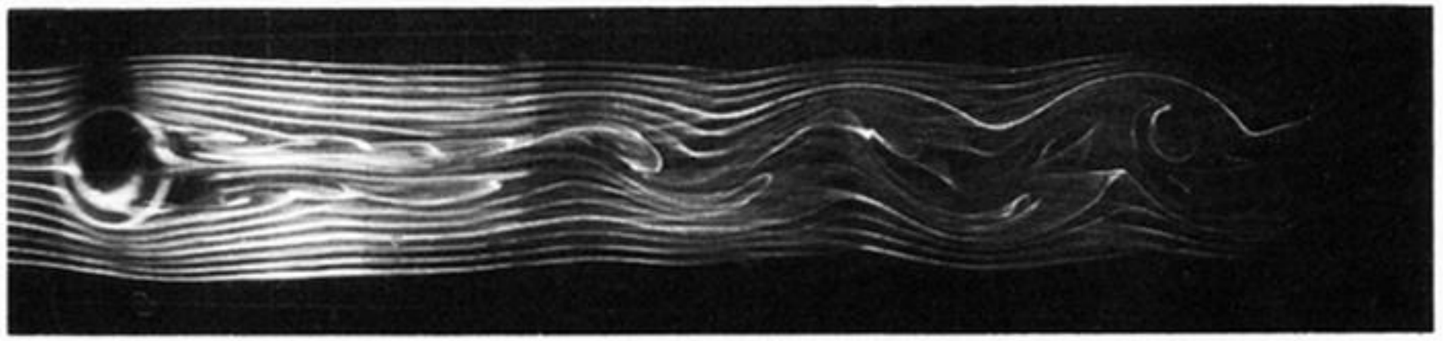

(d)

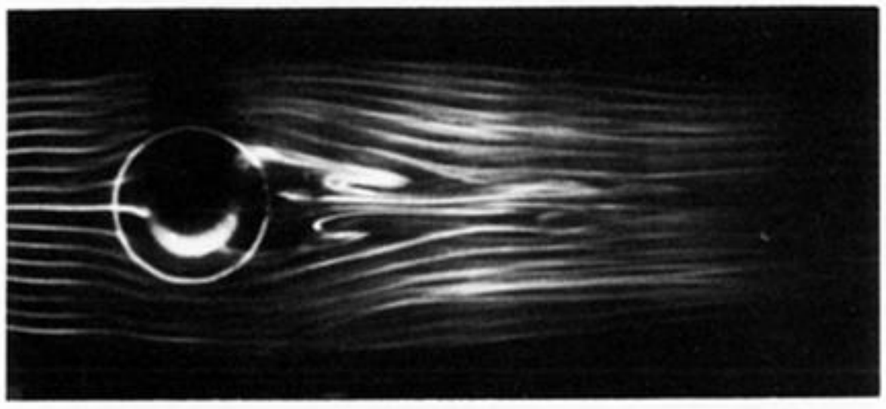

FIGURE 9. (i) Near-field and (ii) far-field streakline patterns for non-rotating flow past cosine-squared obstacle with z^*/h_0 values of (*a*), (*b*) 0.97 and (*c*), (*d*) 0.49, for *Re*, *Fr* values of (*a*) 1000, 0.19, (*b*) 1470, 0.29, (*c*) 1000, 0.18 and (*d*) 1470, 0.27. Geometrical parameters as in the legend of figure 8.

(i) (ii)

(a)

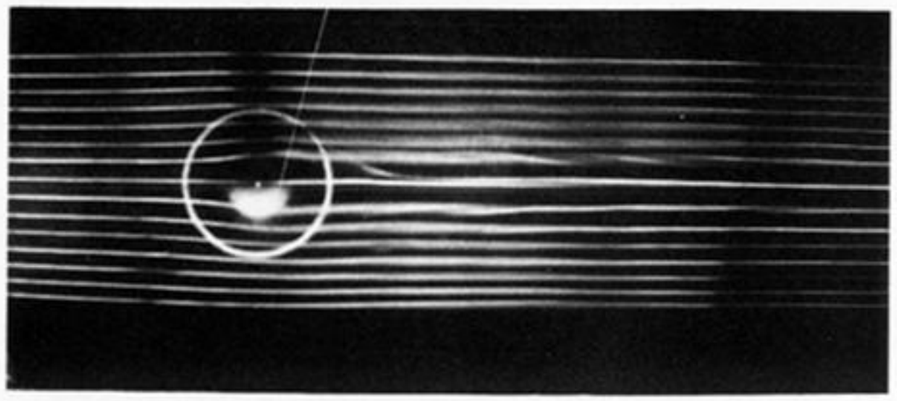

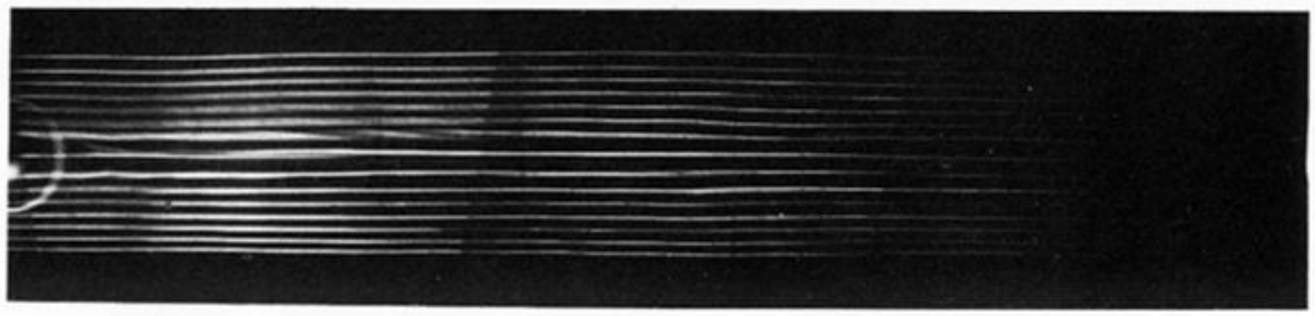

(b)

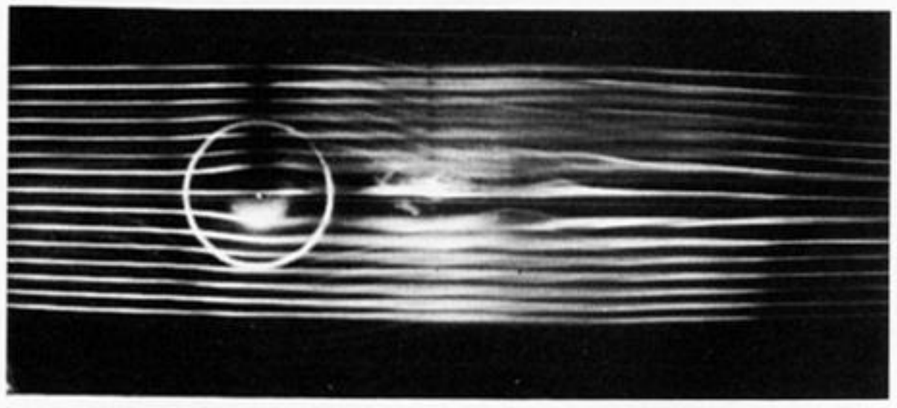

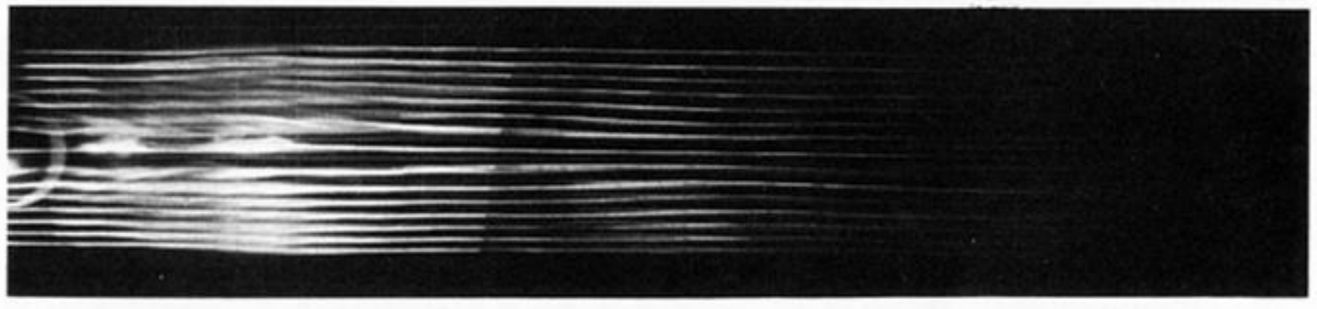

(c)

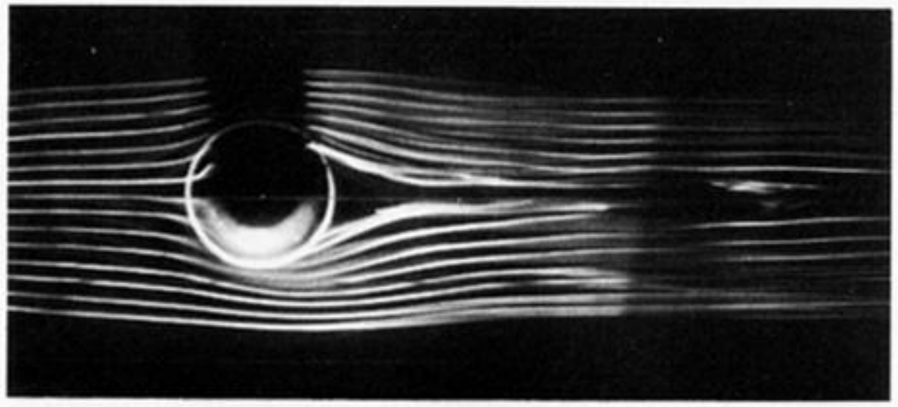

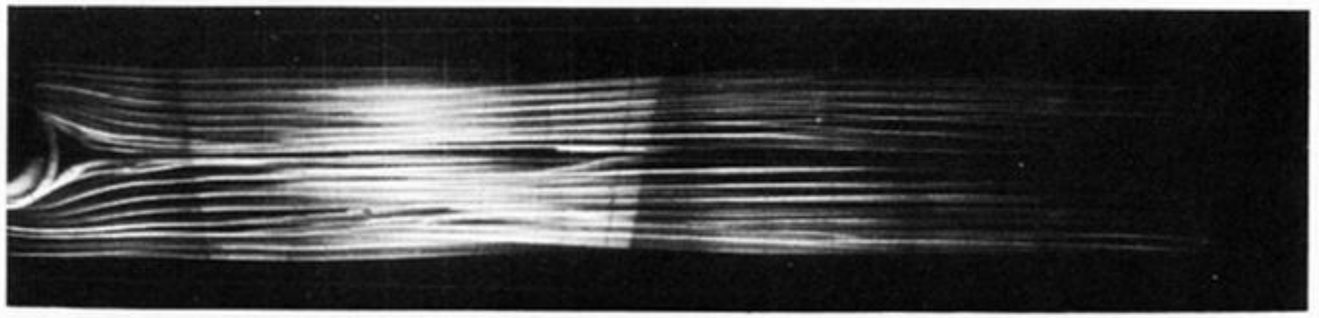

(d)

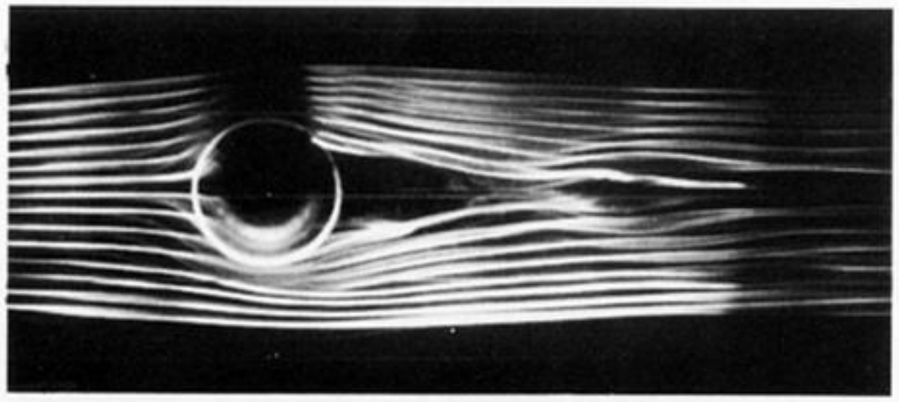

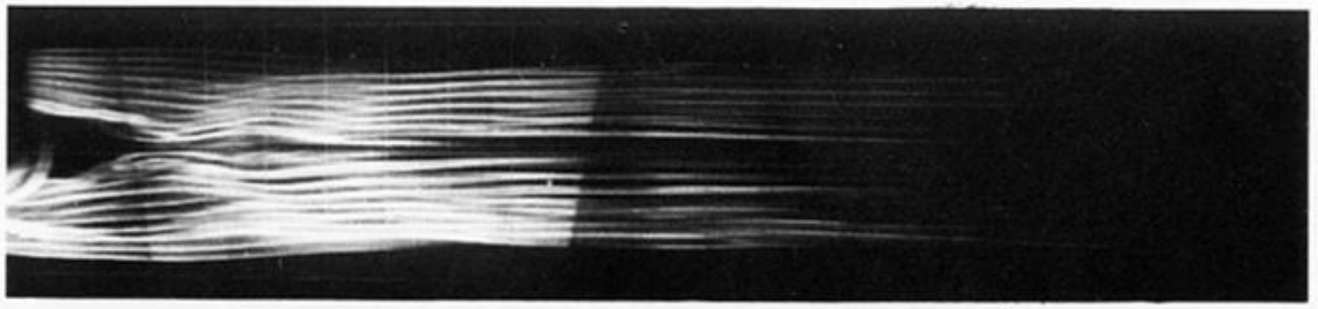

FIGURE 10. Legend as for figure 9 except for *Re*, *Fr* values of (*a*) 960, 0.55, (*b*) 1420, 0.75, (*c*) 960, 0.55 and (*d*) 1440, 0.76.

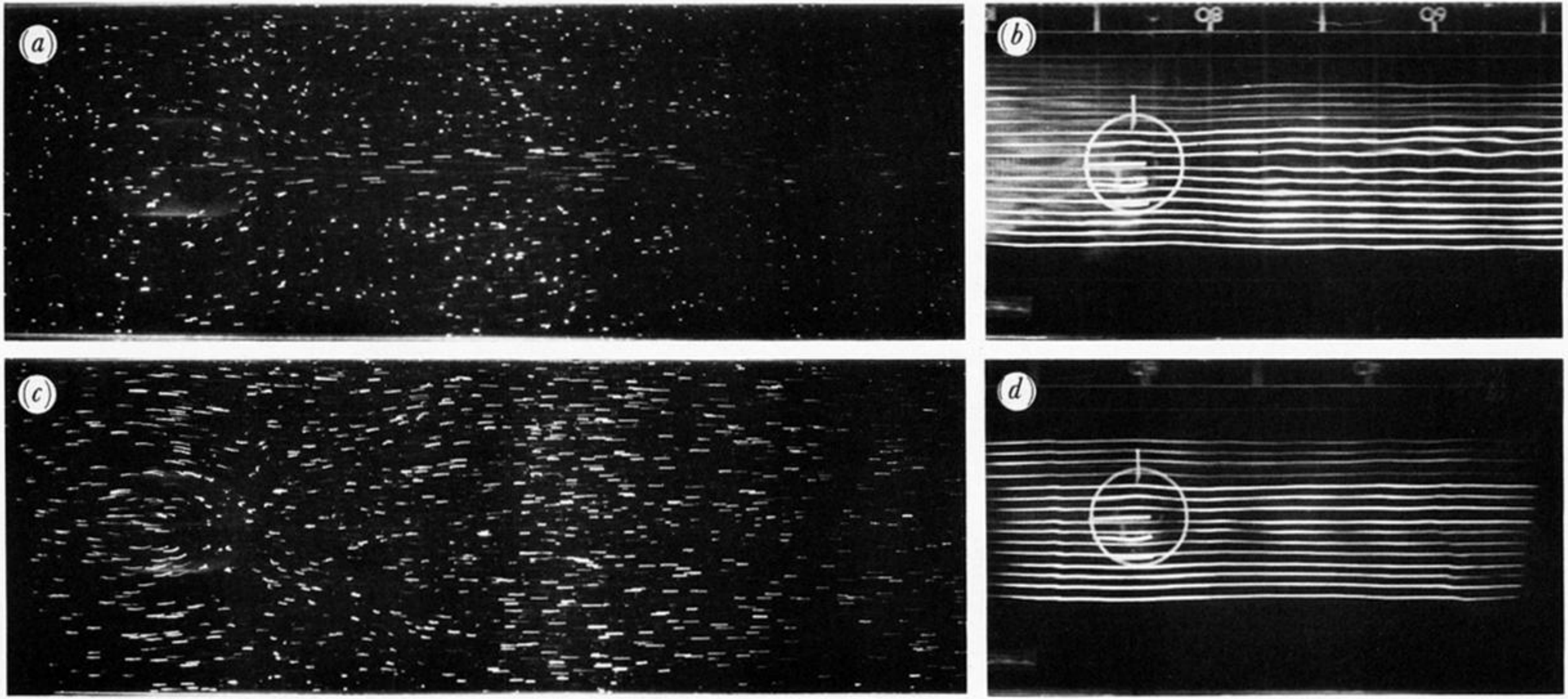

FIGURE 11. Some comparisons between streakline and particle streak photographs of non-rotating flow past cosine-squared obstacle for *Re*, *Fr* values of (*a*) 520, 0.25, (*b*) 490, 0.31, (*c*) 1030, 0.51 and (*d*) 1000, 0.59 and for $z^*/h_0 = 1.46$. Geometrical parameters as in the legend of figure 8.

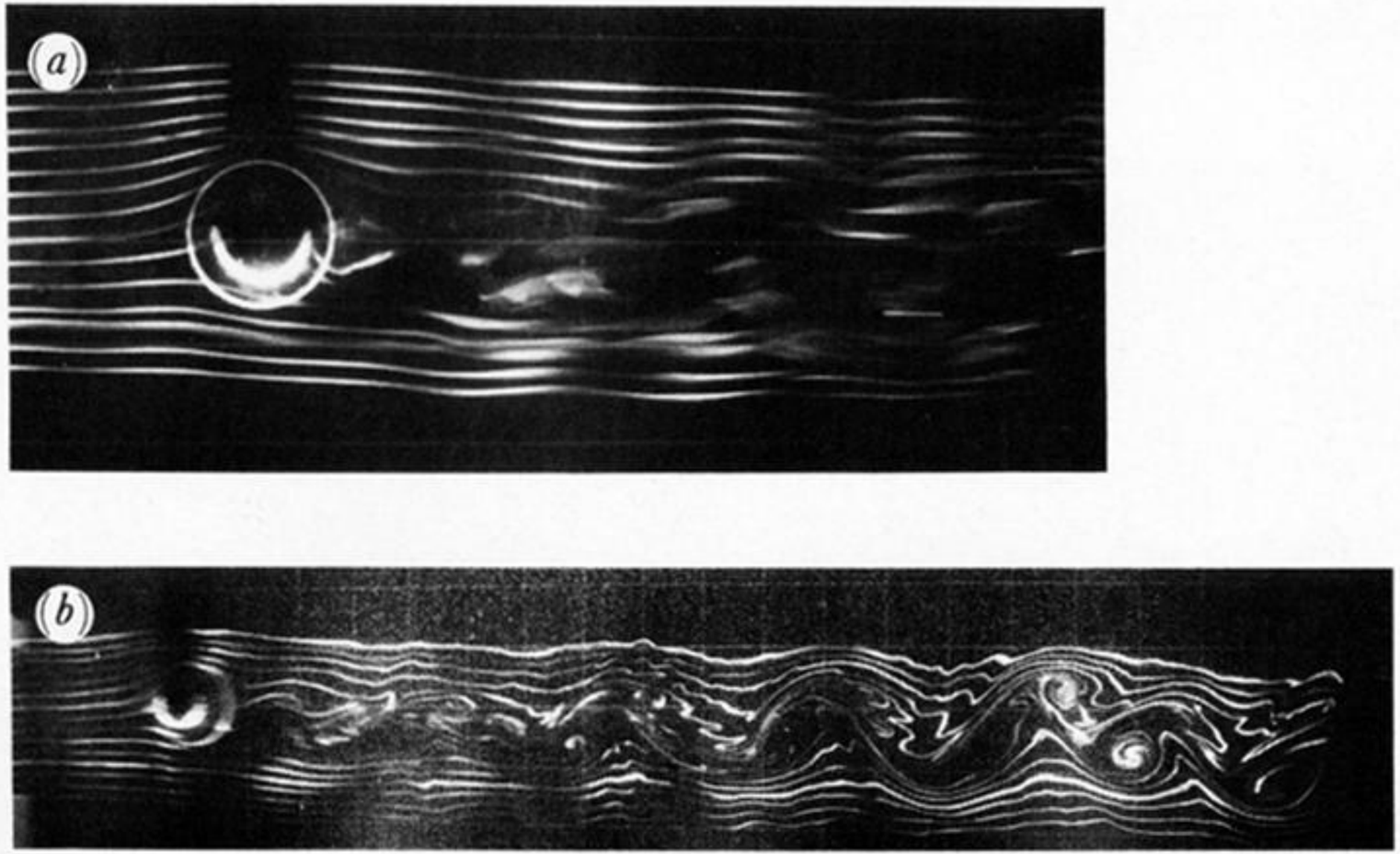

FIGURE 12. (*a*) Near-field and (*b*) far-field streakline patterns for rotating homogeneous flow past conical obstacle; $Ro = 0.20$, $Ek = 1.6 \times 10^{-4}$, $Re = 1100$, $S = 0.0$, $Fr = \infty$ and $z^*/h_0 = 0.46$. Geometrical parameters as in the legend of figure 4.

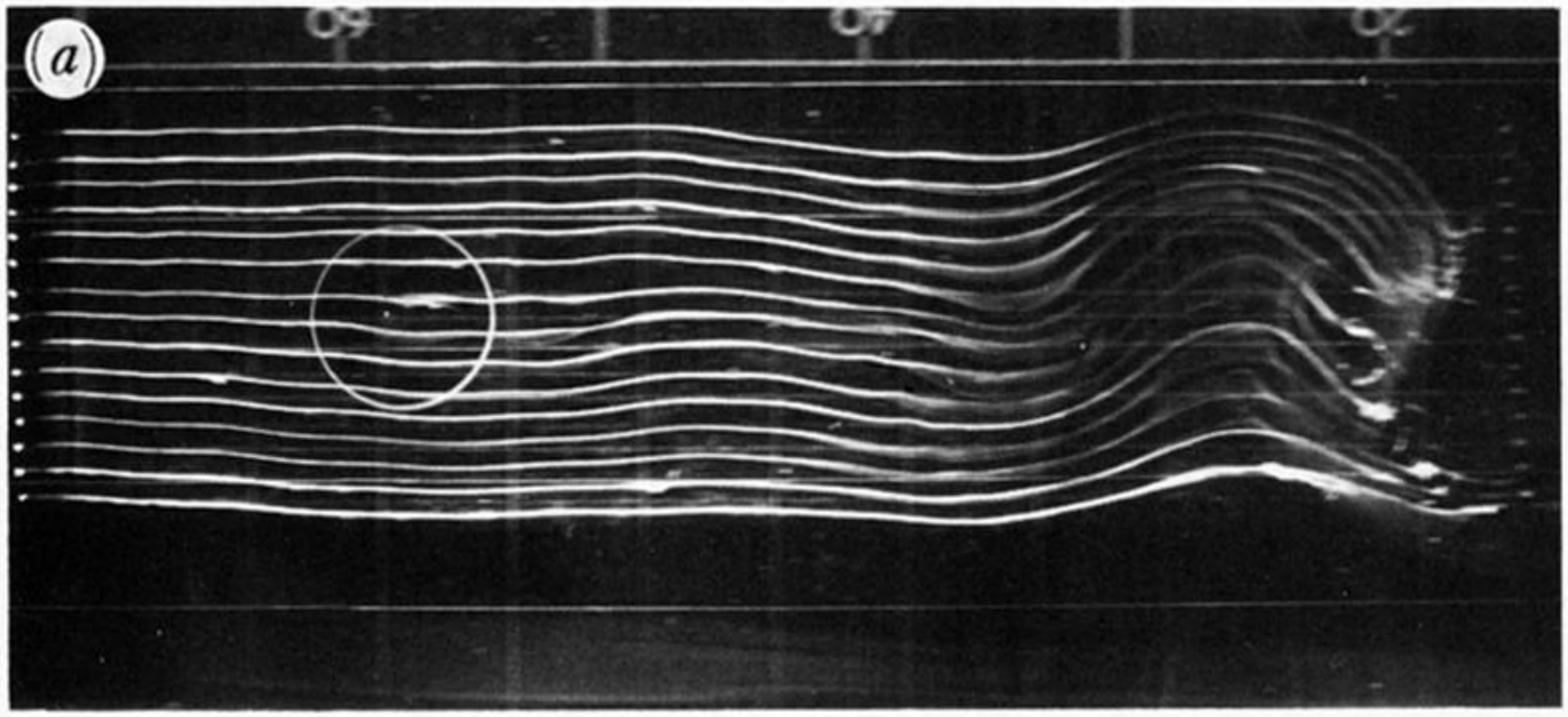

z^*/h_0

1.06

0.76

0.46

FIGURE 13. Streakline photographs for rotating, stratified flow past conical obstacle with $Ro = 0.13$, $Ek = 3.1 \times 10^{-4}$, $Re = 370$, $S = 3.1$ and $Fr = 0.09$. Geometrical parameters as in the legend of figure 4. Arrows on (*b*) and (*c*) indicate initial cyclonic disturbance.

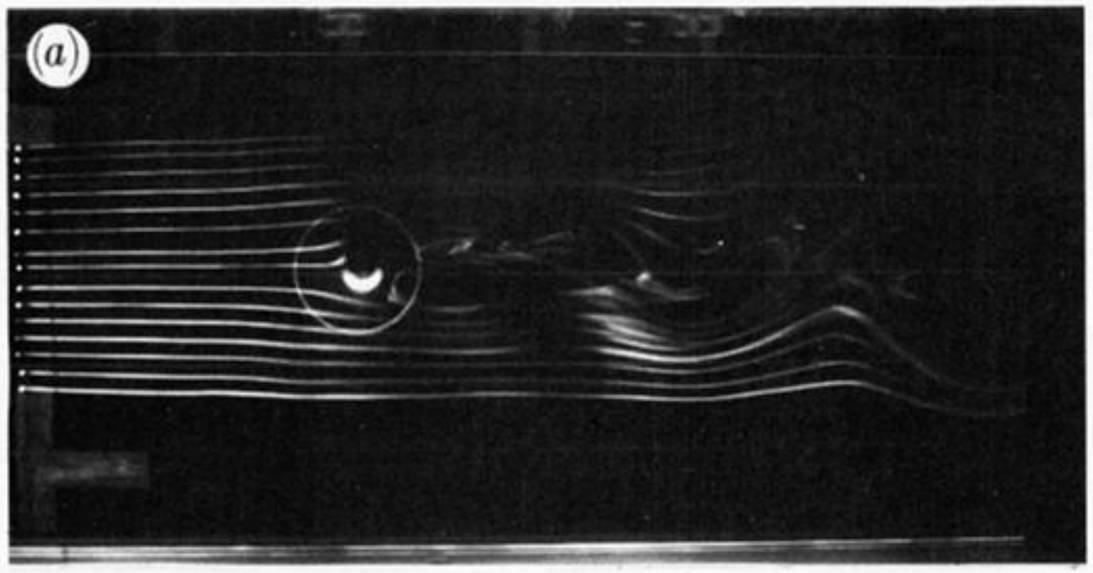

Ro	*Ek*	*S*
∞	∞	∞

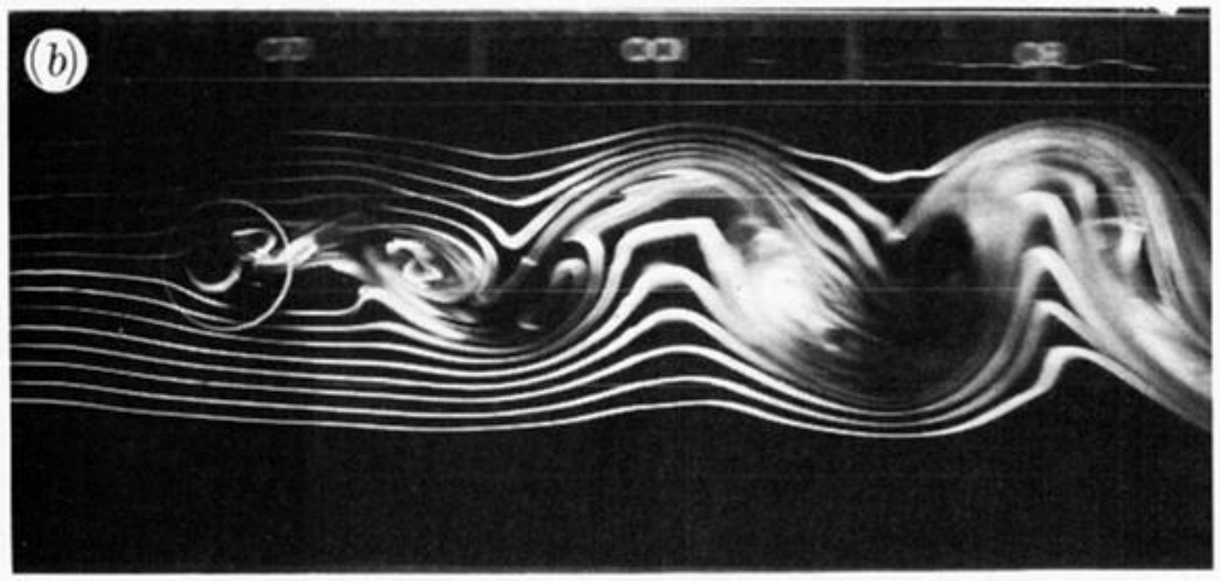

0.26	3.1×10^{-4}	3.0

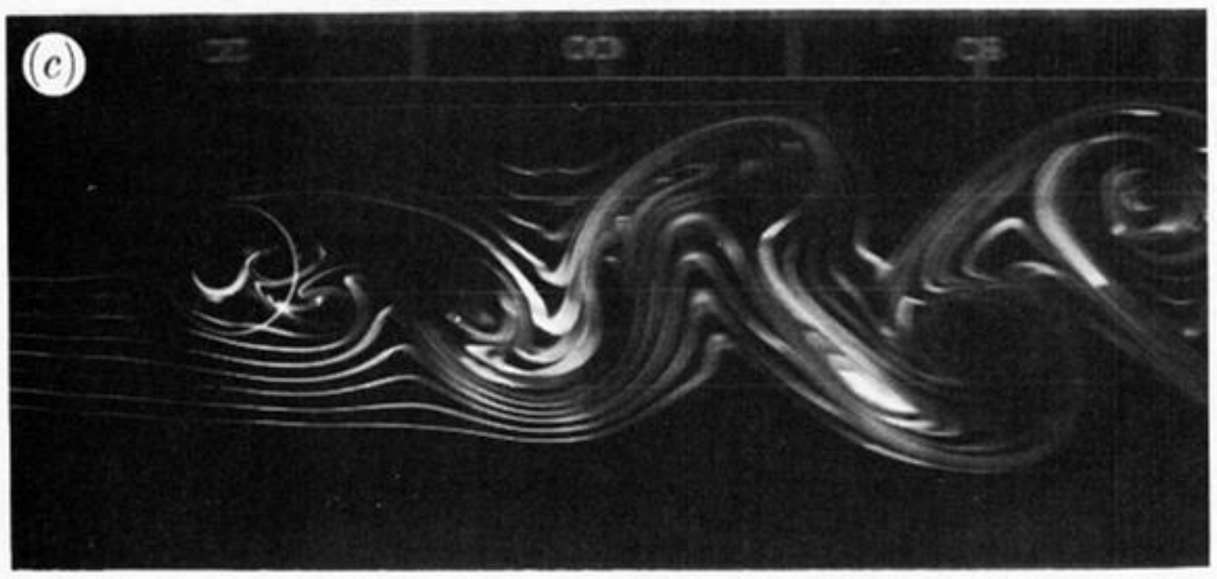

0.13	1.5×10^{-4}	1.1

FIGURE 14. Streakline photographs showing effects of increasing ω upon rotating, stratified flow past conical obstacles for $Re = 740$, $Fr = 0.17$ and $z^*/h_0 = 0.76$. Geometrical parameters as in the legend of figure 4.

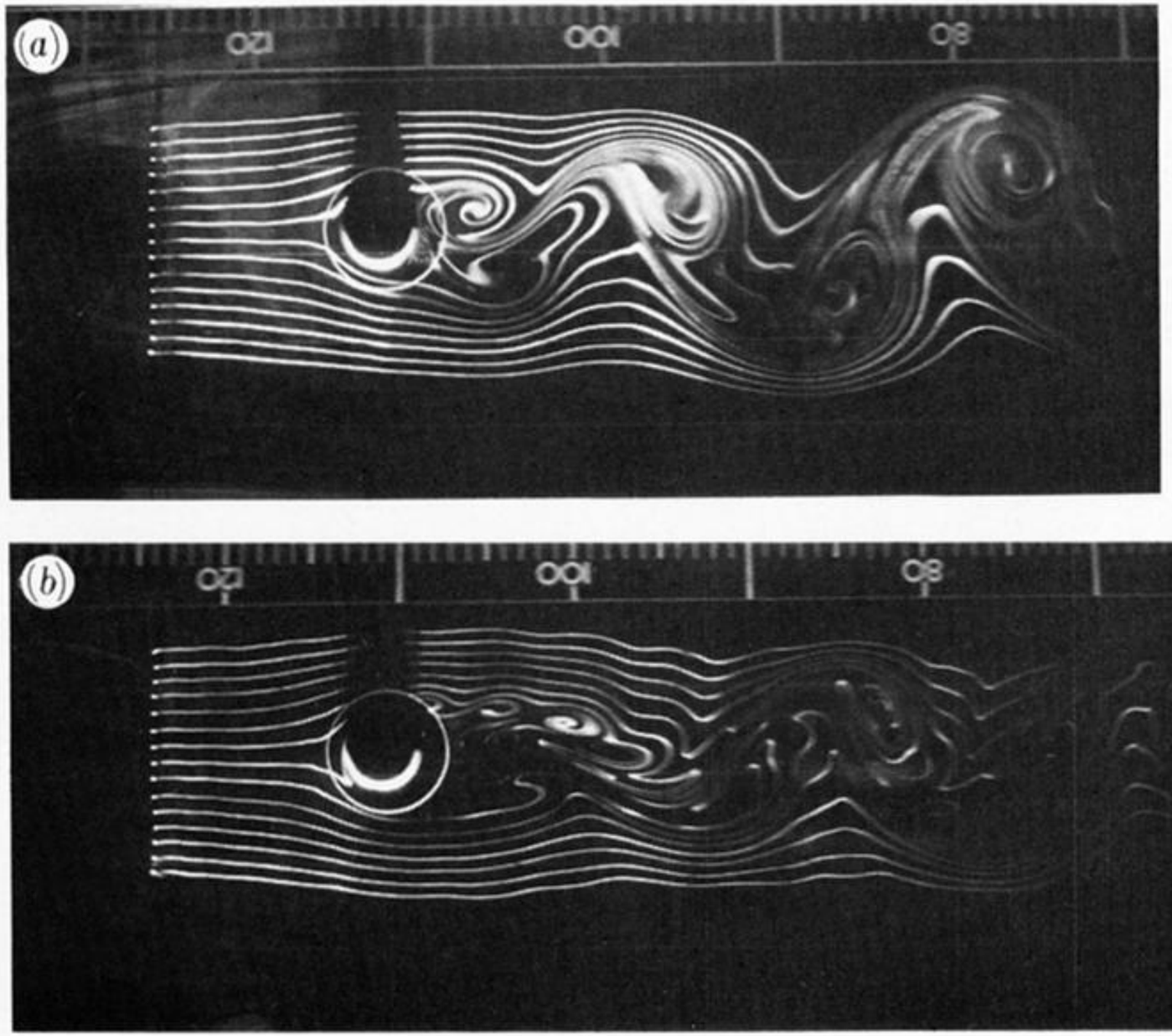

	Ro	*Ek*	*S*
(a)	0.13	3.1×10^{-4}	3.12
(b)	0.06	1.5×10^{-4}	0.85

FIGURE 15. Streakline photographs showing effects of increasing ω upon rotating stratified flow past conical obstacles for $Re = 360$, $Fr = 0.09$ and $z^*/h_0 = 0.46$. Geometrical parameters as in the legend of figure 4.

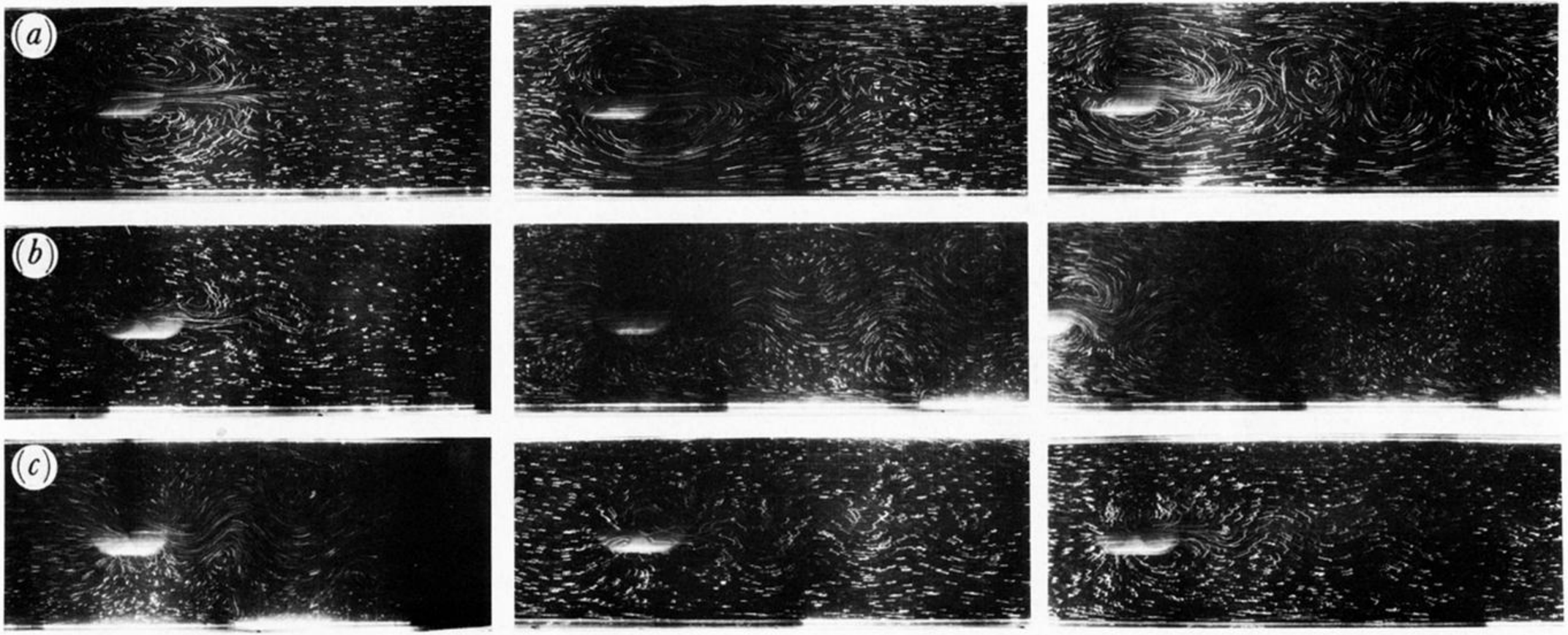

	Ro	*Ek*	*S*
(a)	∞	∞	∞
(b)	0.13	3.6×10^{-4}	5.2
(c)	0.07	1.5×10^{-4}	1.1

$\tau = Ut/D = 5.9$ 9.9 13.8

FIGURE 16. Time sequences of particle streak photographs for rotating stratified flow past conical obstacle for $Re = 370$, $Fr = 0.08$ and $z^*/h_0 = 0.15$. Geometrical parameters as in the legend of figure 4.

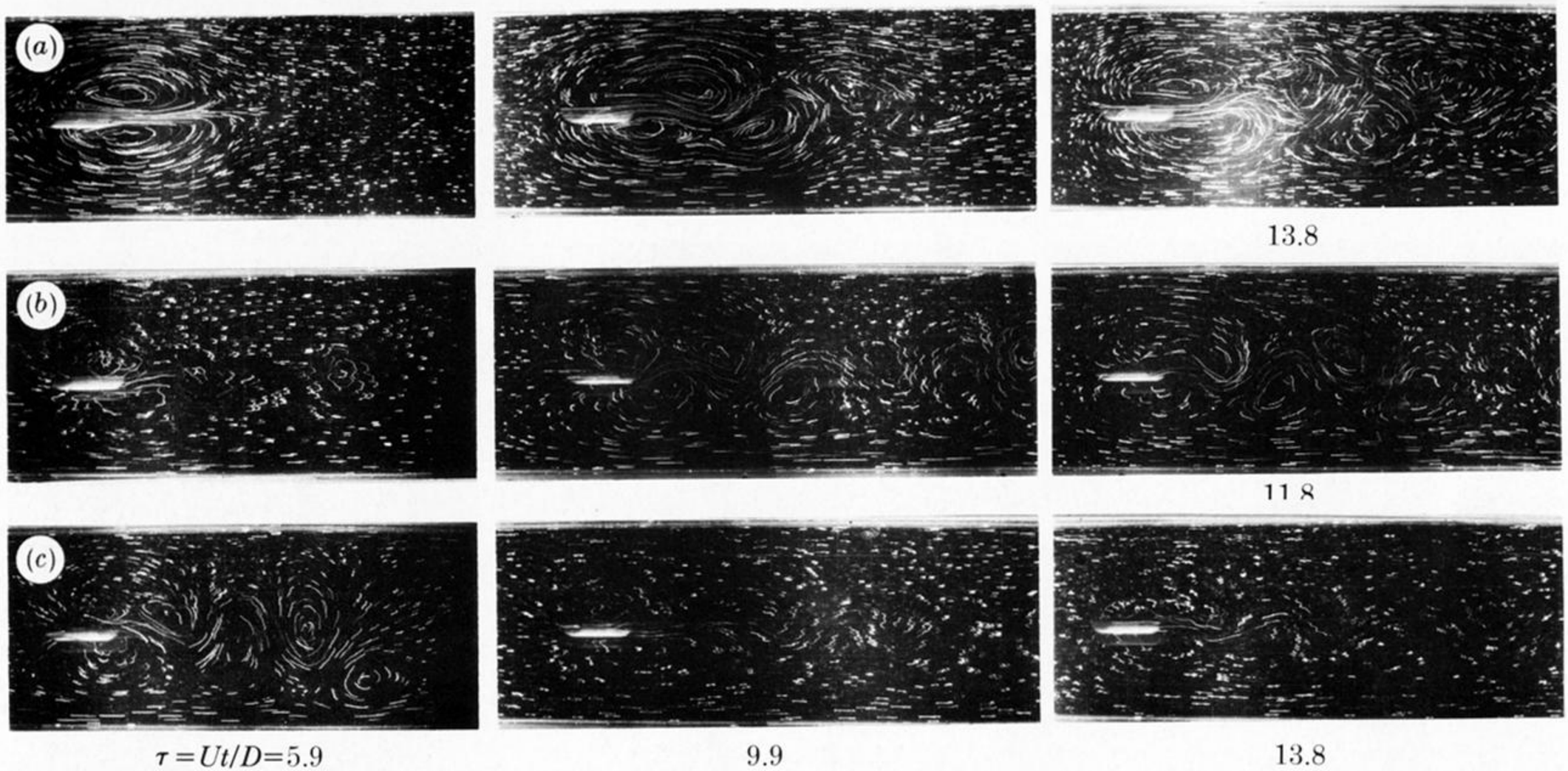

Figure 17. Time sequences of particle streak photographs for rotating stratified flow past conical obstacle for $Re = 390$, $Fr = 0.08$ and $z^*/h_0 = 0.51$. Geometrical parameters as in the legend of figure 4.

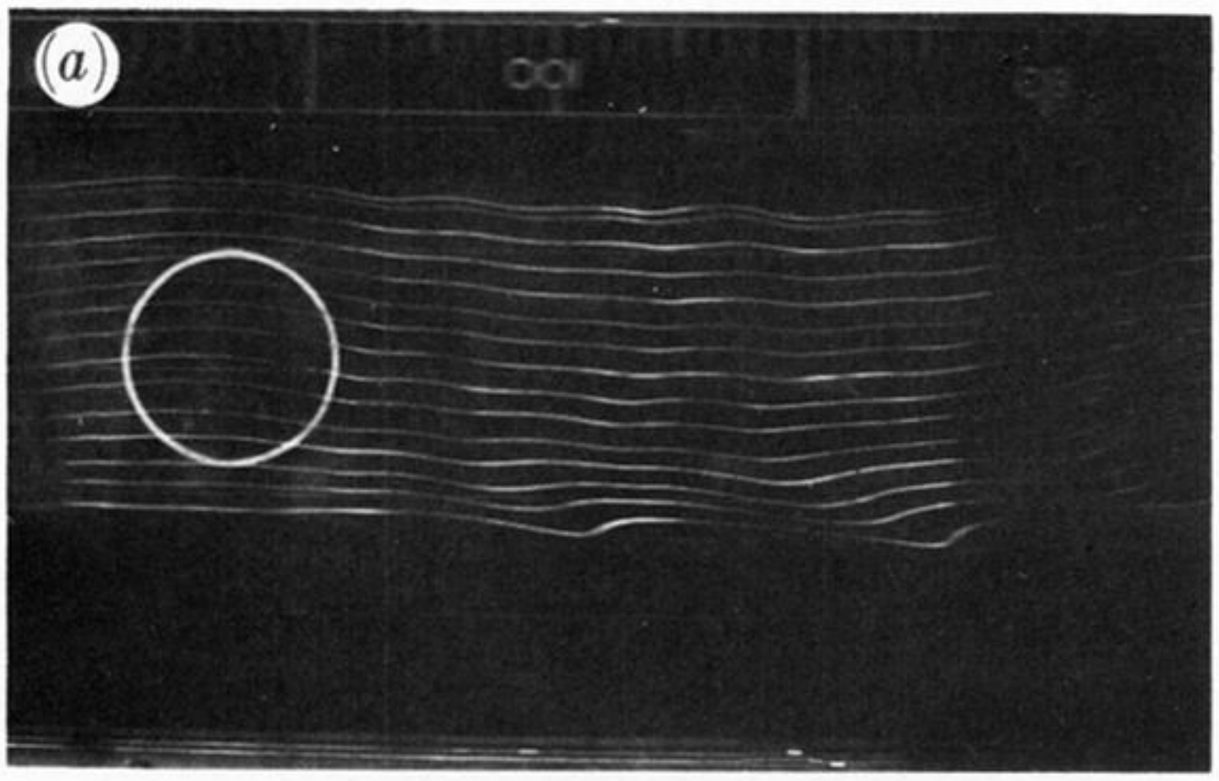

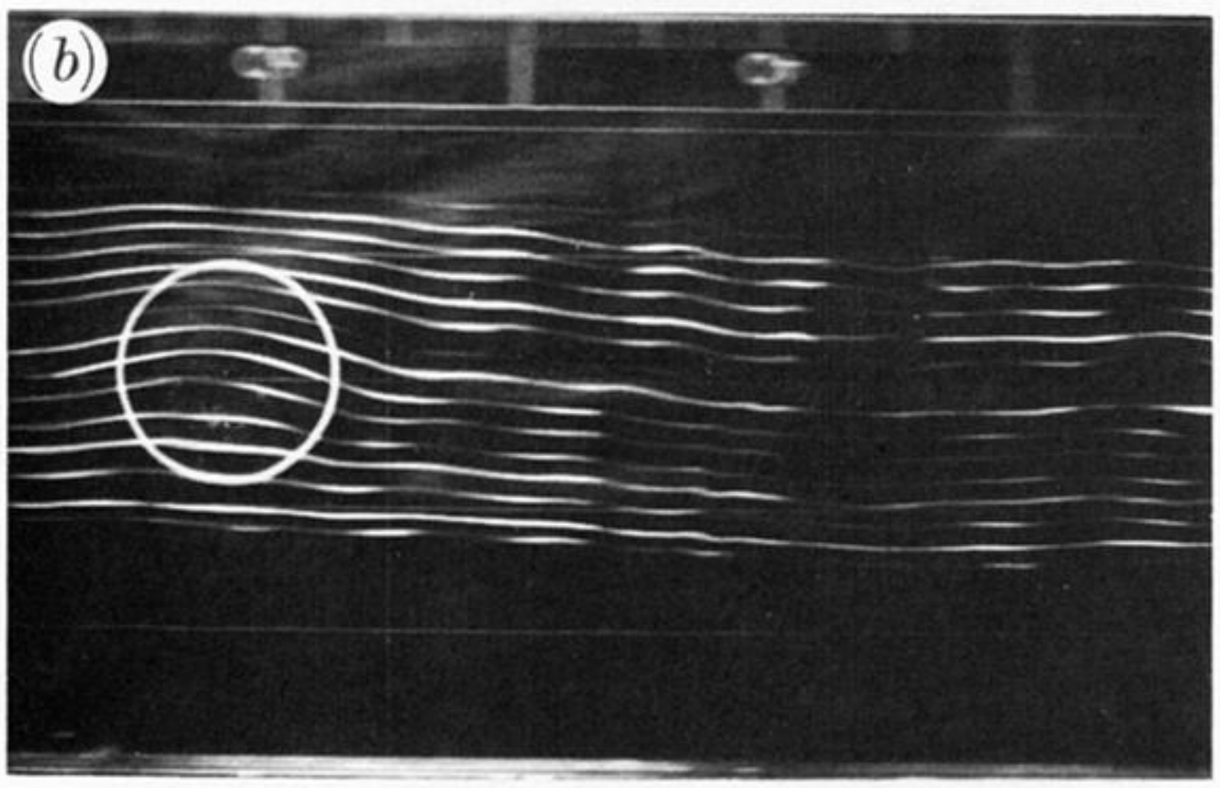

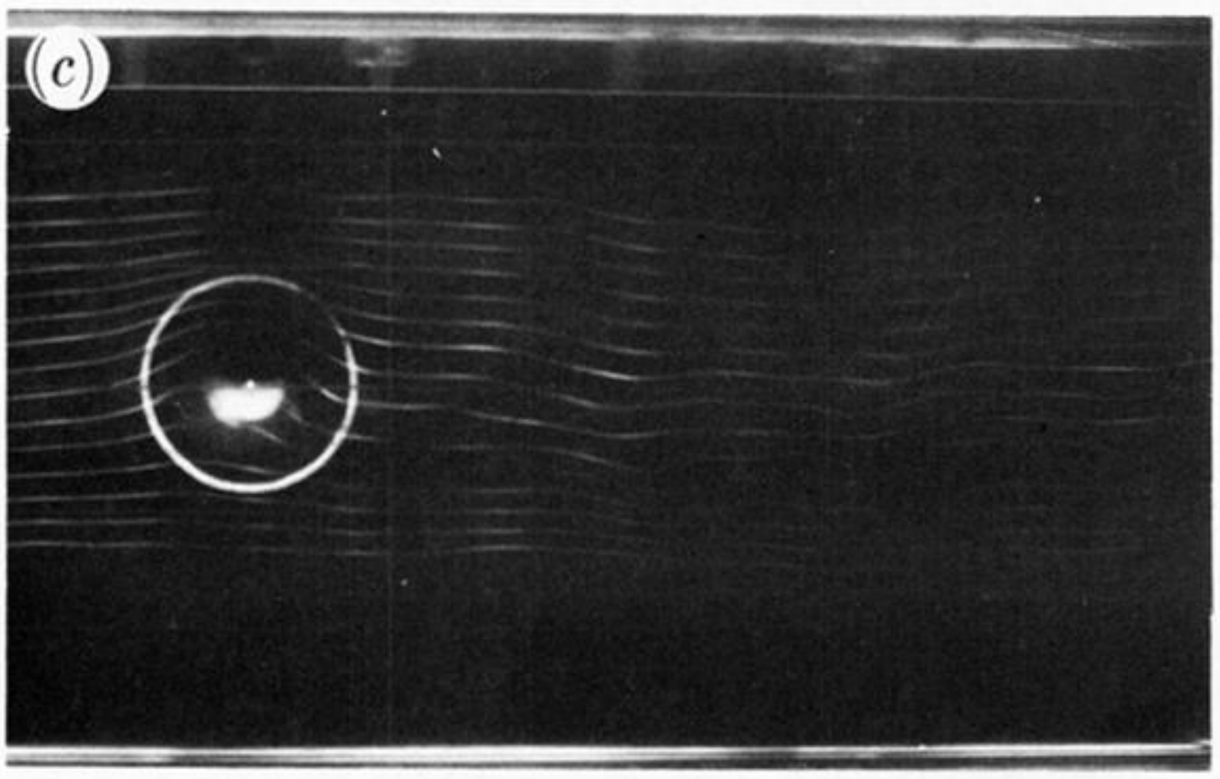

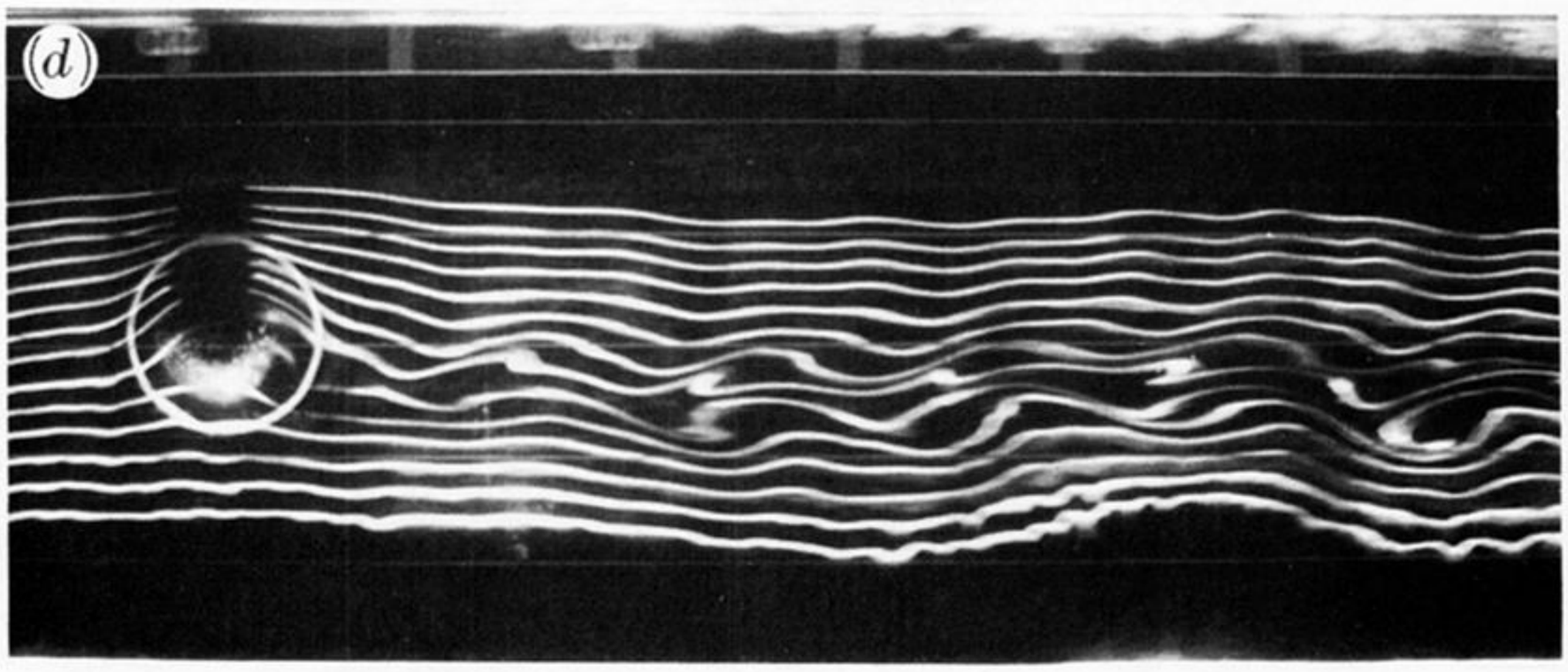

0.49

FIGURE 19. Streakline photographs for rotating stratified flow past cosine-squared topography with $Ro = 0.10$, $Ek = 1.6 \times 10^{-4}$, $Re = 950$, $S = 0.47$ and $Fr = 0.57$. Geometrical parameters as in the legend for figure 8.

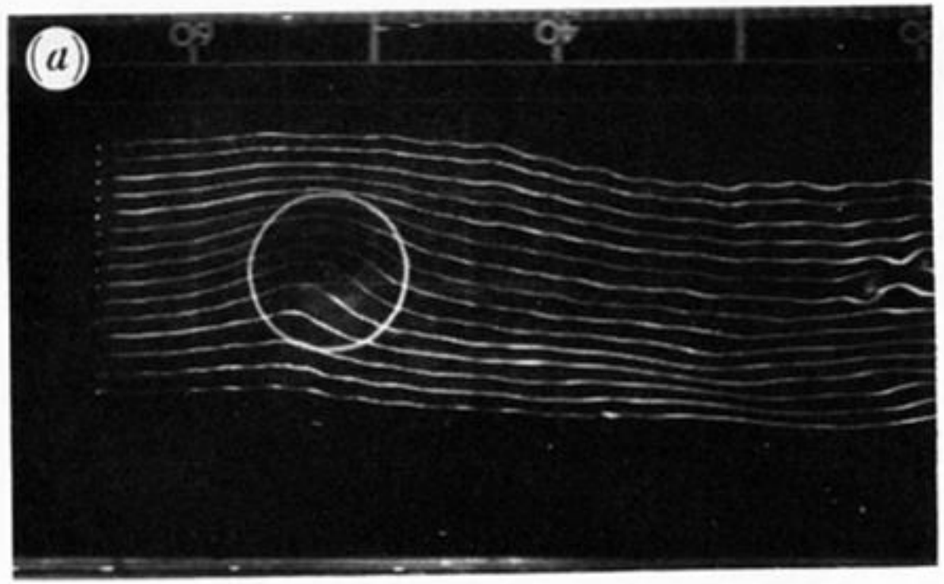

Ro	*Re*	*Fr*
0.05	450	0.39

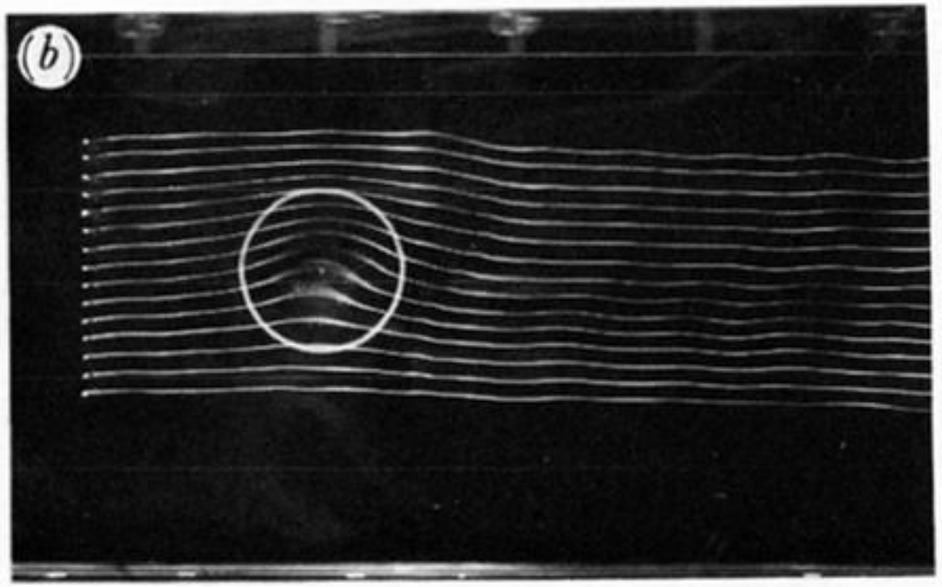

0.10	900	0.82

FIGURE 20. Streakline photographs showing effects of increasing U upon rotating stratified flow past cosine-squared topography for $Ek = 1.7 \times 10^{-4}$, $S = 0.24$ and $z^*/h_0 = 1.46$. Geometrical parameters as in the legend for figure 8.

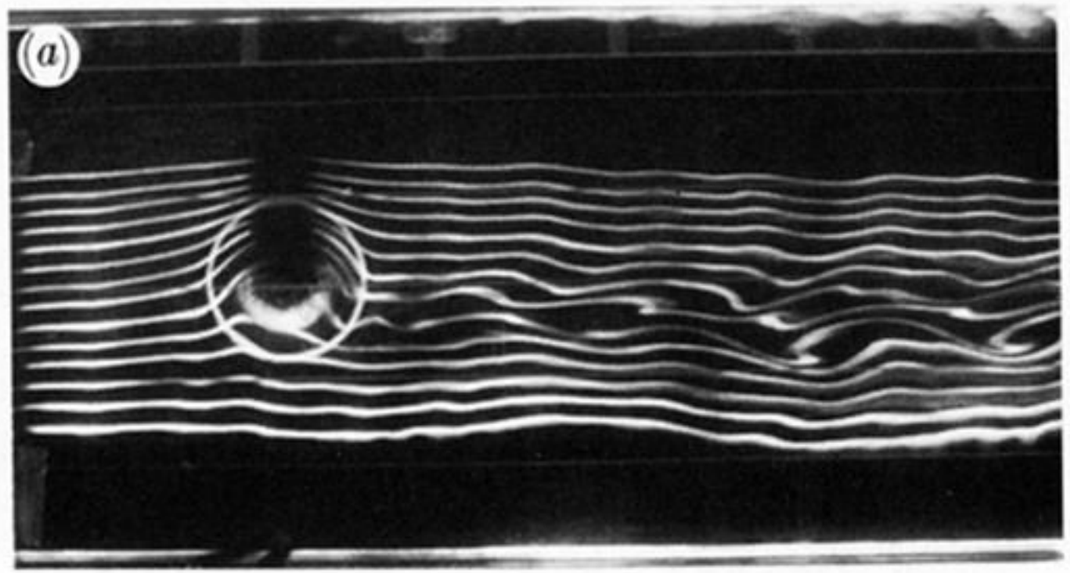

S	(Fr)
0.54	(0.53)

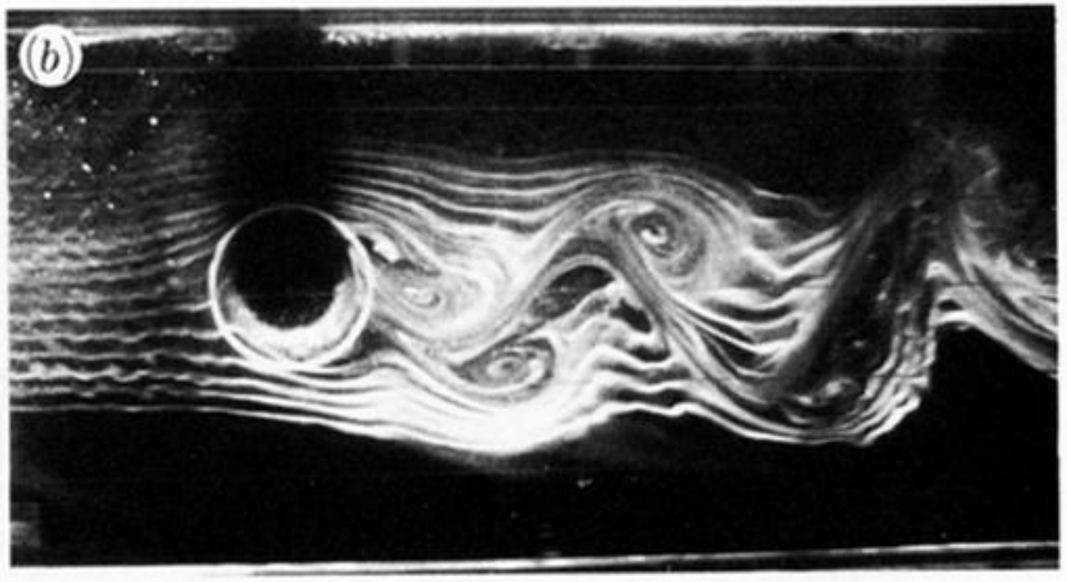

3.8	(0.20)

FIGURE 21. Streakline photographs showing effects of increasing $\Delta\rho/\rho_0$ upon rotating stratified flow past cosine-squared topography for $Ro = 0.10$, $Ek = 1.6 \times 10^{-4}$, $Re = 950$ and $z^*/h_0 = 0.49$. Geometrical parameters as in the legend for figure 8.

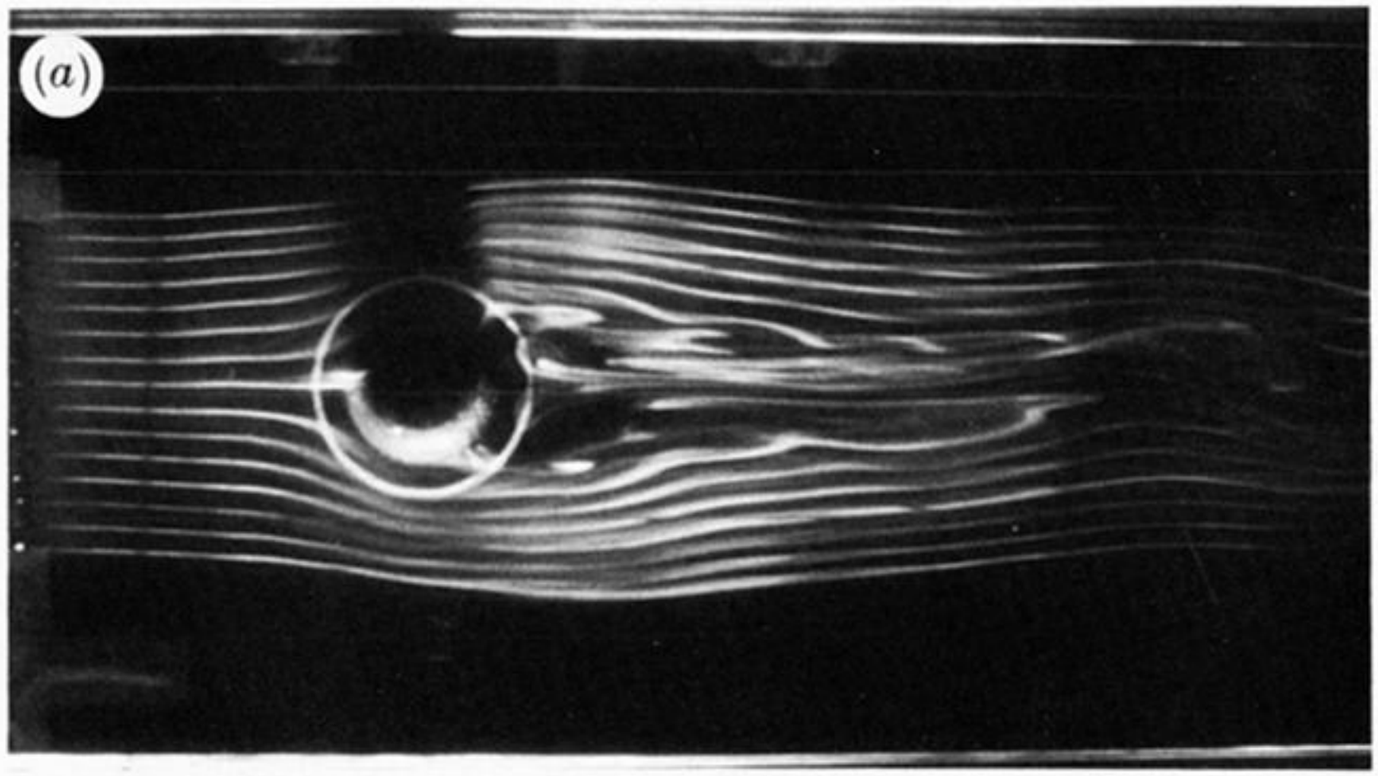

Ro	*Ek*	*S*
∞	∞	∞

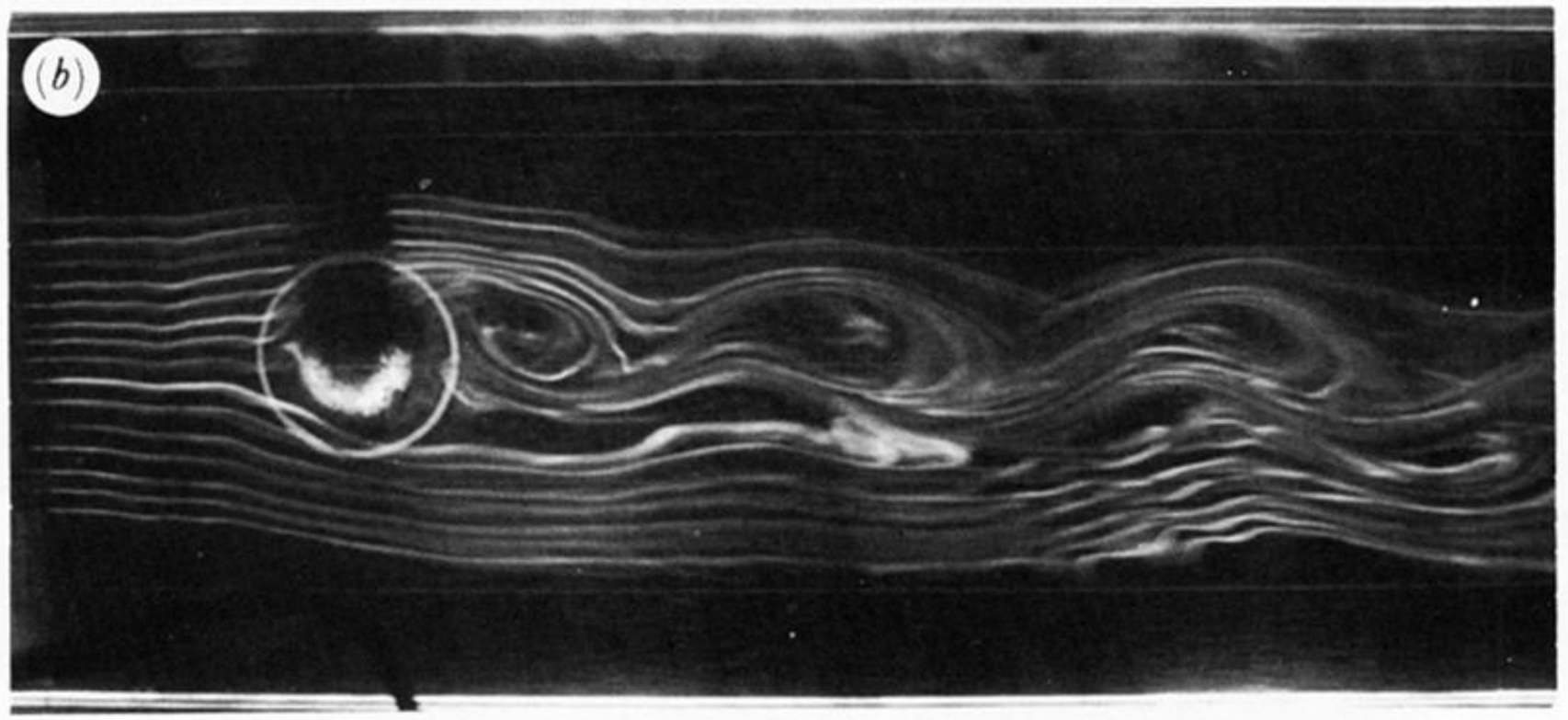

Ro	*Ek*	*S*
0.20	3.2×10^{-4}	14.6

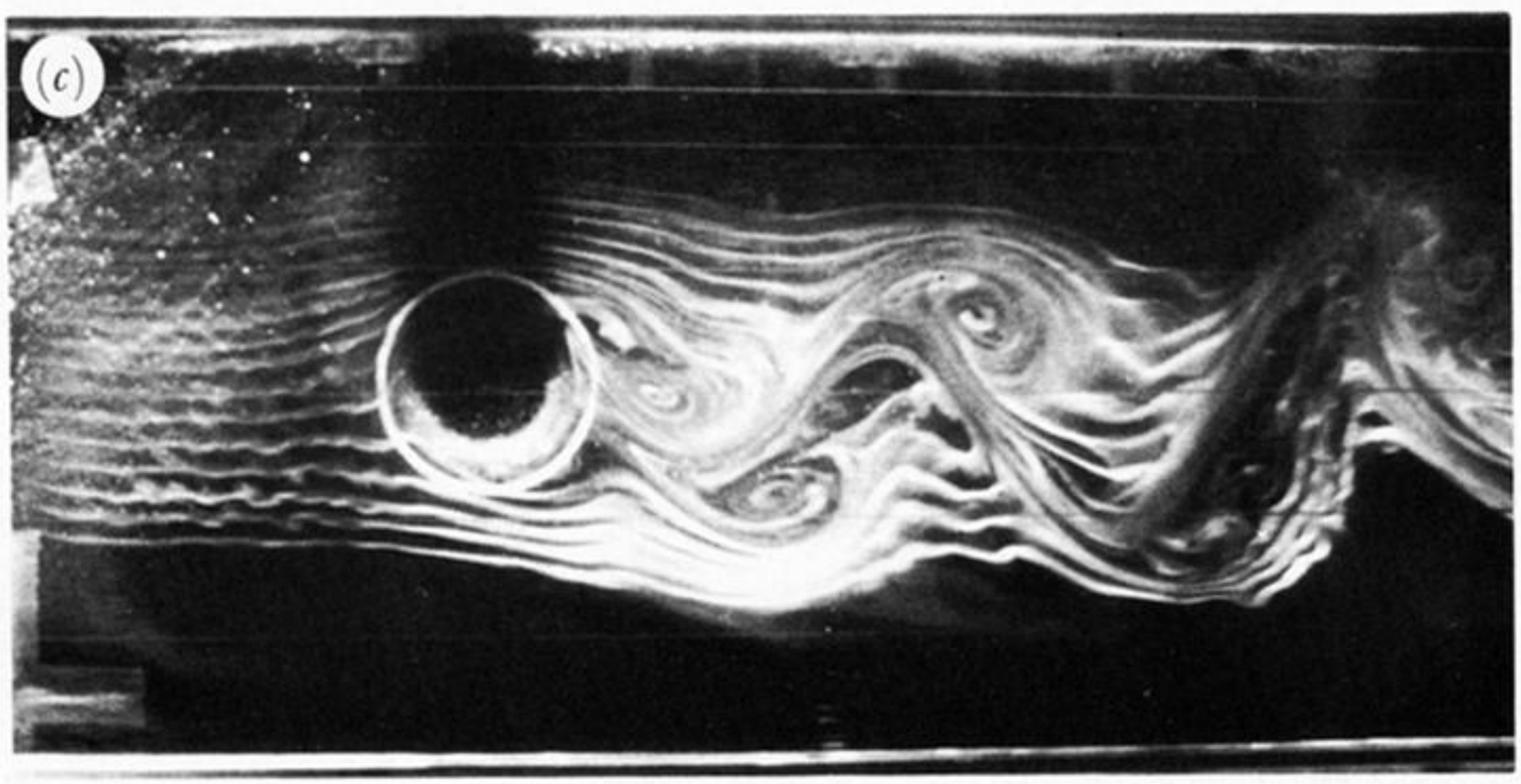

Ro	*Ek*	*S*
0.10	1.6×10^{-4}	3.8

FIGURE 22. Streakline photographs showing effects of increasing ω upon rotating stratified flow past cosine-squared topography for $Re = 980$, $Fr = 0.20$ and $z^*/h_0 = 0.49$. Geometrical parameters as in the legend for figure 8.

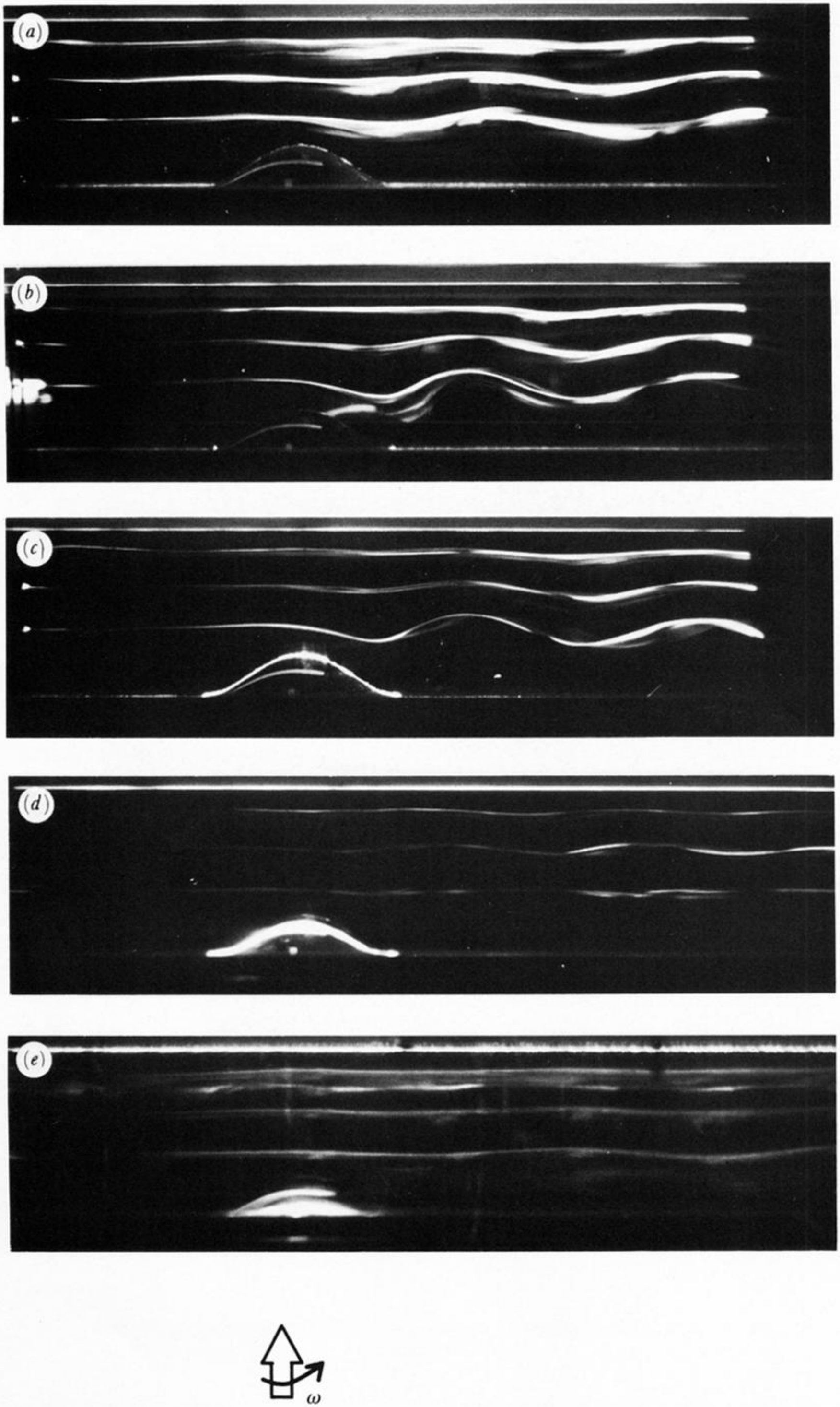

FIGURE 23. Side elevation photographs of lee waves generated by cosine-squared topography for $Ro = 0.30$, $Ek = 3.0 \times 10^{-4}$, $Re = 1510$, $S = 1.7$, $Fr = 0.92$, $z^*/h_0 = 1.46, 2.43, 3.40$ and for $y/(\frac{1}{2}D)$ of (*a*) -0.8, (*b*) -0.4, (*c*) 0.0, (*d*) 0.4 and (*e*) 0.8. Geometrical parameters as in the legend for figure 8.

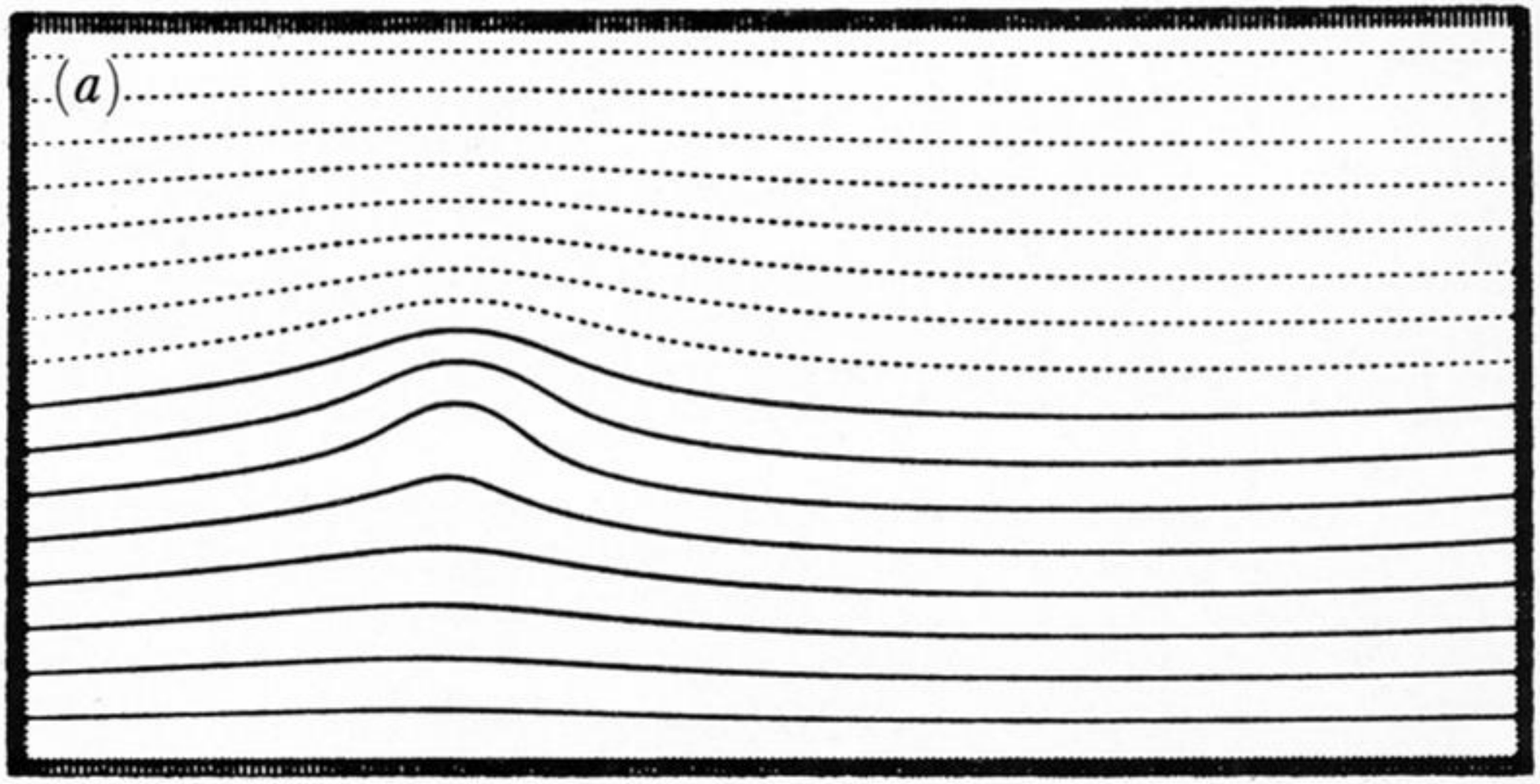

FIGURE 30. A comparison of (*a*) laboratory and (*b*) numerical model streamlines at a height of 3 cm above the bottom, for numerical experiment 1 parameters (see table 1).